Azimuthal Anisotropy of Virtual Photons in Au+Au Collisions at $\sqrt{s_{\mathrm{NN}}} = 2.4\,\mathrm{GeV}$

Azimutale Anisotropie Virtueller Photonen in Au+Au Kollisionen bei $\sqrt{s_{\mathrm{NN}}} = 2.4\,\mathrm{GeV}$
Master-Thesis von Dominique Dittert
Tag der Einreichung:

1. Gutachten: Prof. Dr. Tetyana Galatyuk
2. Gutachten: Dr. Szymon Harabasz

TECHNISCHE
UNIVERSITÄT
DARMSTADT

Fachbereich Physik
Institut für Kernphysik
ViP-QM

Azimuthal Anisotropy of Virtual Photons in Au+Au Collisions at $\sqrt{s_{\mathrm{NN}}} = 2.4\,\mathrm{GeV}$
Azimutale Anisotropie Virtueller Photonen in Au+Au Kollisionen bei $\sqrt{s_{\mathrm{NN}}} = 2.4\,\mathrm{GeV}$

Vorgelegte Master-Thesis von Dominique Dittert

1. Gutachten: Prof. Dr. Tetyana Galatyuk
2. Gutachten: Dr. Szymon Harabasz

Tag der Einreichung:

Erklärung zur Master-Thesis

Hiermit versichere ich, die vorliegende Master-Thesis ohne Hilfe Dritter nur mit den angegebenen Quellen und Hilfsmitteln angefertigt zu haben. Alle Stellen, die aus Quellen entnommen wurden, sind als solche kenntlich gemacht. Diese Arbeit hat in gleicher oder ähnlicher Form noch keiner Prüfungsbehörde vorgelegen.

Darmstadt, den 24.01.2019

_____

(D. Dittert)

Abstract

The HADES at SIS18 (GSI, Darmstadt) investigates strongly interacting matter at high net-baryon densities and moderate temperatures, which resembles properties of QCD matter as they might exist in the interior of compact stellar objects. Virtual photons, that decay into dileptons, are penetrating probes which directly access the entire space-time-evolution of the fireball and escape from the collision zone without further interactions. Thus they provide unique information about the various stages of the collision. Collective observables like flow are used to describe the macroscopic properties of nuclear matter. Since the effective temperature extracted from the m_T spectra of dileptons results from the superposition of all fireball stages with decreasing temperature T but increasing radial flow over time, it is difficult to disentangle early and late emission sources. In comparison, the elliptic flow does not show this implicit time dependence and the combined dependence of elliptic flow of dileptons on their transverse momentum and their invariant mass provides a rich landscape of structures, which allows to set the observational window on specific stages of the fireball evolution.

In this thesis the azimuthal anisotropy of virtual photons from Au+Au collisions at $\sqrt{s_{NN}} = 2.4\,\text{GeV}$ measured with HADES is analyzed. For the lepton identification a multi variate analysis using a machine learning algorithm is performed to separate the lepton and hadron signals. One of the most important detectors for lepton identification is the ring imaging cherenkov (RICH) detector. Here the so called backtracking algorithm is used that utilizes the information from the tracking and time-of-flight detectors to preselect electron candidates for which the position of a possible signal in the RICH detector is predicted. Subsequently the pairs are build and their $\Delta\phi$ distributions are analyzed to obtain the flow values. Since the flow components and the collision geometry are correlated, the event plane angle has to be reconstructed for each event and subtracted from the ϕ angle of the dilepton pair to obtain distribution of $\Delta\phi$ in the laboratory system. This is done using a modified total transverse momentum transfer technique using the spectator hits in the forward wall detector. This reaction plane angle has to be corrected for shifts of the beam in x and y, for anisotropies and finally also the event plane resolution has to be determined, to correct the obtained flow values for it. A further correction is applied to account for the occupancy of the detector. The directed and elliptic flow components will be reconstructed in four mass regions and for different centralities, rapidities and transverse momenta. For the pion mass region also a comparison to the flow of the charged pions will be performed.

This thesis is structured as follows. Chapter 1 will give an introduction to the standard model of particle physics, the theory of quantum chromo dynamics and the topic of heavy ion collision including electromagnetic probes and collective flow. In Chapter 2 the high acceptance di-electron spectrometer (HADES) and its different detector systems will be introduced. The data analysis strategy beginning with particle reconstruction, event selection and single lepton identification over the handling of the combinatorial background in the dilepton analysis to the flow reconstruction will be subject to Chapter 3. In Chapter 4 the results of this analysis will be presented before this thesis concludes with a short summary and outlook in Chapter 5.

Zusammenfassung

HADES am SIS18 (GSI, Darmstadt) untersucht stark wechselwirkende Materie bei hohen Netto-Baryonendichten und moderaten Temperaturen, was den Eigenschaften von QCD Materie entspricht, wie sie im Inneren kompakter stellarer Objekte auftreten könnte. Virtuelle Photonen, die in Dileptonen zerfallen, sind durchdringende Sonden, die direkt die gesamte Raum-Zeit-Evolution des Feuerballs zugänglich machen und ohne weitere Interaktion die Kollisionszone verlassen. Daher bieten sie einzigartige Informationen über die vielfältigen Stadien der Kollision. Kollektive Observablen wie beispielsweise Fluss werden verwendet, um die makroskopischen Eigenschaften von Kernmaterie zu beschreiben. Die effektive Temperatur, die aus den m_T Spektren der Dileptonen extrahiert wird, stammt aus der Superposition aller Stadien der Kollision, wobei über die Zeit hinweg die Temperatur ab- und der radiale Fluss zunimmt. Daher ist es schwierig frühe und späte Emissionsquellen zu unterscheiden. Im Vergleich dazu hat der elliptische Fluss keine implizite Zeitabhängigkeit. Die kombinierte Abhängigkeit des elliptischen Flusses von Dileptonen von ihrem Transversalimpuls und ihrer invarianten Masse bietet vielfältige Strukturen, die es erlauben das Augenmerk auf spezifische Stadien der Kollisionsevolution zu legen.

In der vorliegenden Arbeit wird die azimutale Anisotropie virtueller Photonen aus mit HADES gemessenen Au+Au Kollisionen bei $\sqrt{s_{NN}} = 2.4\,\text{GeV}$ analysiert. Für die Leptonidentifikation wird eine multivariable Analyse mittels eines Algorithmus für maschinelles Lernen durchgeführt, um Leptonen und Hadronen zu separieren. Einer der wichtigsten Detektoren für die Leptonidentifikation ist der RICH (Ring Imaging Cherenkov) Detektor. Hierbei wird ein sogenannter Backtracking Algorithmus verwenden, der die Informationen der Spur und Flugzeit Detektoren nutzt, um mögliche Elektronkandidaten auszuwählen. Für diese wird dann die Position eines möglichen Signals im RICH Detektor vorhergesagt. Anschließend werden die Paare gebildet und ihre $\Delta\phi$ Verteilungen analysiert, um die Flusswerte zu erhalten. Da Flusskomponenten und Kollisionsgeometrie korreliert sind, muss der Winkel der Reaktionsebene vom Azimutalwinkel des Dileptonenpaars subtrahiert werden, um die $\Delta\phi$ Verteilung im Laborsystem zu erhalten. Zur Rekonstruktion der Reaktionsebene werden die auftreffenden Zuschauerteilchen im Forward Wall Detektor genutzt. Die so erhaltene Reaktionsebene wird auf Grund von Strahlverschiebungen in x und y Richtung korrigiert. Des Weiteren wird eine Anisotropiekorrektur angewendet und zuletzt die Auflösung der Reaktionsebene bestimmt, um die Flusswerte damit zu korrigieren. Eine weitere Korrektur wird angewendet, um für Effizienzverluste auf Grund hoher Spurdichten im Detektor Rechnung zu tragen. Die gerichteten und elliptischen Flusskomponenten werden in vier Massebereichen rekonstruiert und hinsichtlich verschiedener Zentralitäten, Rapiditäten und Transversalimpulse analysiert. Im Pionen Massebereich wird außerdem ein Vergleich zwischen dem Fluss der geladenen Pionen und dem Dileptonen Fuss angestellt.

Diese Thesis ist wie folgt gegliedert. Kapitel 1 gibt eine Einführung zum Standard Modell der Teilchenphysik, der Theorie der Quanten Chromodynamik und dem Thema der Schwerionenkollisionen, einschließlich elektromagnetischer Sonden und kollektivem Fluss. In Kapitel 2 wird das High Acceptance Di-Electron Spectrometer HADES sowie seine verschiedenen Detektorsysteme vorgestellt. Die Strategie zur Datenanalyse, angefangen mit der Teilchenrekonstruktion, der Auswahl der Events und der Leptonenidentifikation über die Handhabung des kombinatorischen Hintergrunds in der Dileptonen Analyse hin zu der Rekonstruktion des Flusses ist

Thema in Kapitel 3. In Kapitel 4 werden die Ergebnisse dieser Analyse vorgestellt, ehe die Thesis mit einer kurzen Zusammenfassung und einem Ausblick in Kapitel 5 abgeschlossen wird.

Contents

1 Introduction

People all over the centuries have asked questions like "*Where do we come from?*", "*How was our world created?*" and "*What is it made of?*". Today, most people believe, that the universe was formed in the Big Bang around 13.8 billion years ago. After an initial inflation phase, the universe cooled and allowed the formation of the elementary particles. The prevailing theory, describing these particles and the interactions between them is the Standard Model of particle physics. It was developed in the 1970s and although there are experimental results showing the existence of physics beyond the Standard Model, such as neutrino oscillations, it is rather considered incomplete than wrong.

In this chapter a short overview of the Standard Model will be given, including experimental observations verifying the existence of quarks and gluons as well as motivating the introduction of another quantum number, the color charge. This will be followed by an introduction to Quantum Chromodynamics (QCD), the theory of strong interaction, and its underlying symmetries. Subsequently we will take a look at heavy ion collisions as a tool to produce and observe strongly interacting matter in the laboratory, including important parameters of those collisions as well as different models to describe them. In the last part, the use of electromagnetic probes, especially virtual photons, is motivated and their properties are discussed.

1.1 The Standard Model of Particle Physics

The particles of the Standard Model can be distinguished by their spin. There are 12 elementary fermions with half integer spin, that are classified according to their interaction. The six quarks (u, d, s, c, t, b) carry color charge, hence they undergo the strong interaction. Since they also have electromagnetic charge and weak isospin, they also experience the forces of the electromagnetic and the weak interaction. The six leptons (e, μ, τ, ν_e, ν_μ, ν_τ) are not colored, thus they are unaffected by the strong interaction and since the neutrinos do not have an electric charge, they are also not influenced by the electromagnetic interaction. The matter particles naturally fall into three generations. The first generation, consisting of the light up and down quarks, the electron and the electron neutrino, forms our 'everyday matter'. The second and third generation lead to the formation of exotic states, for instance the kaon, that contains strangeness. The particles of the tree generations only differ in their masses. All other properties are similar in a sense, that they possess exactly the same fundamental interactions.

The carriers of the forces between the elementary particles are the gauge bosons with spin 1. There are three different types of gauge bosons, corresponding to the three fundamental forces contained in the Standard Model. Firstly the massless photon, which mediates the electromagnetic force. Secondly the W^+, W^- and Z bosons as mediators of the weak interaction, with masses of 80.4 GeV and 90.1 GeV, respectively, and lastly the eight gluons that mediate the strong interaction. Additionally, the Higgs boson, a scalar boson with spin 0, exists and due to its symmetry breaking the quarks are not massless. In Figure 1.1 the particles and forces of the Standard Model are summarized.
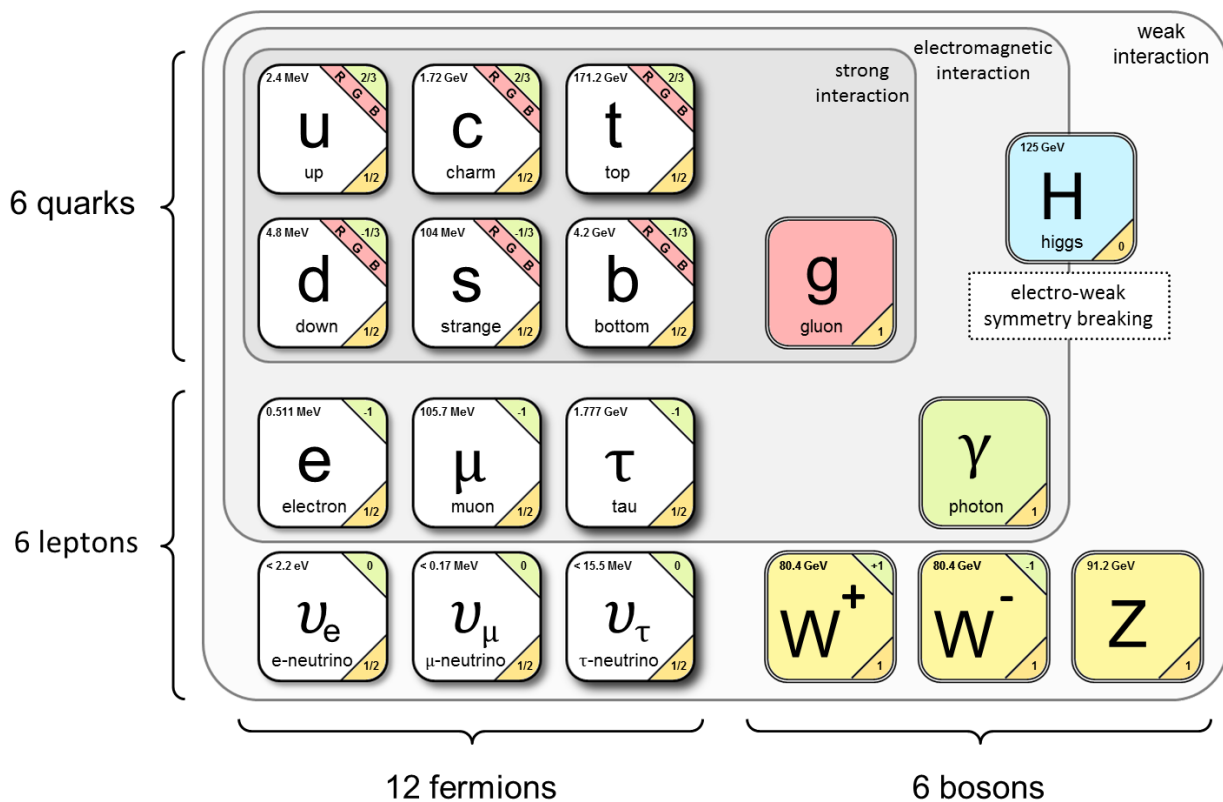
Figure 1.1: The figure shows a summary of all particles and forces contained in the Standard Model of particle physics. In the upper left corner of each cell, the respective mass of each particle is shown. In the upper right corner one can find the electric charge and in the lower right corner the spin of the particle is specified.

While single leptons can be observed experimentally, isolated quarks have never been seen. Instead, they are always bound into colorless states, the hadrons. There can either be a combination of three quarks, one of each colour, that form the baryons. One example would be the proton, consisting of two up and one down quark. The other possibility is a bound state of a quark and an antiquark with corresponding colors, for example green and anti-green. Those quark-antiquark pairs form the mesons.

1.2 Experimental Evidence of Quarks and Gluons

In the early 1960's Murray Gell-Mann introduced the so-called Eightfold Way, a scheme, that arranges baryons and mesons according to their charge and strangeness. In Figure 1.2 the baryon octet is shown as an example. Gell-Mann assumed, that the higher symmetry of elementary particles is the group of all unitary 3x3 matrices with unit determinant (SU(3)). [1]
This model led to the postulation of elementary fermionic constituents, the quarks, in 1964. The prediction of quarks was made independently by Gell-Mann and George Zweig and the great novelty was the idea of particles with non-integral charge. [3, 4]

In 1967 deep-inelastic electron-proton scattering experiments, performed by the MIT-SLAC collaboration revealed the substructure of the proton. A 20 GeV spectrometer was used to measure
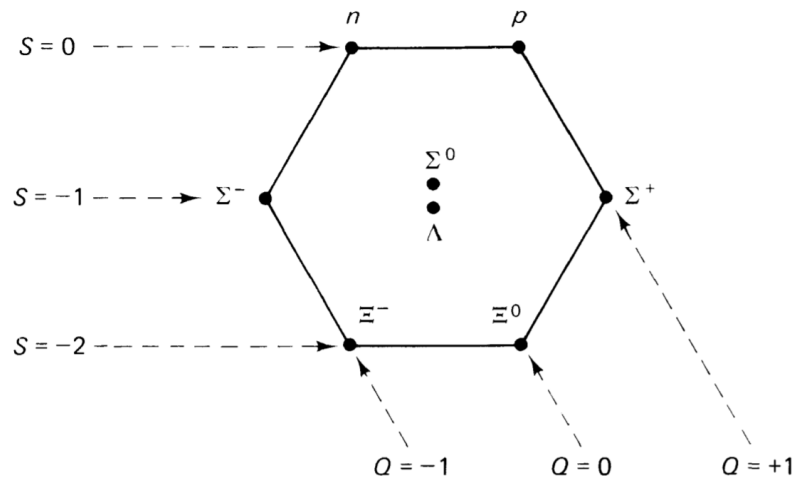
Figure 1.2: The baryon octet: Horizontal lines associate particles of like strangeness and on the downward sloping diagonal lines lie particles of the same charge. [2]

electrons under a scattering angle of 6°. The counting rates in the deep inelastic region were much higher than expected for a soft proton. Figure 1.3 shows a plot of the cross section versus the invariant momentum transfer q^2 to the proton.

It is apparent, that the probability of deep inelastic scattering decreases much slower with q^2 than the one for elastic scattering. In analogy to Rutherford's discovery of the atomic nucleus this result can be interpreted as the electron hitting some kind of hard core inside the protons. The proton structure function F_2 was also extracted and showed a behavior known as Bjorken scaling, i.e. the data points all fell along a single curve that depends on the ratio of the energy loss of the electron and the invariant momentum transfer rather than on the two values independently.

At the same time Richard Feynman developed a model in which protons were composed of pointlike particles that he called partons. With the parton model the Bjorken scaling could be explained and it became apparent, that Feynman's partons are indeed the quarks postulated by Gell-Mann and are consistent with the proton substructure measured by the SLAC experiment. In further experiments the physical properties of the newly discovered quarks such as their spin or charge were determined. In 1975 jets from high energy e^+e^-- collisions at SLAC were observed and provided the visible evidence for the existence of quarks. The corresponding Feynman Diagram for such a 2-jet event is shown in Figure 1.5a. [5, 6]

To motivate the necessity for the existence of color charge, we can take a look at the delta resonance Δ^{++}. It consists of three u-quarks, thus it is symmetric under the interchange of any two quarks. The spin of the Δ^{++} is $J = \frac{3}{2}$, which requires the spins of all three quarks to be parallel: $\left|\Delta^{++}\right\rangle = \left|u\uparrow u\uparrow u\uparrow\right\rangle$. Furthermore it is the lightest baryon with $J^P = \frac{3}{2}^+$, hence we can assume that its orbital angular momentum is $\ell = 0$, leading to a symmetric spatial wave function. Therefore the total wave function of the Δ^{++} is symmetric in space, spin and flavor. This is a violation of the Pauli principle, since the delta is a fermion, which must have an antisymmetric wave function.

Thus another quantum number is needed, to comply the principle. For this additional quantum number, the term color is chosen, although it has nothing to do with actual colors. There need to be at least three colors to create an antisymmetric wave function for the Δ^{++}- resonance, since
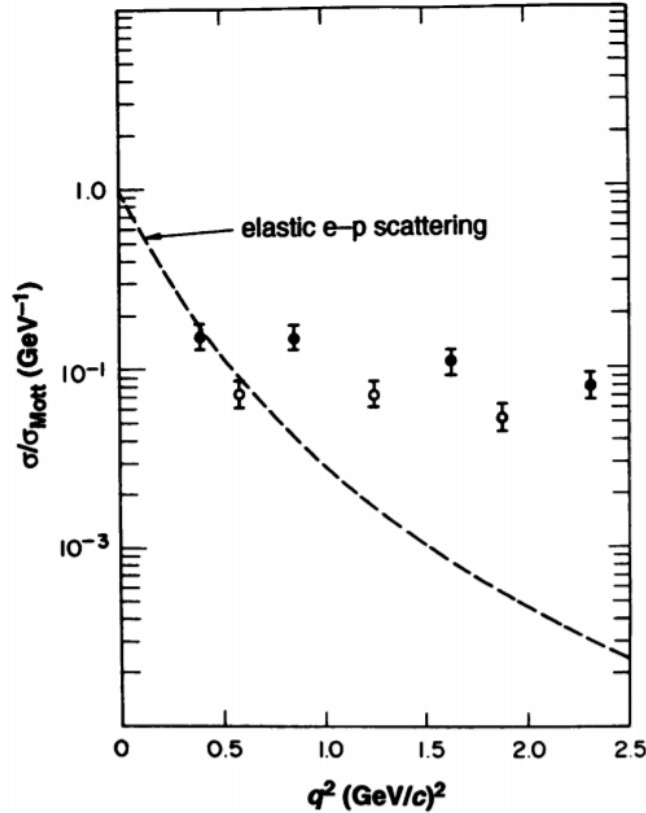
Figure 1.3: Cross sections from electron proton scattering normalized with the respective Mott cross sections for scattering from a point-like proton. [5]

all three quarks have to be different to be distinguished. Including the tree colors red, green and blue, the wave function is no longer symmetric under the exchange of particles, leading to the total antisymmetric wave function: $\left|\Delta^{++}\right\rangle = \left|u_r\uparrow\ u_g\uparrow\ u_b\uparrow\right\rangle$. [7]

Experimental observations support the existence of exactly three different colors. In electron-positron-scattering at sufficiently high energies pair production of leptons (muons or taus) or quarks can take place. As the quarks fly apart, the coupling strength of the strong interaction increases until further quark-antiquark-pairs are produced. This process of hadronization can be observed as jets of particles. The cross section of the quark pair production can be calculated analogously to the cross section of muon pair production, since the electromagnetic interactions are the same. Since there are several different quarks, the total cross section is given by the sum over the individual cross sections of all quark flavors that can be produced at the given energy. Another difference to the muon cross section is, that the quarks do not carry the electric charge of $1 \cdot e$ but rather a charge Q_f which depends on the quark flavor. Futhermore the quark-antiquark pair of one flavor can be produced in different colors. Thus there is an additional factor of N_c corresponding to the number of colors. By calculating ratio of the quark and muon cross sections all factors not connected to the special properties of quarks are eliminated. This leads to:

$$R = \frac{\sigma\left(e^+e^- \rightarrow \text{hadrons}\right)}{\sigma\left(e^+e^- \rightarrow \mu^+\mu^-\right)} = \frac{\sum_f \sigma\left(e^+e^- \rightarrow q_f\bar{q}_f\right)}{\sigma\left(e^+e^- \rightarrow \mu^+\mu^-\right)} = N_c \cdot \sum_f Q_f \qquad (1.1)$$
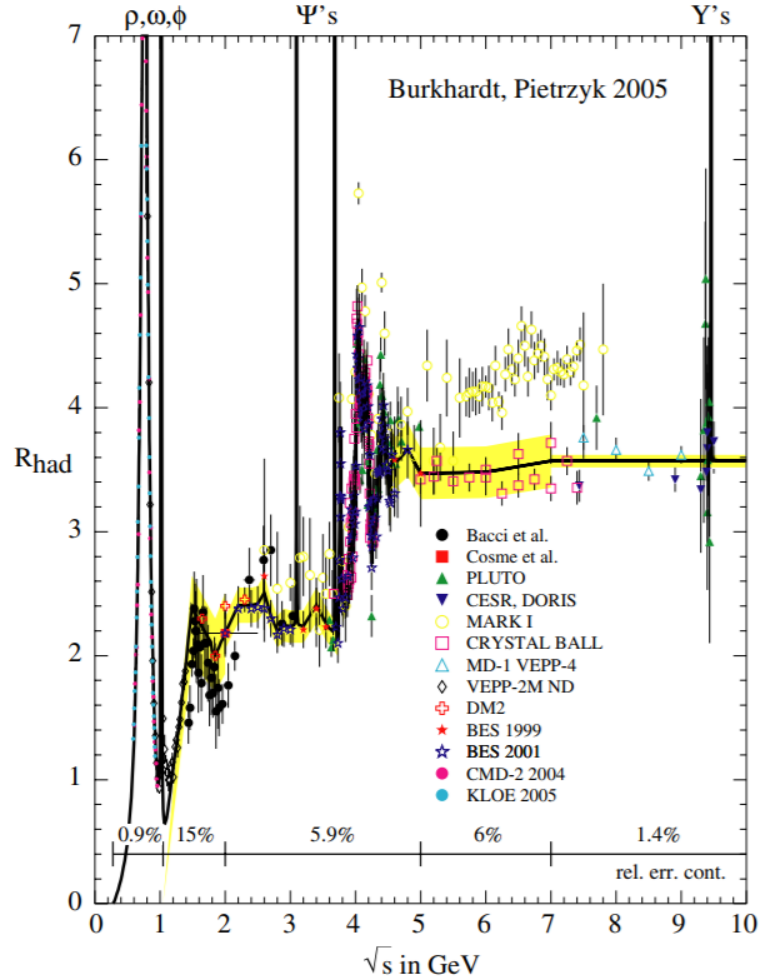
Figure 1.4: Measurements from different experiments for the R factor of hadrons are plotted against the centre of mass energy. [8]

In Figure 1.4 different measurements of the R factor are shown. At an energy of around $4\,\text{GeV}$ the R factor suddenly jumps to a higher value. Below this energy only the light quarks (u, d and s) can be produced and the R factor is approximately 2. Above this energy charm production sets in and R reaches a value of approximately 3.3. Considering only the three light quarks Equation 1.1 evaluates to:

$$R = N_c \cdot [Q_u + Q_d + Q_s] = N_c \cdot \left[\left(\frac{2}{3} \right)^2 + \left(-\frac{1}{3} \right)^2 + \left(-\frac{1}{3} \right)^2 \right] = N_c \cdot \frac{2}{3} \qquad (1.2)$$

With $R = 2$ it follows, that the number of colors N_c is equal to 3. [2, 7, 8]

The experimental evidence for the existence of gluons was provided in 1979 by the TASSO experiment located at the DESY e^+e^- storage ring PETRA. The TASSO collaboration analysed hadron jets from e^+e^- annihilation at energies between $13\,\text{GeV}$ and $31.6\,\text{GeV}$. They observed a large increase of transverse momentum with energy, in which the broadening of the jets is anisotropic around the azimuthal angle of the quarks. So called planar events, i.e. events with large transverse momenta in direction of the plane and small transverse momenta perpendicular to it, tend to be preferred. The rate of those events in the higher energies clearly exceeds the

(a) Two-jet event   **(b)** Three-jet event
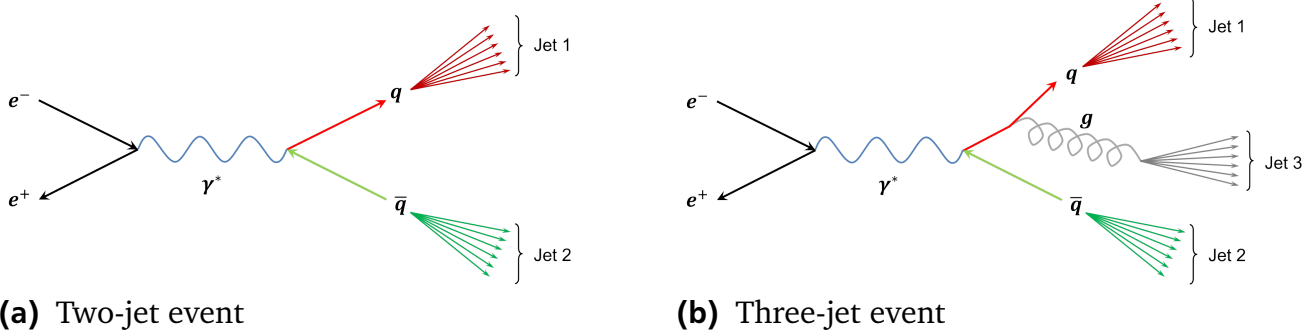
Figure 1.5: Feynman Diagrams for quark production from e^+e^- annihilation with (b) and without (a) additional gluon bremsstrahlung.

number of events predicted from statistical fluctuation of the $q\bar{q}$-jets. The strong broadening predominantly occurs in only one of the jets and goes along the theory prediction of gluon bremsstrahlung by one of the outgoing quarks. For sufficiently high transverse momenta of the radiated gluons the events yield a three-jet topology. The Feynman Diagram for quark pair production from e^+e^- annihilation including gluon bremsstrahlung $e^+e^- \rightarrow q\bar{q}g$ is shown in Figure 1.5b and Figure 1.6 depicts a characteristic three-jet event in momentum space.
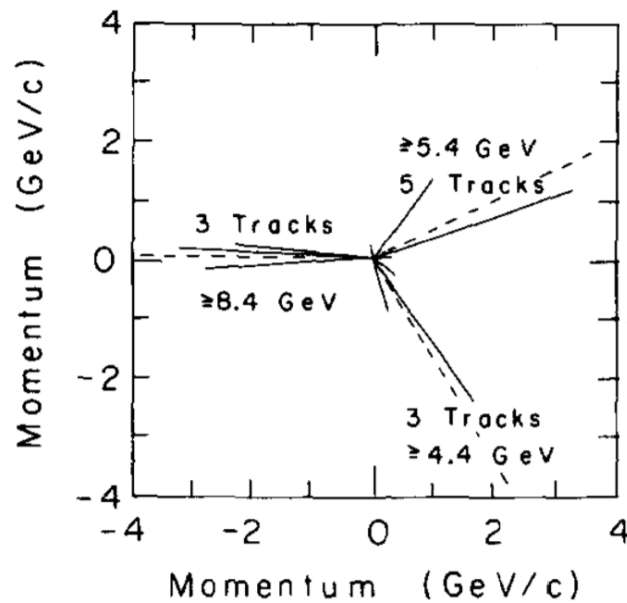
Figure 1.6: Momentum representation of a characteristic three jet event, projected in the $\hat{n}_2 - \hat{n}_3$-plane, which is the plane containing the largest momentum components. The $\hat{n}_i$ are the unit eigenvectors of the second-rank tensor constructed from the hadron momenta, associated with the smallest (i=1), intermediate (i=2) and largest (i=3) eigenvalues. [9]

The TASSO data are indeed in agreement with the theory calculations of three-jet events due to gluon bremsstrahlung from 1976, thus they provide the experimental evidence of gluons. [9–11]

1.3 Quantum Chromodynamics

The quarks are bound together via the exchange of gluons. In comparison to the electromagnetic interaction, whose mediator, the photon, is uncharged, the gluons itself are carrying (color-)charge, hence they not only interact with the quarks but also with each other. The quark and gluon interactions are described by the Lagrange density of QCD:

$$\mathcal{L}_{QCD} = \sum_j^{N_f} \bar{\psi}_j \left(i\gamma^\mu D_\mu - m_j \right) \psi_j - \frac{1}{4} G^a_{\mu\nu} G^{\mu\nu}_a \tag{1.3}$$

D_μ is the covariant derivative $D_\mu = \partial_\mu - igT_a A^a_\mu$ with the quark-gluon-coupling constant g, the gluon-fields A^a_μ and the generator T_a of the SU(3) gauge group. The ψ_j ($\bar{\psi}_j$) are the (adjoint) quark-field spinors the and γ^μ are the Dirac-matrices with $\mu = 1, ..., 3$. With the covariant derivative we can separate the Lagrangian into a kinetic part $\mathcal{L}_{kin}$, that represents the kinetic and mass terms for all of the fermion fields (i.e. the quarks) and a part $\mathcal{L}_{str}$ devoted to the strong interaction, that contains the kinetic terms and self interactions of the eight gluons as well as the strong interaction between quarks and gluons. Further using the slashed notation $\partial\!\!\!/ = \gamma^\mu \partial_\mu$ to abbreviate the contraction between the gamma matrices and ∂_μ leads to the following representation of the QCD Lagrangian:

$$\mathcal{L}_{QCD} = \underbrace{\sum_j^{N_f} \bar{\psi}_j \left(i\partial\!\!\!/ - m_j \right) \psi_j}_{\mathcal{L}_{kin}} + \underbrace{\sum_j^{N_f} g\bar{\psi}_j \gamma^\mu T_a \psi_j A^a_\mu - \frac{1}{4} G^a_{\mu\nu} G^{\mu\nu}_a}_{\mathcal{L}_{str}} \tag{1.4}$$

Applying the Euler-Lagrange-equation on the kinetic part, results in the Dirac equation, which provides the propagators for the quarks. The sum in $\mathcal{L}_{str}$ contains the potential for interaction with gluons, which is required to achieve gauge-invariance. And the field tensor $G^a_{\mu\nu}$ that contains the gluon-fields and the gluon-gluon interactions is given by

$$G^a_{\mu\nu} = \partial_\mu A^a_\nu - \partial_\nu A^a_\mu + gf^{abc} A^b_\mu A^c_\nu \tag{1.5}$$

where f^{abc} are the structure constants that determine the Lie brackets of all elements of the Lie algebra, for instance $[T_a, T_b] = if^{abc}T_c$. The first two summands form the non-interacting part, i.e. the propagators of the gluon fields, and the third summand contains the gluon-gluon-interaction. The the three- and four-gluon-gluon-interaction-vertices are obtained by a contraction between the field tensors (last summand of Equation 1.4)[1]. The sum in the Lagrangian runs over the number of all included quark flavors N_f and the m_j are their respective Higgs masses. [12]

---

[1] $G^a_{\mu\nu} G^{\mu\nu}_a = gf^{abc} A^b_\mu A^c_\nu \partial_\mu A^a_\nu - gf^{abc} A^b_\mu A^c_\nu \partial_\nu A^a_\mu \longrightarrow$ three-gluon-interaction-vertex
  $+ g^2 f^{abc} A^b_\mu A^c_\nu f^{ade} A^d_\mu A^e_\nu \longrightarrow$ four-gluon-interaction-vertex

1.3.1 Qualitative Characteristics of the Strong Interaction

The strong interaction exhibits some interesting features, that are strongly connected to the behavior of its coupling constant α_s, which leads to effects like asymptotic freedom and confinement.

Running Coupling

The name coupling *constant* might be misleading, as it in fact depends on Q^2. It is worth noting, that this is true for every coupling constant in quantum field theory, thus it also applies to the electromagnetic coupling α_{em} and the weak coupling α_w. However, the dependence for the latter two is very small. In contrast, the strong coupling constant α_s depends heavily on the value of Q^2. In Table 1.1 the measured values for α_{em} and α_s for varying Q^2 are presented and Figure 1.7 compares the strength of the three coupling constants.

measurement	$\sqrt{Q^2}$	α_{em}	α_s
Thompson scattering	$0\,\text{eV} - 1\,\text{eV}$	$\approx \frac{1}{137}$	/
τ - decay	$1.78\,\text{MeV} = M_{\tau^\pm}$	/	0.330 ± 0.014
JADE experiment	$45\,\text{GeV}$	$\approx \frac{1}{129}$	/
Z^0 decay	$91\,\text{GeV} = M_{Z^0}$	$\approx \frac{1}{128}$	0.1184 ± 0.0007

Table 1.1: Comparison of electromagnetic and strong coupling constant at different energies.
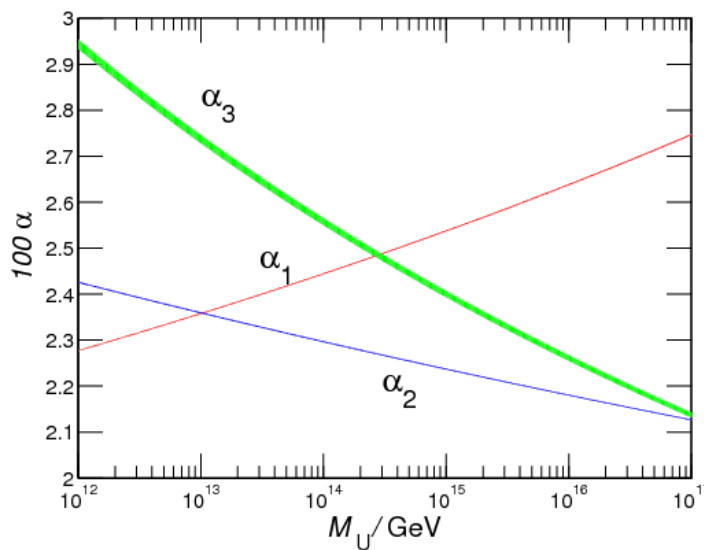
Figure 1.7: Running of the coupling constants of the electromagnetic (α_1), the weak (α_2) and the strong (α_3) interaction. [13]

An electric charge q is screened by virtual electron positron pairs, that group around it. Thus the effective charge is larger for short distances, i.e. large Q. The electromagnetic coupling constant therefore changes with the distance/energy like:

$$\alpha_{em} = \frac{q_{eff}^2}{4\pi\epsilon_0 hc} \tag{1.6}$$

In QCD additionally to the screening of a color charge by the surrounding cloud of virtual quark-antiquark pairs, color antiscreening occurs due to the self-coupling of the gluons. Since the second effect prevails, the effective charge is larger for large distances, i.e. small values of Q, leading to:

$$\alpha_s(Q) = \frac{6\pi}{33 - 2N_f} \log\left(\frac{\Lambda_{QCD}}{Q}\right) \tag{1.7}$$

where N_f denotes the number of flavors taken into account.

For very small distances, i.e. very high values of Q^2 the interquark coupling vanishes asymptotically, thus in the limit $Q^2 \to \infty$ the quarks can be considered free, which leads to the expression *asymptotic freedom*. For small values of Q^2 on the other hand, the coupling increases, leading to confinement which will be discussed more thoroughly in the next section.

Figure 1.8 shows an overview of different measurements of the strong coupling constant over a large range of Q, where the just described behavior becomes evident.
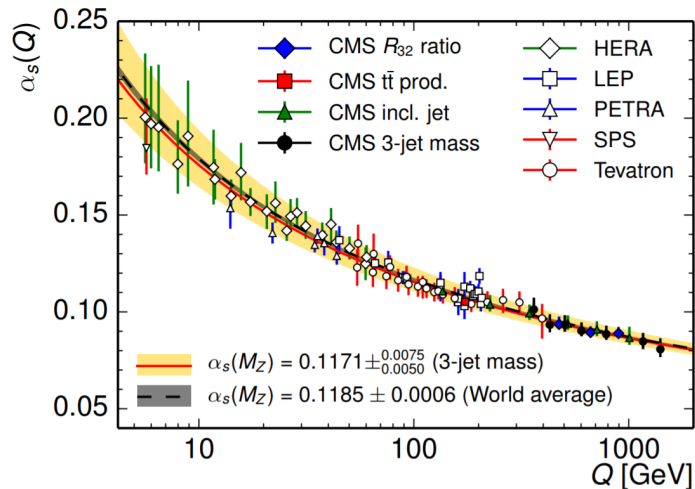
Figure 1.8: Measurement of the running coupling constant of the strong interaction. Data points are taken from electron-positron, electron-proton and proton-(anti)proton collider experiments. [14]

Confinement

In QED the constituent electrons and nuclei as well as the processes to release the constituents from their bound states, such as ionization, can be observed easily. In contrast, free quarks have never been seen, albeit applying collision energies several magnitudes above the rest energy of the strongly bound states. A solution to this conundrum might be the confinement hypothesis,

which states, that the only eigenstates with finite energy of the QCD Hamiltonian are color neutral. [12]

To draw a more comprehensible picture, consider a bound state of a quark and antiquark. As you try to pull them apart from each other, the coupling constant of the strong interaction increases. Thus to further separate them, a larger and larger amount of energy is necessary, until eventually this energy is sufficient to create a new quark-antiquark pair out of the vacuum. Subsequently the quark will be attracted to the original antiquark and form a bound state with it, as well as the antiquark and the original quark. Therefore the creation of isolated colored particles is impossible. This process is also associated with the term "string-breaking", as you can imagine the original pair being connected by a string, that is stretched out further and further, until it finally breaks. The distance at which this happens is called the confinement radius r_c, where the strong coupling $\alpha_s(\Lambda_c)$ becomes large at the scale $\Lambda_c = 1/r_c$. From the behavior of the strong coupling it is likely, that Λ_c is in the neighborhood of the scale of QCD Λ_{QCD} at the magnitude of several hundred MeV. Thus it follows, that the confinement radius is in the order of $10^{-15}\,\mathrm{m} = 1\,\mathrm{fm}$, which agrees with the size of a nucleon. [12, 15]

1.3.2 Symmetries of QCD

Symmetries play an important role in any theory, giving insight into its structure and leading to a qualitative understanding. There are different types of symmetry:

- **global symmetries** hold at all points of space time (e.g. C, P and T symmetry), while **local symmetries** vary from point to point. They are also called intrinsic symmetries and form the basis for gauge theories. (e.g. color symmetry)

- **continuous symmetries** are characterized by an invariance against continuous changes in the geometry of a system. They play an important role in Noether's Theorem for the derivation of conservation laws. (e.g. flavor symmetry)
  discrete symmetries on the other hand only hold for certain non-continuous changes in a system. (e.g. parity)

- symmetries can be **exact** or only **approximate**, which means, that one observes small violations of the consequences of the symmetry (e.g. quark masses in the QCD Lagrangian lead to chiral symmetry being only approximate)

- **anomalous symmetries** are symmetries, that are present in the classical state, but broken on a quantum level

- In **Wigner-Weyl symmetries** both the interaction and the physical state are invariant against the symmetry transformation.
  In **Nambu-Goldstone symmetries** only the interaction obeys the symmetry, but not the physical state. Such symmetries are also called spontaneously broken and an interesting feature is, that the symmetry pattern changes as a function of temperature. Thus at high temperatures the Nambu-Goldstone phase transitions into the Wigner-Weyl phase.

Besides the Poincaré symmetry, including CPT invariance (each of which is separately conserved), that every relativistic quantum field theory has, QCD also exhibits several internal symmetries. First to mention is the local gauge symmetry, i.e. the transformation of quarks and

gluons under color SU(3), that is a key requirement of the whole theory. The global symmetry in flavor space with N_f different flavors is called chiral symmetry. Particularly a SU(2) rotation in flavor space, acting on up and down quarks, leads to isospin symmetry and a U(1) rotation to baryon number conservation. And finally the center symmetry has to be mentioned, which is spontaneously broken in the deconfined phase. The different symmetries of QCD are summarized in Table 1.2. [16]

Symmetry	Vacuum	High T	Low T, high μ	Order parameter	Consequences
(Local) color SU(3)	Unbroken	Unbroken	Broken	Diquark condensate	Color super-conductivity
Z(3) center symmetry	Unbroken	Broken	Broken	Polyakov loop	Confinement/ Deconfinement
Scale invariance	Anomaly			Gluon condensate	Scale (Λ_{QCD}), running coupling
Chiral symmetry $U_L(N_f) \times U_R(N_f) = U_V(1) \times SU_V(N_f) \times SU_A(N_f) \times U_A(1)$					
$U_V(1)$	Unbroken	Unbroken	Unbroken	—	Baryon number conservation
Flavor $SU_V(N_f)$	Unbroken	Unbroken	Unbroken	—	Multiplets
Chiral $SU_A(N_f)$	Broken	Unbroken	Broken	Quark condensate	Goldstone bosons, no degenerate states with opposite parity
$U_A(1)$	Anomaly			Topological susceptibility	Violation of intrinsic parity

Table 1.2: Symmetries of QCD. [16]

In this chapter the focus is set on the chiral symmetry and the effects breaking it.

Chiral Symmetry

Considering only the light quarks - up, down and possibly strange - we can work within the low-energy approximation of the effective theory. It is important to mention, that the quarks involved are very light in comparison to the scale of QCD $(\Lambda_{QCD} \approx 200 - 400\,\text{MeV})$. Thus as a first approach we can consider the qarks as massless and introduce the non-zero masses later on as small corrections. This approximation with $m_{light} \to 0$ (and $m_{heavy} \to \infty$) is also called the chiral limit. Any symmetry of the Lagrangian in the chiral limit that is broken by the mass term, will then be only an approximate symmetry of the whole Lagrangian.

So as a first approach we will construct the symmetry group of the chiral Lagrangian, which can later be reduced. The kinetic term in Equation 1.4 with masses set to zero is invariant under the symmetry group $U(2N_f)$, where the factor two can be explained by the fact that

each Dirac fermion is made up of two Weyl (or Majorana) fermions. Furthermore, the required symmetry must not act in color space, but in flavor space only, since it has to commute with the SU(3) generators T_a in the covariant derivative, that act on the color indices of the quarks, to preserve gauge-invariance. The symmetry subgroup of $U(2N_f)$ that meets those conditions is the group $U_L(N_f) \times U_R(N_f)$. Decomposing the quark-field spinors into left- and right-handed components, leads to:

$$\mathscr{L}_{\text{QCD}} = \underbrace{\bar{\psi}\,(i\slashed{D} - m)\,\psi}_{} \quad - \quad \tfrac{1}{4}F_{\mu\nu}F^{\mu\nu} \qquad \text{with } \slashed{D} = \gamma^\mu D_\mu$$

$$\bar{\psi}_L i\slashed{D}\psi_L + \bar{\psi}_R i\slashed{D}\psi_R \qquad \longrightarrow \qquad \begin{array}{l}\text{Symmetric under independent rotations} \\ \text{ of left and right handed quarks}\end{array} \qquad (1.8)$$

$$\bar{\psi}_L m\psi_R + \bar{\psi}_R m\psi_L \qquad \longrightarrow \qquad \begin{array}{l}\text{Full Lagrangian } \underline{\text{NOT}} \text{ symmetric,} \\ \text{Symmetry only holds for chiral limit}\end{array}$$

Since we are only considering the three light quarks, N_f equals 3. To get to the full symmetry group, first any anomalies have to be cancelled. It is convenient to change the basis of the generators to

$$\underbrace{U_V(3)}_{U_{L+R}(3)} \times \underbrace{U_A(3)}_{U_{L-R}(3)}$$

which is isomorphic to the former basis. The corresponding symmetry transformation can be written as

$$\delta \begin{pmatrix} u \\ d \\ s \end{pmatrix} = \left[\frac{i}{2}w_V^a \lambda_a + \frac{i}{2}w_A^a \lambda_a \gamma_5 \right] \begin{pmatrix} u \\ d \\ s \end{pmatrix} \qquad (1.9)$$

where the λ_a are the Gell-Mann matrices and $w_V = \frac{w_L + w_R}{2}$, $w_A = \frac{w_L - w_R}{2}$ are the group parameters. The Dirac matrix $\gamma_5 = i\gamma_0\gamma_1\gamma_2\gamma_3$ can be used to construct two projection operators $P_L = \frac{1}{2}(1 + \gamma_5)$ and $P_R = \frac{1}{2}(1 - \gamma_5)$ that project onto the left- and right-handed components of each quark field.

While the vector combination, which is independent from γ_5, rotates left- and right-handed quarks alike, the axial generators are explicitly proportional to γ_5, thus they act with opposite sign on left- and right-handed quarks. Since the vector generators treat left-and right-handed quarks equally, only the axial transformations can be anomalous. However, the only non anomaly-free symmetries are axial symmetries for which the trace is not vanishing. The U(3) group is generated by arbitrary 3×3 Hermitian matrices, each of which can be written as a linear combination of the eight traceless Gell-Mann matrices λ_a, $a = 1 \ldots 8$ (Eq: 1.10) and the (normalized[2]) unit matrix (λ_0), hence the Lie algebra for U(3) is equivalent to that of $SU(3) \times U(1)$. It follows, that the sole anomalous generator of $U_L(3) \times U_R(3)$, that does not survive quantization, is the axial λ_0 generator $U_A(1)$. In combination with the vector part of the

---

[2]   The normalization is necessary to ensure, that the nine matrices satisfy the orthonormalization condition $\text{tr}(\lambda_a \lambda_b) = 2\delta_{ab}$

group, the full anomaly-free symmetry group of the Lagrangian in the chiral limit is given by $G = SU_L(3) \times SU_R(3) \times U_V(1)$.

$$\lambda_0 = \sqrt{\frac{2}{3}} \begin{pmatrix} 1 & 0 & 0 \\ 0 & 1 & 0 \\ 0 & 0 & 1 \end{pmatrix} \qquad \lambda_1 = \begin{pmatrix} 0 & 1 & 0 \\ 1 & 0 & 0 \\ 0 & 0 & 0 \end{pmatrix} \qquad \lambda_2 = \begin{pmatrix} 0 & -i & 0 \\ i & 0 & 0 \\ 0 & 0 & 0 \end{pmatrix}$$

$$\lambda_3 = \begin{pmatrix} 1 & 0 & 0 \\ 0 & -1 & 0 \\ 0 & 0 & 0 \end{pmatrix} \qquad \lambda_4 = \begin{pmatrix} 0 & 0 & 1 \\ 0 & 0 & 0 \\ 1 & 0 & 0 \end{pmatrix} \qquad \lambda_5 = \begin{pmatrix} 0 & 0 & -i \\ 0 & 0 & 0 \\ i & 0 & 0 \end{pmatrix} \qquad (1.10)$$

$$\lambda_6 = \begin{pmatrix} 0 & 0 & 0 \\ 0 & 0 & 1 \\ 0 & 1 & 0 \end{pmatrix} \qquad \lambda_7 = \begin{pmatrix} 0 & 0 & 0 \\ 0 & 0 & -i \\ 0 & i & 0 \end{pmatrix} \qquad \lambda_8 = \frac{1}{\sqrt{3}} \begin{pmatrix} 1 & 0 & 0 \\ 0 & 1 & 0 \\ 0 & 0 & -2 \end{pmatrix}$$

Chiral Symmetry Breaking

The $U_V(1)$ subgroup, that is responsible for baryon number conservation is the only exact symmetry of the QCD Lagrangian, i.e. it remains a symmetry when extended to the rest of the Standard Model. All the other symmetries are broken, either explicitly by other terms in the Lagrangian, most importantly to mention are the non-zero quark masses, or by mixed anomalies with the electromagnetic or weak gauge interactions.

Due to the non-zero quark-mass terms which are invariant under axial transformations, the chiral symmetry is broken. The mass terms break all axial elements $SU_A(3)$ of the $U_L(3) \times U_R(3)$ symmetry. In addition also most of the vector transformations are broken, which leads to the fact, that rotations of one quark type into another are not preserved. The number of up, down and strange quarks on the other hand is. Considering the masses of up and down quark to be significantly smaller than the mass of the strange quark rises the expectation, that the axial elements of the $U_L(2) \times U_R(2)$ symmetry group are much less strongly broken than the ones involving three quarks.

Breaking of the Vector Subgroup

The vector subgroup of the symmetry is often also called flavor $SU_f(3)$, since its generators act in flavor space. And its subgroup, the $SU_V(2)$ group, that only shuffles the u and d quarks, can also be identified with the isospin symmetry ($SU_I(2)$). Symmetries, that are not spontaneously broken, leave the ground state invariant and it is predicted, that particle states related by such a symmetry must have the same mass, i.e the states degenerate. These degeneracies were already mentioned in Section 1.2 in the context of Gell-Mann's eightfold way. Since the symmetry is not exact, the masses will not be completely equal, instead they will differ by approximately 20 % within the $SU_L(3) \times SU_R(3)$ group and around 1 % for the elements of the $SU_I(2)$.

The change of the quark mass matrix

$$M_q = \begin{pmatrix} m_u & & \\ & m_d & \\ & & m_s \end{pmatrix}$$

under the vector part of the transformation in Equation 1.9 is

$$\delta M_q = \frac{i}{2} w_V^a [M_q, \lambda_a] \tag{1.11}$$

This vanishes only for λ_0, λ_3 and λ_8, corresponding to three linear combinations of up, down and strange number, which are preserved. As an example we can take a look at the mesons. The nine possible flavor states are summarized in a 3×3 hermitian matrix

$$\mathcal{M} = \begin{pmatrix} u \\ d \\ s \end{pmatrix} \begin{pmatrix} \bar{u} & \bar{d} & \bar{s} \end{pmatrix} = \begin{pmatrix} u\bar{u} & u\bar{d} & u\bar{s} \\ d\bar{u} & d\bar{d} & d\bar{s} \\ s\bar{u} & s\bar{d} & s\bar{s} \end{pmatrix} \tag{1.12}$$

$\mathcal{M}$ can be expanded in terms of the generators λ_a to obtain the irreducible representation of the flavor group: $3 \otimes \bar{3} = 8 \oplus 1$. The flavor invariant singlet state is caused by λ_0 being proportional to the unit matrix. The flavor octet arises, because all Gell-Mann-Matrices commute by definition, so they form an eight-dimensional representation. The expansion of $\mathcal{M}$ can be written as:

$$\mathcal{M} = \sum_{a=0}^{8} \mu_a \lambda_a$$

$$= \begin{pmatrix} \mu_3 + \frac{1}{\sqrt{3}}\mu_8 + \sqrt{\frac{2}{3}}\mu_0 & \mu_1 - i\mu_2 & \mu_4 - i\mu_5 \\ \mu_1 + i\mu_2 & -\mu_3 + \frac{1}{\sqrt{3}}\mu_8 + \sqrt{\frac{2}{3}}\mu_0 & \mu_6 - i\mu_7 \\ \mu_4 + i\mu_5 & \mu_6 + i\mu_7 & -\frac{2}{\sqrt{3}}\mu_8 + \sqrt{\frac{2}{3}}\mu_0 \end{pmatrix} \tag{1.13}$$

$$= \begin{pmatrix} \pi^0 + \frac{1}{\sqrt{3}}\eta_8 + \sqrt{\frac{2}{3}}\eta_1 & \sqrt{2}\pi^+ & \sqrt{2}K^+ \\ \sqrt{2}\pi^- & -\pi^0 + \frac{1}{\sqrt{3}}\eta_8 + \sqrt{\frac{2}{3}}\eta_1 & \sqrt{2}K^0 \\ \sqrt{2}K^- & \sqrt{2}\bar{K}^0 & -\frac{2}{\sqrt{3}}\eta_8 + \sqrt{\frac{2}{3}}\eta_1 \end{pmatrix}$$

In Table 1.3 the valence-quark content of each particle type, that is determined via comparison between the flavor eigenstates in Equation 1.13 and the possible quark combinations in Equation 1.12, and their respective masses are summarized. [12, 17]

Pseudoscalar Mesons	Valence-Quark Content	Experimental Masses (PDG)
$\pi^0 = \mu_3$	$\frac{1}{\sqrt{2}}\left(u\bar{u} - d\bar{d}\right)$	$m_{\pi^0} = 134.9770 \pm 0.0005\,\text{MeV}$
$\pi^+ = \frac{1}{\sqrt{2}}\left(\mu_1 - i\mu_2\right)$	$u\bar{d}$	$m_{\pi^+} = 139.57061 \pm 0.00024\,\text{MeV}$
$\pi^- = \frac{1}{\sqrt{2}}\left(\mu_1 + i\mu_2\right)$	$d\bar{u}$	$m_{\pi^-} = 139.57061 \pm 0.00024\,\text{MeV}$
$K^+ = \frac{1}{\sqrt{2}}\left(\mu_4 - i\mu_5\right)$	$u\bar{s}$	$m_{K^+} = 493.677 \pm 0.016\,\text{MeV}$
$K^- = \frac{1}{\sqrt{2}}\left(\mu_4 + i\mu_5\right)$	$s\bar{u}$	$m_{K^-} = 493.677 \pm 0.016\,\text{MeV}$
$K^0 = \frac{1}{\sqrt{2}}\left(\mu_6 - i\mu_7\right)$	$d\bar{s}$	$m_{K^0} = 497.611 \pm 0.013\,\text{MeV}$
$\bar{K}^0 = \frac{1}{\sqrt{2}}\left(\mu_6 + i\mu_7\right)$	$s\bar{d}$	$m_{\bar{K}^0} = 497.611 \pm 0.013\,\text{MeV}$
$\eta_8 = \mu_8$	$\frac{1}{2\sqrt{3}}\left(u\bar{u} + d\bar{d} - 2s\bar{s}\right)$	$m_\eta = 547.862 \pm 0.017\,\text{MeV}$
$\eta_1 = \mu_0$	$\frac{1}{\sqrt{6}}\left(u\bar{u} + d\bar{d} + s\bar{s}\right)$	$m_{\eta'} = 957.78 \pm 0.06\,\text{MeV}$

Table 1.3: Valence-quark content and masses of the nine pseudoscalar mesons. For the η and η' mixing of the eigenstates η_1 and η_8 occurs due to the weak and electromagnetic forces. However, since the mixing angle is small, the contribution of the respective other eigenstate is on the level of a few percent. So one can approximately state $\eta \approx \eta_8$ and $\eta' \approx \eta_1$.

The η_1 corresponds to the above mentioned $SU_f(3)$ singlet state and the pseudoscalar meson octet consists of π^0, $\pi^\pm$, $K^0, \bar{K}^0$, $K^\pm$ and η_8. In the chiral limit all mesons within the octet would have degenerated masses. Of course this is not the case. But since $(m_d - m_u) \ll (m_s - m_d)$ the isospin symmetry $SU_I(2)$ is a much better approximation. The isospin generators are given by the first three Gell-Mann matrices ($\lambda_{1,2,3}$) which leads to the pions forming an isospin triplet. Furthermore there exist two isospin doublets (K^+, K^0) and (K^-, $\bar{K}^0$). In fact, the mass split within those isospin multiplets is of the order of the predicted $1\,\%$ and the deviation within the octet is of the order of the estimated $20\,\%$. The appearance of the meson spectrum provides evidence that the QCD ground state does indeed not spontaneously break the vector subgroup $SU_f(3)$.[12, 18]

The much larger mass of the η' arises due to the explicit breaking of the $U_A(1)$ subgroup by the previously discussed quantum anomaly [19].

Breaking of the Axial Subgroup

In contrast to the vector subgroup of the QCD symmetry, the ground state of the axial subgroup is not a singlet, so the $SU_A(3)$ symmetry is spontaneously broken. Thus particles related by this symmetry do not necessarily have equal masses. This is experimentally supported by the fact, that all the observed mesons exactly agree with the particle content, that is predicted by the $SU_f(3)$ multiplets. However, a spontaneously broken symmetry yields some other interesting

features. In case of the chiral symmetry the most important one is the existence of massless Goldstone particles [3]. Since the chiral symmetry is not exact, the effects that explicitly break the symmetry can generate mass for them, resulting in so-called pseudo-Goldstone particles, that are substantially lighter than the rest of the hadron spectrum, albeit not massless. To derive the properties of such a Goldstone particle, besides its low mass, we will take a look at Goldstone's theorem:

> *(...) if there is continuous symmetry transformation under which the Lagrangian is invariant, then either the vacuum state is also invariant under the transformation, or there must exist spinless particles of zero mass. [20]*

Denote the conserved current of such a Lagrangian by j_μ, the corresponding conserved charge by $Q = \int d^3x\, j^0$ and the transformation operator by $R(\omega) = i \int d^3x\, \omega(x) j^0(x)$. Then the change in a field $|\psi\rangle$ is $\delta |\psi\rangle = R(\omega) |\psi\rangle$ and the change in a field operator F is $\delta F(x) = [R(\omega), F(x)]$. A symmetry is spontaneously broken by definition, if the ground state $|\Omega\rangle$ is not invariant under the transformation R: $\delta |\Omega\rangle = R(\omega) |\Omega\rangle \neq 0$. However, it is more convenient to work with the order parameter $\delta F(x)$, that is the variation of the field operator and for which the expectation value in the ground state does not vanish, $\langle\Omega| \delta F(x) |\Omega\rangle \neq 0$, since $R(\omega) |\Omega\rangle = 0$ implies $\langle\Omega| \delta F(x) |\Omega\rangle = 0$. From the nonzero expectation value it follows, that there must exist an energy eigenstate $|G(p,n)\rangle$, for which the matrix element $\langle G(p,n)| R(\omega) |\Omega\rangle \neq 0$. Since R is an internal symmetry, it commutes with the Poincaré transformations. Combining this with the Lorentz invariance of the ground state leads to $|G\rangle$ being a spinless state: $\langle G(p,n)| j^0(x) |\Omega\rangle \neq 0$ with the rotational scalar j^0. Furthermore $|G(p,n)\rangle$ has to be massless ($p^2 = p^\mu p_\mu = 0$) to fulfill current-conservation $\partial_\mu j^\mu = 0$. Additionally the Goldstone state must be a pseudoscalar, since the theory is parity-invariant and j^μ is an axial vector.

So in conclusion it is expected to find $N_f^2 - 1$ spinless pseudoscalar mesons with masses much lighter than the rest of the hadron spectrum. Considering the three quark flavors u, d and s leads to eight pseudo-Goldstone bosons, that are consistent with the pseudoscalar meson octet. Since the axial symmetry $SU_A(2)$ that only involves the u and d quarks, is much less strongly broken, the three pions are very light with masses that are by a factor 3 to 4 smaller than the ones of the other members of the pseudoscalar octet. Thus most of the time with the term *Goldstone bosons* not the whole meson octet is meant, but just π^0 and $\pi^\pm$.

The ground state $|\Omega\rangle$ is also called the vacuum state and the reason, why its variation $\delta |\Omega\rangle$ does not vanish, is the existence of the so called chiral condensate. This chiral condensate arises due to the attraction between virtual quarks and antiquarks of opposite chirality, thus it is a measure for the coupling between left- and right-handed quarks. The above mentioned order parameter $\delta F(x)$ is indeed the quark condensate, thus we can rewrite the vacuum expectation value as

$$\langle\Omega| \delta F(x) |\Omega\rangle = \langle q\bar{q}\rangle = \langle (\bar{q}_L + \bar{q}_R)(q_L + q_R)\rangle = \langle \bar{q}_R q_L + \bar{q}_L q_R\rangle \neq 0 \qquad (1.14)$$

where $\langle q\bar{q}\rangle$ denotes the quark (chiral) condensate and the projection operators are used to split the quark field into left and right handed components. The expectation value is of the order of $\langle q\bar{q}\rangle \approx \Lambda_{QCD}^3$, thus it is large in comparison to the scale of QCD. [21]

---

[3] In fact *every* spontaneously broken continuous symmetry implies the existence of massless states, not only the chiral symmetry we focus on here.

The chiral condensate can be connected to the bare quark mass, the pion mass and the pion decay constant $f_\pi = 93\,\text{MeV}$ via the Gell-Mann-Oakes-Renner relation [22]:

$$m_\pi^2 f_\pi^2 \;=\; m_q \langle q\bar{q} \rangle \tag{1.15}$$

It is expected, that high temperatures or baryon chemical potentials induce the chiral condensate to melt, $\langle q\bar{q} \rangle \to 0$, thus the chiral symmetry is restored. This will be discussed in more detail in the subsequent section.

The chiral condensate also gives an explanation for the huge difference between the constituent quark mass of around $m_{q_{const}} \approx \frac{1}{3} m_{\text{Nucleon}} \approx 300\,\text{MeV}$ and the bare quark mass that is of the order of a few MeV for the u and d quark. One can interpret the constituent or valence quarks as quarks dressed with the virtual quark antiquark pairs and and gluons from the chiral condensate. The measured mass of the quarks depends on the distance over which it is probed, since the coupling strength decreases when two quarks come closer to each other and therefore the measured mass will also be smaller.

Chiral Symmetry Restoration

The chiral condensate, introduced in the section above, characterizes the vacuum state of QCD but changes within the medium. To estimate those modifications, the thermal medium is approximated as a gas of non-interacting light hadrons, i.e. pions at finite temperature T and nucleons at finite density ρ_N. A linear density expansion of the quark condensate leads to [23]:

$$\frac{\langle\langle q\bar{q} \rangle\rangle (T, \mu_B)}{\langle q\bar{q} \rangle} \;\approx\; 1 - \frac{T^2}{8 f_\pi^2} - \frac{1}{3}\frac{\rho_N}{\rho_0} - \cdots , \qquad \rho_0 \approx 0.16\,\text{fm}^{-3} \tag{1.16}$$

Besides the quark-antiquark condensate, the gluon condensate $\langle\langle G^2 \rangle\rangle$ plays an important role, since it substantially contributes to the dynamic mass generation of the nucleons. It can be expanded in a similar way, thus both the quark and the gluon condensate show a clear dependence on temperature and density. Their behavior is shown in the plots in Fig 1.9.
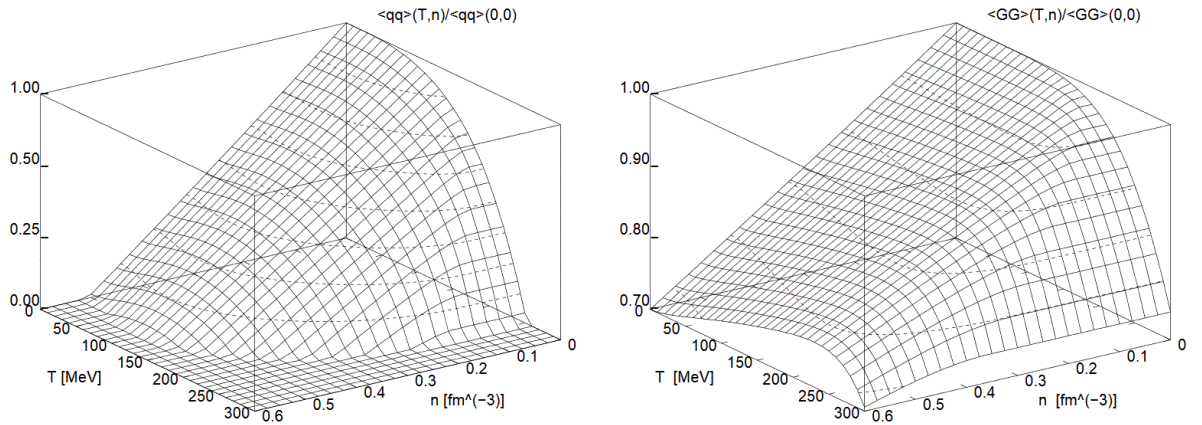
Figure 1.9: Temperature and density dependence of the quark (left panel) and the gluon condensate (right panel), normalized to their vacuum value. [23]

Where the quark condensate vanishes, chiral symmetry is restored. This means, that in contrast to the ground state, the state at high energy/density possesses the same symmetries as the Hamiltonian. As a consequence Goldstone modes should not be present anymore, thus the pions should become as massive as the other hadrons. Furthermore chiral partners must degenerate, hence the mass split between those states (e.g. ρ (770 MeV) and a_1 (1260 MeV), or N (940 MeV) and N* (1535 MeV)) of about 500 MeV should vanish. Since the chiral restoration and the deconfinement phase transition take place at approximately the same temperature[4], hadrons are of course not a good measure. Therefore the preferred experimental observable is the mass of chiral partners, especially vector mesons, since they decay into dileptons, which are experimentally accessible. The use of electromagnetic probes in heavy ion collisions is subject of chapter 1.4.1. [23–25]

1.3.3 The QCD Phase Diagram

The properties of strongly interacting matter, depending on temperature and density, can be summarized in the QCD phase diagram. It is roughly divided into three different regions: hadronic matter at low temperatures and densities, Quark-Gluon-Plasma (QGP) at high temperatures and Color Superconductors at high densities. Figure 1.10 shows data points from the various experiments, that aim for creating matter at different T-ρ-points. Except for the red triangle, that was measured by the NA60 collaboration, all data points represent the conditions at freezeout. The NA60 experiment measured dileptons which show a higher temperature than the hadrons, since they shine from within the fireball. In general, experiments with very high beam energies produce matter at high temperatures and low baryon chemical potentials, resembling properties like in the early universe, a few microseconds after the Big Band. At lower beam energies, matter at moderate temperatures but high baryon chemical potentials is created, as it might be found in the core of neutron stars or even neutron star mergers.

Up until now the nature of the phase transition between hadronic matter and the Quark-Gluon-Plasma is not yet understood and different theories provide different predictions on the position of a critical point as well as its existence at all. In Figure 1.11 two possible scenarios for the appearance of the QCD phase diagram are shown. According to lattice QCD calculations a first order phase transition is expected up to a certain temper-
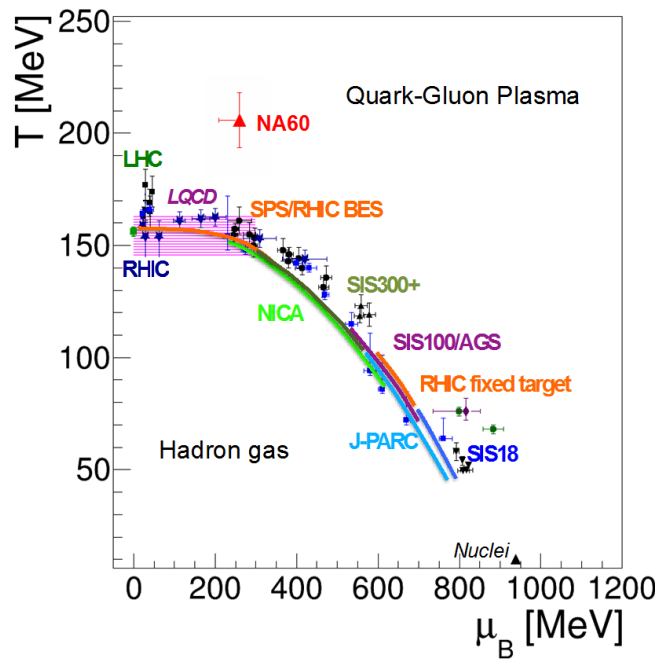
Figure 1.10: The plot shows the phase diagram of QCD matter and the different T-ρ regions of various experiments [26].

---

[4]   It is not yet fully understood, why chiral and deconfinement phase transition occur at the same temperature. This holds true for $\mu_B = 0$, while at finite baryochemical potentials the temperatures are not yet determined.
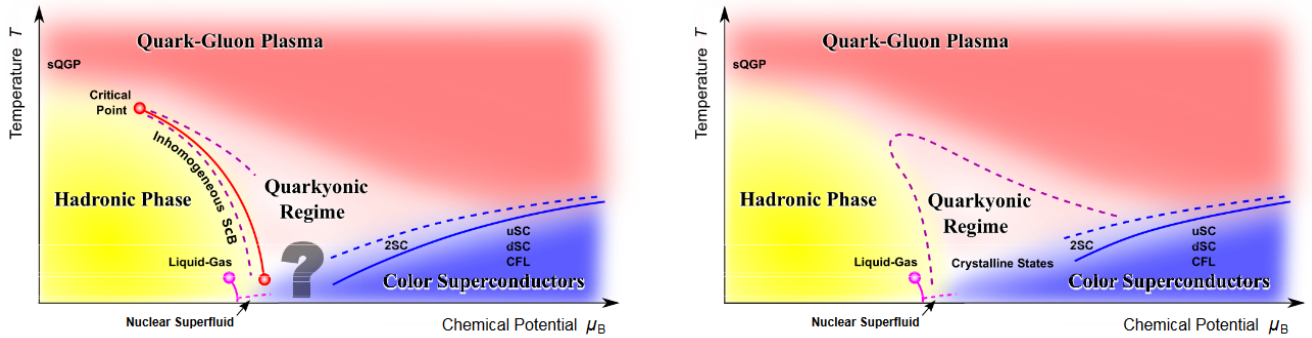
Figure 1.11: Two possible scenarios for a QCD phase diagram. The left panel shows a first order phase transition (red line) and critical points and the left panel displays a version without a first order phase transtion [27].

ature above which a smooth cross-over should take place. With increasing baryon chemical potential the gas like behavior of the QCD matter should become liquid-like via a first order phase transition. Calculations with an infinite number of colors predict another state of matter, called the Quarkonic regime, where the matter is still confined, but chiral symmetry is already restored. Besides the deconfinement phase transition, Figure 1.11 independently indicates the chiral transition (pink dashed line), which is most likely to be a smooth cross-over.

1.4 Heavy Ion Collisions

As mentioned before, a way to access the QCD phase diagram in the laboratory are Heavy Ion Collisions (HIC). One can distinguish between collider experiments, where two beams of heavy ions are crossed in the detector region and fixed target experiments, where a heavy ion beam is shot into a target. Since the former set up allows for the highest energies, it is able to create extremely high temperatures at very low baryon chemical potentials (e.g. experiments at LHC and RHIC). In the latter one on the other hand, especially at lower beam energies, the matter is rather compressed than heated (e.g. experiments at SIS18), resulting in the other extreme with moderate temperatures but highest baryon chemical potentials. See Figure 1.10 for more detailed information on the various experiments performed to explore the different regions of the QCD phase diagram.

In Figure 1.12 a schematic view of a heavy ion collision is shown, displaying the different stages the colliding nuclei go through.

As the two (Lorentz-contracted) nuclei approach each other, in ultra-relativistic collisions a state named Color Glass Condensate (CGC) forms, where high transverse momentum particles are suppressed at forward rapidity (e.g. d+Au collisions at $\sqrt{s_{NN}} = 200\,\text{GeV}$) [29]. Subsequently, as the nuclei touch, hard scattering of quarks and gluons occurs and depending on the energy of the collision, prompt photons, Drell-Yan dileptons and jets as well as heavy quarks are produced. Within a short time ($\tau \approx 1\,\text{fm/c}$) after these first chance collisions, the system thermalizes and prethermal photons and dileptons are created and with sufficiently large energy also QGP. Due to large pressure gradients, the fireball starts to expand hydrodynamically, accompanied by the formation of collective flow, jet quenching and the production of thermal photons and dileptons. With decreasing temperature and pressure hadronization sets in (if QGP was produced), the mean free path between hadrons increases until freezeout takes place. In
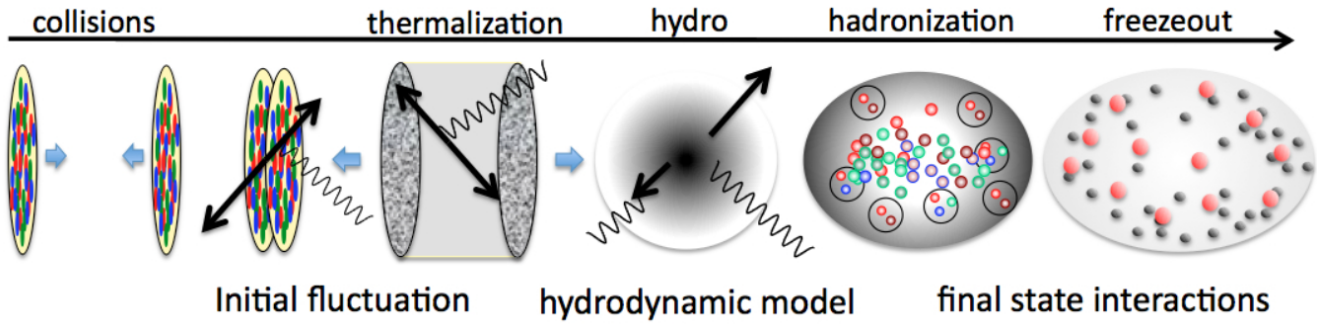
Figure 1.12: Schematic view of the stages of a heavy ion collision [28].

this last stage, final state interactions come into play. Figure 1.13 summarizes the different states the matter undergoes during the collision. [28, 30–33]
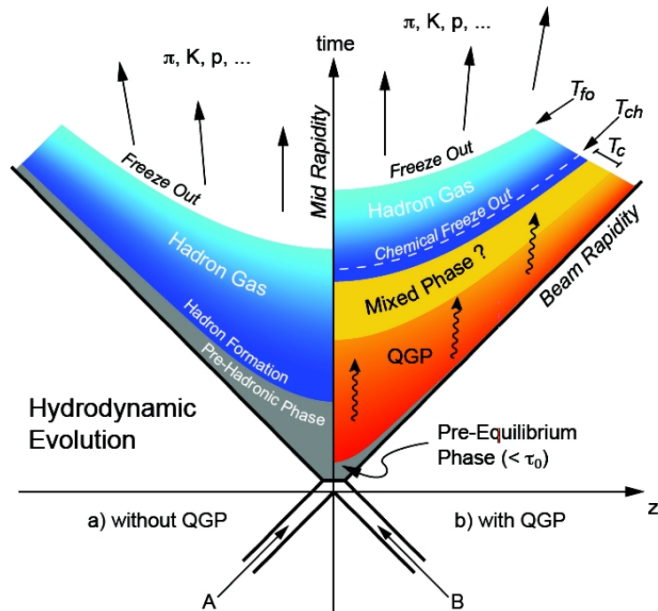
Figure 1.13: Evolution of a heavy ion collision with (b) and without (a) formation of QGP [34].

Since nuclei are extended objects, consisting of protons and neutrons, not every nucleon takes place in the collision. Instead only the nucleons in the overlap region are participating, while the other ones, called spectators, are leaving the collision zone rather unaffected. The size of this overlap region is characterized by the impact parameter b, which is the distance between the centers of the two nuclei. The smaller b is, the larger the overlap region and the more central the collision, which also leads to a higher particle multiplicity in the detector. The left side of Figure 1.15 shows the reaction plane, that is the plane spanned by the vector along the beam axis and the impact parameter. This plane changes from event to event, since the impact parameter varies, thus it has to be determined for each event. In the same figure also the two colliding nuclei are shown and the overlap region with the participants is indicated. If collisions with all possible impact parameters $0 \leq b \leq b_{max}$ are measured, the data is called minimum bias. Often the collisions are split into several centrality classes, depending on the number of nucleons taking part in the collision (A_{part}).

Virtual photons, that decay into dileptons are penetrating probes, because they are capable of directly accessing the interior of the fireball produced in a heavy ion collision. Since dileptons are produced continuously throughout the entire collision evolution, they provide information on the various stages of the collision. In contrast to hadrons, the most abundantly produced particles in HICs, dileptons do not undergo the strong interaction, thus they can escape freely from the collision zone after hadronisation. All this lead to the fact, that dileptons carry very rich physics information. The downside, on the other hand, is that it can be difficult to disentangle interesting from trivial sources of dilepton radiation and that only an integral yield over the various stages of the collision can be measured. [35, 36]
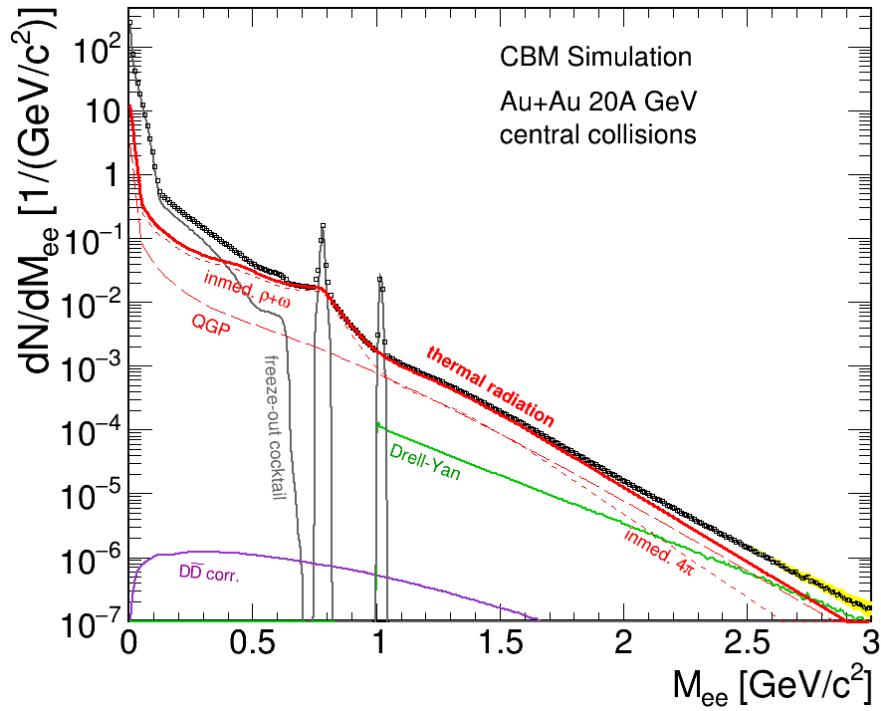
Figure 1.14: CBM simulation for Au+Au collisons at $20A$ GeV. Besides the dilepton signal the different contributions to it are shown [37].

In Figure 1.14 the invariant mass spectrum of the dilepton radiation simulated for Au+Au collisions at 20 A GeV is shown. In the very first stage of the collision the two nuclei begin to overlap and Drell-Yann quark-antiquark annihilation takes place: $q\bar{q} \rightarrow e^+e^-X$. This process, as well as the production of heavy flavors, contributes to the high mass region of the dilepton spectrum beyond $3\,\mathrm{GeV/c^2}$, which can only be measured by high-energy experiments. In the intermediate mass region between 1 and $3\,\mathrm{GeV/c^2}$, the main contribution to the dilepton invariant mass spectrum can be summarized as medium radiation. This medium radiation consists of quark-antiquark annihilation directly from the QGP, if the energy is high enough to produce quark-gluon plasma, and of in-medium vector mesons like the ρ or the ω. This intermediate mass region allows for a non-blue-shifted temperature measurement, unlike the effective temperature extracted from the transverse momentum spectra. Finally, the low mass region below $1\,\mathrm{GeV/c^2}$ originates from the latest phase of the collision evolution due to final state decays,

which are dominated by (Dalitz) decays of baryonic resonances and pion annihilation. However, at the low SIS18 beam energies excess radiation also dominates the spectrum below $1\,\mathrm{GeV/c^2}$, making this especially interesting to investigate. [38, 39]

1.4.2 Collective Flow

Not only the properties of individual particles can be measured, but also common properties that are exhibited by a large number of outgoing particles. Those common properties are called collective observables and they are used in heavy ion collisions to describe the quasi-macroscopic properties of nuclear matter. In particular, collective flow summarizes collectivity for kinematic observables, like the velocity or direction of ejectiles. Two types of collective flow may be distinguished: radial flow, that describes the common transverse velocity β_T, thus it affects the thermal spectra of the outgoing particles and anisotropic flow, which affects the spatial orientation of the particle momenta. The right side of Figure 1.15 shows the creation of flow in collisions at SIS18 energies.
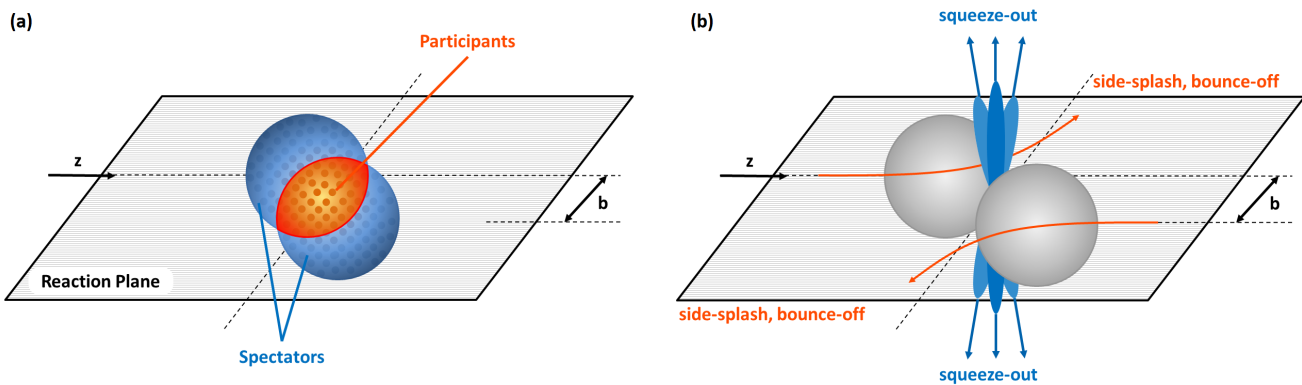
Figure 1.15: Colliding nuclei with finite impact parameter b. Part (a) shows the reaction plane, defined by impact parameter and beam axis as well as the participant- and spectator-nucleons. In part (b) the creation of collective flow in such a non-central collision is displayed.

While the radial flow is well established and used by measuring the effective temperature $T_{\mathrm{eff}} = T + M \langle \beta_T \rangle^2$ [40] it also holds some difficulties regarding to dileptons. Since dileptons are produced and emitted throughout the entire collision evolution, their p_T spectra are a superposition of all fireball stages with high temperatures but low transverse velocities at early times and low temperatures but high transverse velocities for the later stages. Thus the final spectra emerge from space-time-folding over the entire $T-\beta_T$ history of the fireball from $T_i \rightarrow T_f$, which makes it difficult to disentangle early and late emission sources.

The anisotropic flow, on the other hand, does not show this implicit time dependence of the effective temperature, while containing the same information. Instead the azimuthal anisotropy at high energies is small in the early phases of the fireball evolution, where the flow is not yet fully developed, and grows larger in the later phases. For smaller energies where different mechanisms lead to the formation of flow, the time evolution is not finally resolved yet. The mechanisms which generate azimuthal anisotropies at different energies are discussed at the end of this section.

Since there is no implicit time dependence, studying the azimuthal anisotropy of dileptons can

therefore give an insight into the time evolution of collectivity in the system without the necessity to deal with the complex superposition of different variables. [35, 41, 42]

The anisotropic flow can be described by a Fourier expansion of the azimuthal angle $\Delta\phi$ between the reaction plane and the dilepton pair [43]:

$$\frac{dN}{d\Delta\phi} \propto 1 + 2\sum_{n=1}^{\infty} v_n \cos(n\Delta\phi) \tag{1.17}$$

The flow coefficients v_1 (directed flow), v_2 (elliptic flow), v_3 (triangular flow) and higher orders are defined as the Fourier coefficients of this expansion. And the sine terms vanish due to the reflection symmetry with respect to the reaction plane. In Figure 1.16 such a Fourier expansion is fitted to the dilepton $\Delta\Phi$-distribution below $120\,\text{MeV/c}^2$ and additionally the first two Fourier coefficients v_1 and v_2 are plotted separately.
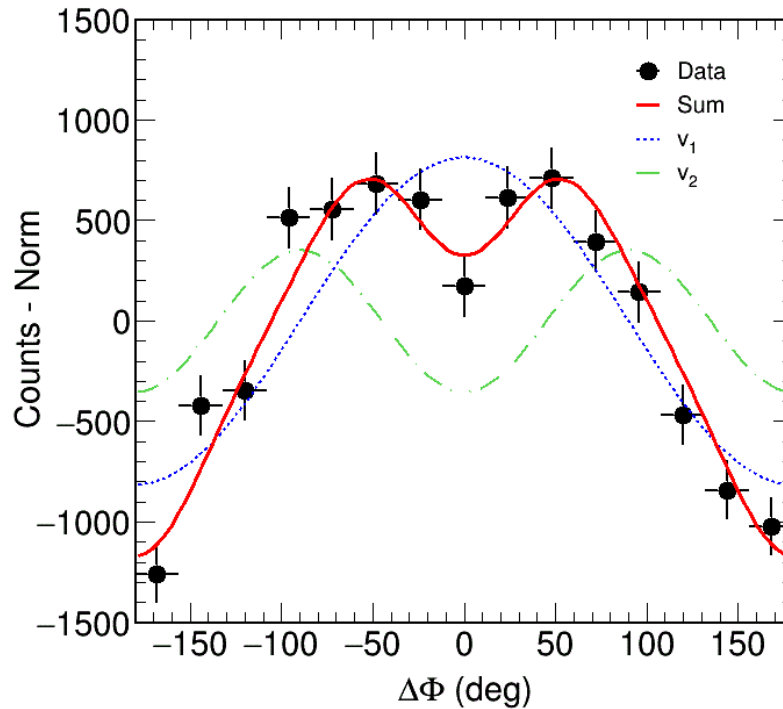
Figure 1.16: Azimuthal anisotropy of dileptons with $M_{ee} \leq 120\,\text{MeV/c}^2$ measured with HADES in Au+Au. The data are shifted down by the norm of the Fourier expansion. The solid red line shows the sum of this expansion, fitting the data well. The blue dotted line displays the directed flow component v_1 and the green dashed line represents the elliptic flow component v_2 [44].

In terms of elliptic flow one can distinguish between in-plane and out-of-plane elliptic flow. The former one gives positive values of v_2 while the latter one is negative. In Figure 1.17 the behavior of the elliptic flow for different collision energies is summarized.

In the low energy regime below $100A\,\text{MeV}$ deep inelastic scattering occurs and the ejectiles are emitted from the fast-spinning compound nucleus that is formed during the collision. This leads
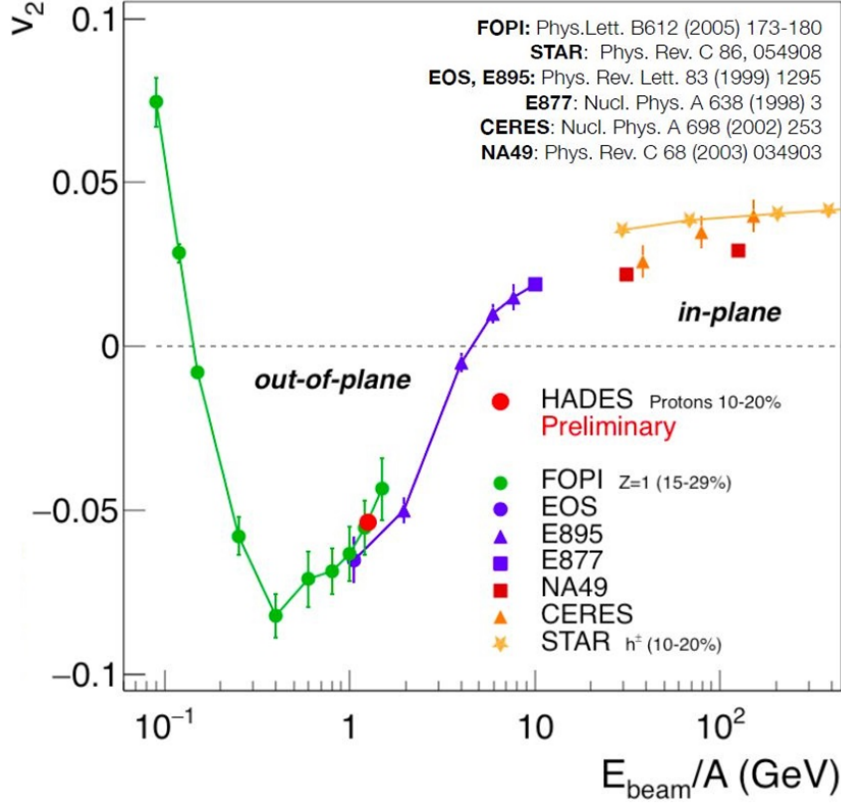
Figure 1.17: The behavior of elliptic flow of protons for different collision energies. The HADES data point is indicated as red circle.

to an enhanced emission of particles in the direction of the reaction plane due to the angular momentum transferred by the projectile nuclei, which corresponds to positive values of elliptic flow. Close to 100A MeV the elliptic flow component vanishes, which can be explained by the rotation responsible for the in-plane flow at low beam energies is not established due to the heating and the compression of the nuclear matter at higher energies. Thus the elliptic flow transitions to out-of-plane flow at collision energies between $100 - 1500$A MeV, leading to negative values of v_2. This out-of-plane flow can be explained by the passing spectator nuclei shadowing the collision center. This shadowing effect reduces the mean free path of particles that are emitted into the reaction plane, which leads to a squeeze-out of ejectiles perpendicular to the reaction plane. The higher the beam energy the faster the colliding nuclei pass each other which reduces the shadowing effect. At the same time the initial spatial anisotropies translate into a pressure gradient that makes in-plane ejection of particles more favorable. The counterplay between those two effects lead to in-plane elliptic flow at relativistic and ultra-relativistic energies above 1500A MeV. The HADES Au+Au run from 2012 with a beam energy of 1.23A GeV is indicated with the red circle in Figure 1.17 and lies clearly in the negative regime of the elliptic flow. [45]

The left panel of Figure 1.18 shows the p_T-integrated elliptic flow as a function of dilepton mass, calculated with a hydrodynamic model for the expansion of the fireball at ultra-relativistic energies. The solid line describes the total elliptic flow of all dileptons, beside dileptons from post-freeze-out decays. The dashed line shows the elliptic flow of dileptons from the QGP and the dotted line represents the elliptic flow of dileptons from hadronic decays. In the same plot the elliptic flow of various hadrons is indicated. It is visible that the resulting elliptic flow carries

contributions from hadronic and quark matter stages. The elliptic flow of hadronic dileptons is large and agrees with the v_2 of hadrons at the same mass. At low masses the elliptic flow of all dileptons is dominated by this hadronic contribution. For high masses the v_2 of all dileptons decreases, because the flow anisotropies are not yet fully developed at the early stages of the collision evolution. [42]

The first analysis of dilepton elliptic flow was presented by the STAR collaboration from minimum bias Au+Au collisions at $\sqrt{s_{NN}} = 200\,\text{GeV}$ [80]. The mass dependent elliptic flow can be seen in the right panel of Figure 1.18. It has to be stressed, that this is the elliptic flow of the inclusive dilepton radiation, which consists of contributions from the cocktail and the excess radiation. A further discussion and comparison to theory calculations can be found in [35].
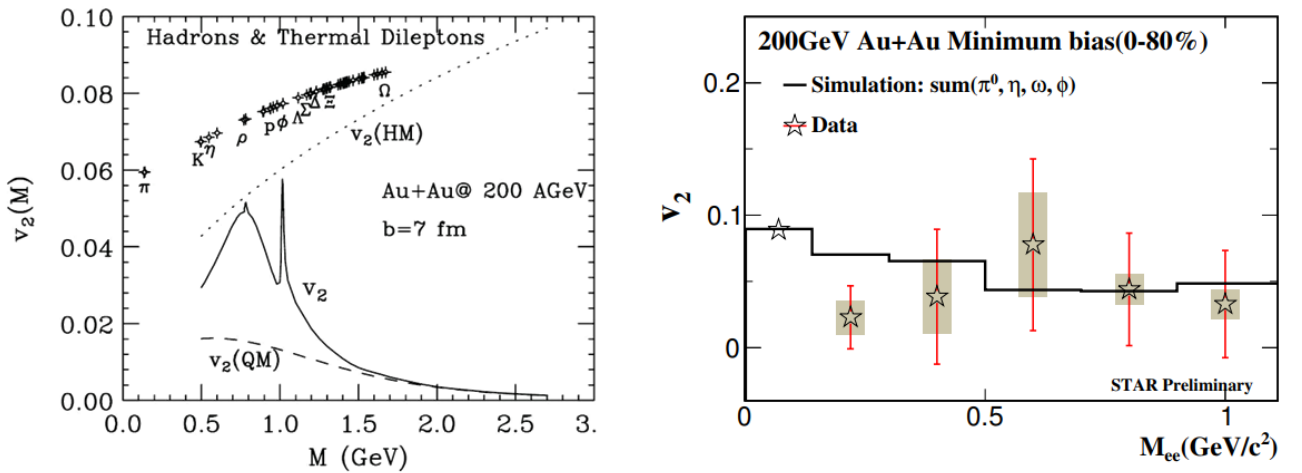
Figure 1.18: The left panel shows theory predictions for the behavior of dilepton v_2 at ultra-relativistic energies from a hydrodynamic model. [42]
In the right panel the first measurement of inclusive elliptic flow of dileptons by the STAR collaboration is presented. [80]

The azimuthal anisotropy of dilepton excess radiation has not been observed by any experiment thus far. At this point, HADES promises the ability to analyze the elliptic flow of the dilepton excess radiation, since the dilepton spectra at SIS18 energies are excess dominated. This offers the unique opportunity to further investigate the collective behavior of dileptons from the hot and dense phase of the fireball.

2 The High Acceptance Di-Electron Spectrometer (HADES)

HADES at SIS18 (GSI, Darmstadt) is a fixed target experiment, that investigates strongly interacting matter at highest net-baryon chemical potentials and moderate temperatures. The spectrometer provides a large acceptance between 18° and 85° in polar angle as well as a nearly full azimuthal coverage. Figure 2.1 shows a cross section through all components of the detector. The Ring Imaging CHerenkov detector (RICH), the Time of Flight (TOF) and RPC detector as well as the Pre-Shower detector are mainly used for particle identification, while the four planes of low-mass MDCs in combination with the superconducting toroidal magnet are used to determine the particle tracks and momenta. In order to reduce background from photon conversion in the detector material, all tracking detectors are designed as light as possible. The whole spectrometer has a hexagonal shape, consisting of six trapezoidal sectors. About 7 m behind the spectrometer the Forward Wall is placed, which is used to reconstruct the event plane and determine the centrality of the collision by measuring the spectator nucleons. For future runs, the Pre-Shower detector is replaced by an Electromagnetic CALorimeter (ECAL), that can measure π^0 and η mesons via their two photon decay.
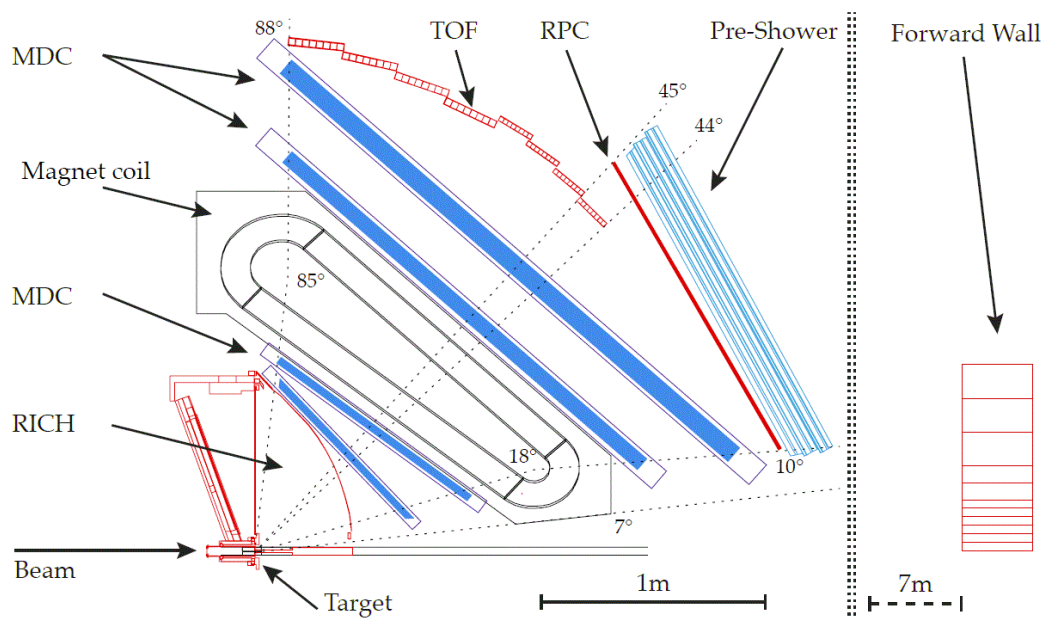
Figure 2.1: One of the six sectors of HADES [46].

All detectors are connected to the Data AcQuisition network (DAQ), that can handle event rates of 100 kHz (p + p) and 20 kHz (Au + Au), respectively as well as data rates up to 400 MBytes/s. In the following sections each part of the spectrometer will be described. [47]

2.1 The Target and Start-Veto System

Experiments with various solid fixed targets, such as KCl, Carbon, Niobium, Wolfram, Gold and Polyethylene have been performed at HADES, as well as some runs with a liquid hydrogen target. To reduce gamma conversion and multiple scattering in the target, the solid targets are segmented into several slices. In this thesis data from the Au+Au run at 1.23A GeV in 2012 will be analyzed. The gold target consists of 15 foils, each 25 μm thick, that are glued to a Kapton® polyimide film and mounted in a carbon fiber support frame.
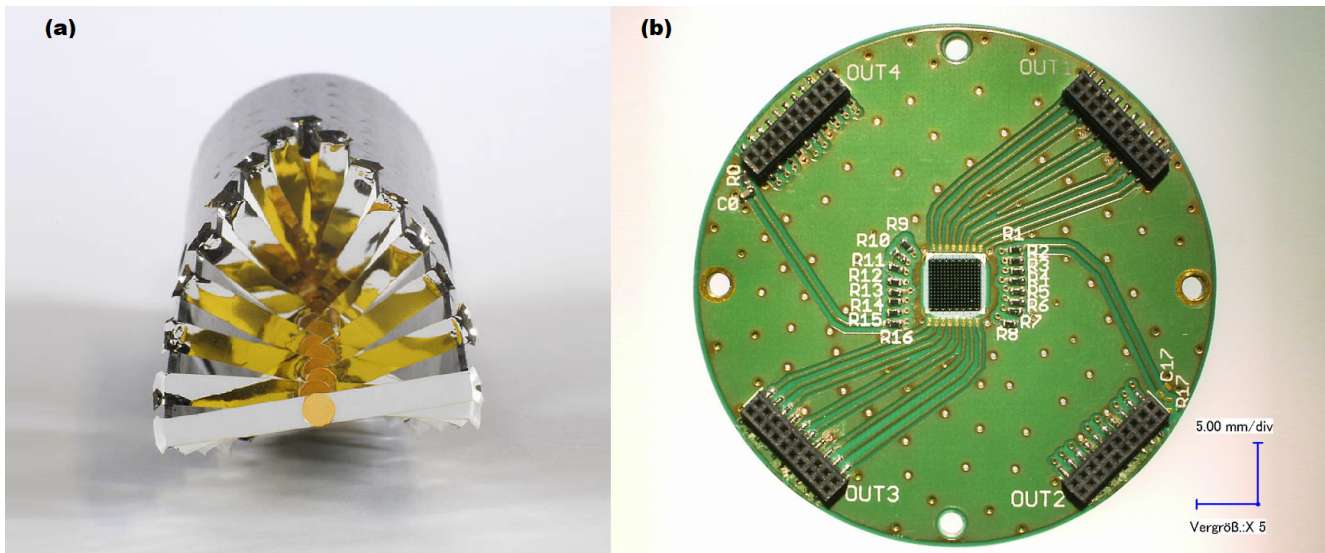
Figure 2.2: (a) The segmented Gold target used in the HADES Au+Au run in 2012. It consists of 15 25 μm thick gold foils, mounted in a carbon fiber support frame. (Photograph by Gabi Otto, GSI)
(b) The diamond based Start detector for the future Ag+Ag run in 2019 [48]

A diamond based Start detector is placed 2 cm in front of the target. It measures the T_0 start signal needed for the time-of-flight measurements, thus it requires a precision better than 50 ps. 70 cm behind the target there is a second diamond based Veto detector, to discard beam particles that did not interact with the target. Furthermore, the two detectors are used to monitor the beam. Since the start-veto system is mounted in the beam-line it needs to be radiation hard, which is why diamond is chosen as a material. The start detector is made of a mono-crystalline single crystal Chemical Vapor Deposition (scCVD) of 75 μm thickness, to achieve a very low interaction probability of the beam ions with the detector of 0.36%. The Veto detector consists of a polycrystalline diamond material with a thickness of 100 μm. Both detectors are metalized to provide contact between the diamond and the electrodes. Besides the radiation hardness, diamond detectors offer further advantages, such as a high rate capability (signal base-width of about 2 ns), very high drift velocities of electrons and holes of 1200 cm^2/Vs leading to a fast signal collection time, a wide band gap of 5.5 eV resulting in low noise and a high thermal conductivity of 1000 − 2000 W/mK that allows to operate the detectors at room temperature. Charged particles traversing the detector produce free electron-hole pairs in the diamond material that drift to the electrodes. The voltage at the electrodes is proportional to the deposited energy. For obtaining the position information needed for beam monitoring, the metalization on the diamond is segmented into 16 strips in x and y direction, which can be seen in the right panel of Figure 2.2. [49–51]

2.2 The Ring Imaging CHerenkov Detector (RICH)

To discriminate leptons from hadrons, the RICH detector is used. It takes advantage of the fact, that at SIS18 energies the ratio β of the particle velocity to the speed of light is close to one for electrons and positrons but only about 0.95 for hadrons. Thus the Cherenkov radiation, that is emitted when a charged particle traverses a dielectric medium at higher velocity than the phase velocity of light in this medium, can be used for lepton identification. The medium in the RICH detector is chosen in such a way, that only electrons and positrons can exceed the speed of light in this medium. In case of HADES it is C_4F_{10} gas. The Cherenkov light is emitted in a cone and reflected by a spherical mirror, producing rings that are focused on the photon detection plane. The photon detection system consists of six trapezoidal multi-wire proportional chambers (MWPCs) operated with CH_4 gas, each of which has 4712 CsI photo cathode pads. The both gas volumes are separated by a CaF_2 window, that is transparent for UV-light. The left side of Figure 2.3 shows a schematic view of the RICH detector at HADES. On the right side the photon hit distribution in the RICH pad plane can be seen for typical rings.
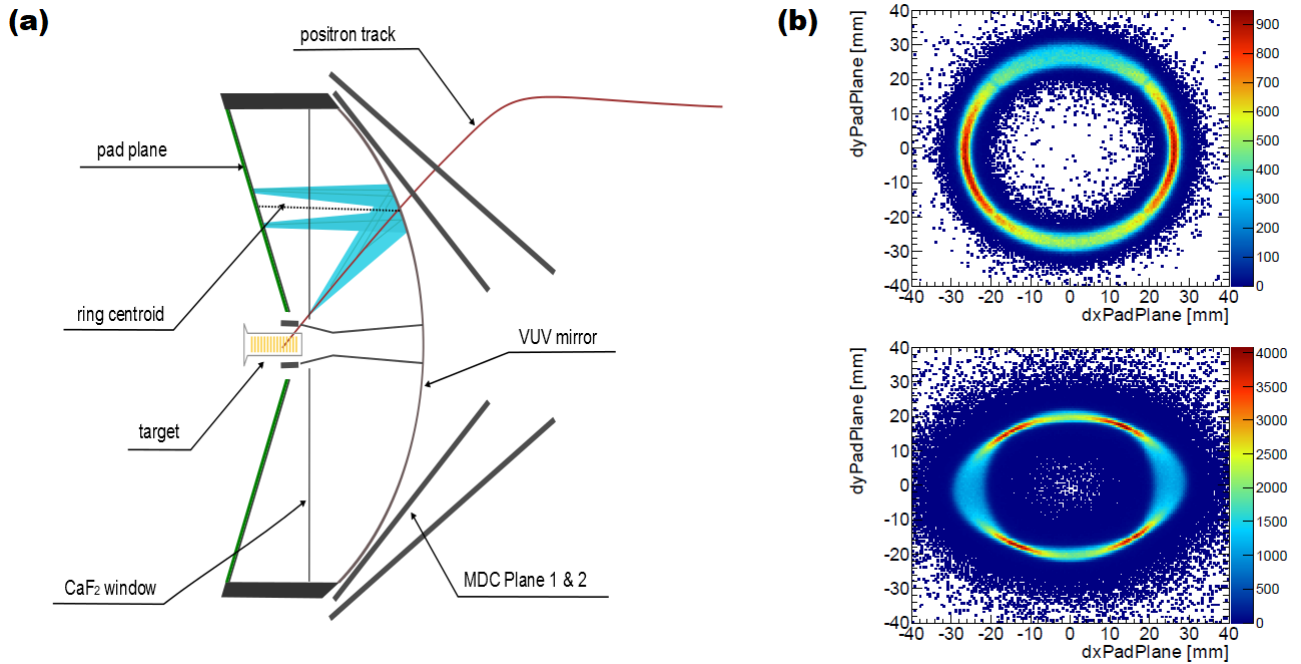
Figure 2.3: (a) A schematic view of the RICH detector at HADES. [52]
(b) Photon hit distributions of rings generated with GEANT. The upper ring is located at a polar angle of $\Theta \approx 31°$. The lower ring shows a deformation typical for higher polar angles. It is located at $\Theta \approx 77°$. [53]

The RICH detector is the innermost detector of hades, located in an essentially field free region, thus the particle tracks are straight lines. It is designed to identify relativistic $e^{\pm}$ with momenta $0.1\,\text{GeV/c} \leq p \leq 1.5\,\text{GeV/c}$. To minimize external pair conversion and multiple scattering the detector is build as lightweight as possible. For the upcoming beamtime in 2019 the RICH detector is upgraded with a new photon detection system using multi anode photomultiplier tubes (MAPMTs) to detect the Cherenkov photons. [54–56]

2.3 The HADES Tracking System

The HADES tracking system consists of four planes of Multiwire Drift Chambers (MDCs), two in front and two behind the field region of the superconducting toroidal magnet. For historical reasons the MDCs are also called Mini Drift Chambers. The overall layout of the tracking system can be seen in the left panel of Figure 2.5.

2.3.1 Magnet

The magnet is designed in a way to provide a nearly field free region around the target, to allow the operation of the RICH detector. Thus the six superconducting NbTi coils produce a toroidal field with a gradient from 3.6 T at the coil surface down to 0.8 T in the center. Furthermore it has a large acceptance for momenta in the range of $0.1\,\text{GeV/c} \leq p \leq 1.5\,\text{GeV/c}$ and polar angles $\Theta = 18°$ - $85°$ as well as nearly full azimuthal coverage. The plot in the right part of Figure 2.4 shows the field map of the magnet at $\Phi = 0°$, i.e. midplane between the coils. Due to the shape of the coils, the field shows a strong inhomogeneity as a function of polar and azimuthal angles. Indicated in the same picture are the four planes of MDCs and the trajectory of a negatively charged particle.
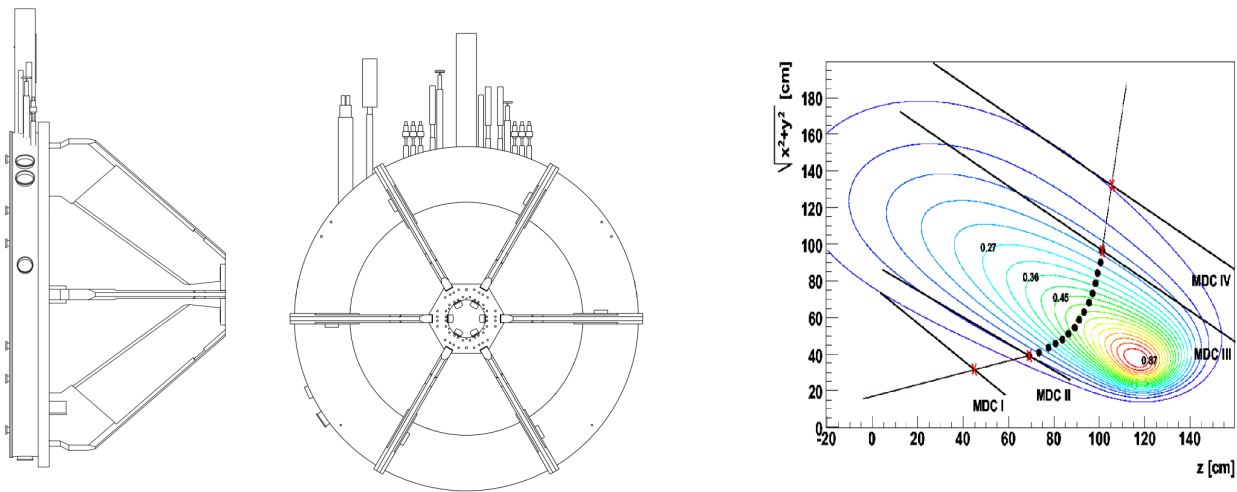
Figure 2.4: Technical drawing of the superconducting magnet that is part of the tracking system. The picture on the left shows a side view of the magnet and in the middle it is shown from the back. On the right the field lines of the B-field as a function of z (along the beam axis) and r (perpendicular to the beam axis) are plotted and the trajectory of a negatively charged particle is indicated. [55]

A charged particle traversing the field of the magnet experiences a transverse kick, altering its trajectory. This deflection allows to calculate the momentum of the particle. For electrons the momentum resolution is of the order of $\sigma_p/p = 1.5$ - 2%.

2.3.2 Multiwire Drift Chambers

Following the overall detector geometry of the spectrometer the MDCs consist of six trapezoidal sectors. The size of the planes increases towards the outermost plane, to provide a constant polar angle coverage of 18° - 85°. By measuring the position of a charged particle in the four planes its track can be reconstructed and in combination with the deflection in the magnetic field its momentum can be calculated. In addition a particle can be identified by its energy loss in the MDC chambers. A chamber module consists of about 1100 drift cells, resulting in a total of 27.000 cells. Each chamber is composed of 13 layers of wires that form six drift cell layers, each oriented in a different angle ($\pm 0°$, $\pm 20°$, $\pm 40°$), which favors maximum spatial resolution in polar direction aligned with the momentum kick of the magnet. The right panel of Figure 2.5 shows a schematic picture of a drift chamber. To provide a constant granularity the sizes of the drift cells increase from $5 \times 5\,\mathrm{mm}^2$ (plane I) to $14 \times 10\mathrm{mm}^2$ (plane IV).
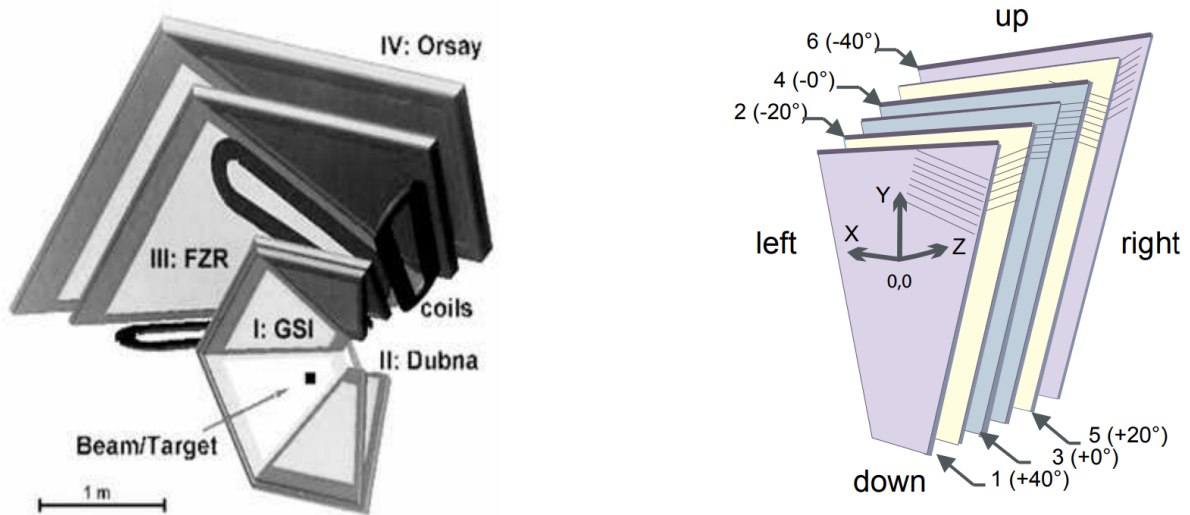
Figure 2.5: On the left the overall layout of the HADES tracking system can be seen. Two planes of MDCs are placed in front and behind the magnetic field. The right panel shows the six sense and field wire layers that form a drift cell. [55]

The drift chambers of the innermost plane (plane I) are filled with Ar/CO_2 (70/30) and all the other chambers are filled with Ar/C_4H_{10} (84/16) gas mixture. A charged particle traversing the detector ionizes the gas inside the chambers and the electrons and positively charged gas ions drift to the sense and field wires. Close to the wires the electric field is high and the electrons that are accelerated towards the sense wires create an avalanche that can be measured. The spatial resolution of the cells lies between 60 - 100 μm in polar angle direction and 120 - 200 μm in azimuthal angle direction.

The energy loss in the MDCs can be measured indirectly from the width of the drift time signal. Since the MDCs are not equipped with ADCs a direct measurement of the deposited charge is not possible. For minimum ionizing particles a dE/dx resolution of around 7 % can be achieved, while stronger ionizing particles show an energy loss resolution of about 4 %.

2.4 The Time of Flight Measurement

To calculate the velocity of a particle, the distance it covers is divided by its time-of-flight. For the reconstruction of the time-of-flight a good measurement of the start and stop time of the particle is required. The former one is performed by the Start detector described in Section 2.1. The start time estimation reaches a time resolution of about 50 ps. For the stop time measurement a combination of a Time-of-Flight Wall (TOF) and a Resistive Plate Chamber (RPC) is placed behind the tracking system.

2.4.1 Resistive Plate Chamber (RPC)

The RPC detector covers the forward polar angles between 18° and 45°. It replaces the low-granularity TOFino detector and is capable of handling collisions with high particle multiplicities. Following the overall detector geometry the total area of 8 m^2 of the RPC is divided into six trapezoidal sectors. Each sector is subdivided into three columns that consist of 31 strip-like RPC cells. In total the detector has two partially overlapping layers of cells to increase acceptance and efficiency and reduce dead regions. A RPC cell consists of three aluminum electrodes and two glass electrodes of 1.85 mm and 2 mm thickness respectively. The different electrodes are hereby placed in an alternating order. The four gaps between the electrodes are fixed by PEEK[1] monofilaments of 270 μm diameter, which are placed every 5 to 10 cm along the cell. Each cell is mounted inside an individual shielding tube and filled with a gas mixture of $C_2H_2F_4/SF_6$ (90/10). To ensure a constant gap size the shielding tube also contains a PVC pressure plate, that is compressed down by three springs. The complete setup is shown in Figure 2.6 on the left and the right part shows a photograph of a single cell.
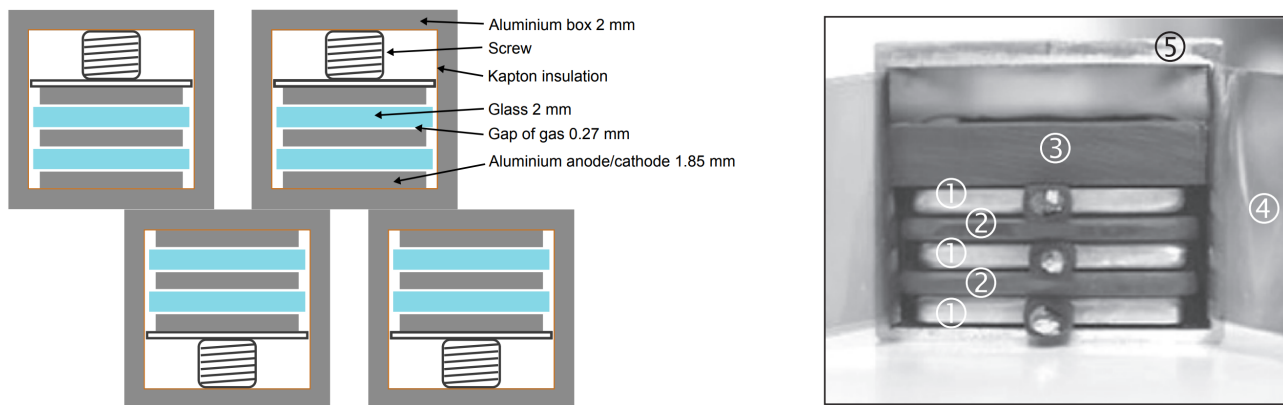
Figure 2.6: On the left a cross section through the HADES RPC cells shows the main components and the overall structure of the detector [57]. On the right a photography of one cell is shown: 1 – aluminium electrodes, 2 – glass electrodes, 3 – PVC pressure plate, 4 – kapton insulation, 5 – aluminum shielding tube [58].

The RPC detector operates at a nominal voltage of 5.6 kV. A charged particle that traverses the cell ionizes the gas and due to the high electric fields the free electrons are accelerated towards the anode where they create an avalanche. An advantage of the RPC is, that the amplification of

---

[1] Polyetheretherketone

primary electrons is strongly localized, since the high resistivity of the glass electrodes prevents the discharge from propagating through the gas. Therefore blind spots after a hit are very small. In addition the individual shielding of each tube leads to an excellent multi-hit capability. The chosen gas mixture exhibits a relaxation time for blind spots in the order of ms. Hence the RPC setup allows for very high multiplicities with particle rates up to $1 \, \text{kHz/cm}^2$ and an average double hit probability below 10 % (in Au+Au at 1.23 A GeV). The detection efficiency in this case is 95%. Furthermore a good time resolution of $\sigma_t \approx 70 \, \text{ps}$ and longitudinal position resolution of 8 mm is achieved. [57–61]

2.4.2 Time of Flight Wall (TOF)

The TOF detector covers the outer polar angles between 44° and 88°. According to the detector geometry the TOF wall has six sectors and each of them consists of eight modules. Each module again comprises a set of eight scintillator rods amounting to a total of 384 rods which are enclosed in a carbon fiber case. The length of the rods varies from 1 m for the smaller polar angles to 2 m for the larger polar angles. Their cross section is $20 \times 20 \, \text{mm}^2$ for the inner half of the rods and $30 \times 30 \, \text{mm}^2$ for the outer 192 rods. These sizes have been chosen to match the TOF granularity to the charged particle multiplicity angular distribution in order to keep the double hit probability below 10 % in the whole detector. Each rod is made of BC408 plastic scintillator material and glued to a light guide in an angle of 65° to 67°. The light guide has an initial square cross section to match the rod and it progressively changes to a circular cross section at the end where it is coupled to the photomultiplier (PMT).

A charged particle that travels through the scintillator material generates scintillation light. The emitted photons travel to the PMTs on the left and right side of each scintillator. From the different arrival times the x-position of the particle can be estimated with a resolution of $\sigma_x \approx 25 \, \text{mm}$ and $\sigma_x \approx 27 \, \text{mm}$, respectively for the inner ($20 \times 20 \, \text{mm}^2$) and outer ($30 \times 30 \, \text{mm}^2$) rods. The y-position of the particle can be determined with a resolution in the order of 2 to 3 cm corresponding to the dimension of the rods. The resolution of the time-of-flight is given by $\sigma_t = 100 - 150 \, \text{ps}$. In comparison the peak width of the TOF is almost double of the RPC due to the lower resolution of the TOF. Furthermore the deposited energy ΔE can be measured. The equation below shows how time of flight (tof), the hit position along the rod (x) and the deposited energy ΔE are calculated.

$$
\begin{aligned}
\text{tof} \quad &= \quad \frac{1}{2}\left(t_{\text{right}} + t_{\text{left}} - \frac{L}{V_g} \right) \\
x \quad &= \quad \frac{1}{2}\left(t_{\text{right}} - t_{\text{left}} \right) V_g \\
\Delta E \quad &= \quad k \sqrt{a_{\text{right}} \cdot a_{\text{left}} \cdot e^{L/\lambda_{\text{at}}}}
\end{aligned}
\tag{2.1}
$$

V_g denotes hereby the group velocity of the light inside the scintillator rod, λ_{at} is its attenuation length, L the length of the rod and k a constant. t_{left} and t_{right} are the calibrated time intervals between the occurrence of the reaction and the arrival of the two light pulses at each rod end, and a_{left} and a_{right} are the corresponding light signal amplitudes.

The TOF wall can be also used for a fast determination of the charged particle multiplicity which allows to select certain reaction classes such as impact parameter selection, i.e. centrality characterization or trigger. [55]

2.5 The Pre-Shower detector

The Pre-Shower detector is mounted behind the RPC at forward polar angles between 18° and 45°. It provides additional information for lepton identification which is important due to the higher track density in the region of smaller polar angles. Each of the six sectors is composed of three trapezoidal wire chambers (pre-chamber, post1-chamber, post2-chamber) separated by two lead converters of $d_1 = 2\chi_0$ and $d_2 = 1.5\chi_0$ thickness, with the radiation length of lead $\chi_0 = 0.56\,\text{cm}$. The complete setup can be seen in Figure 2.7.
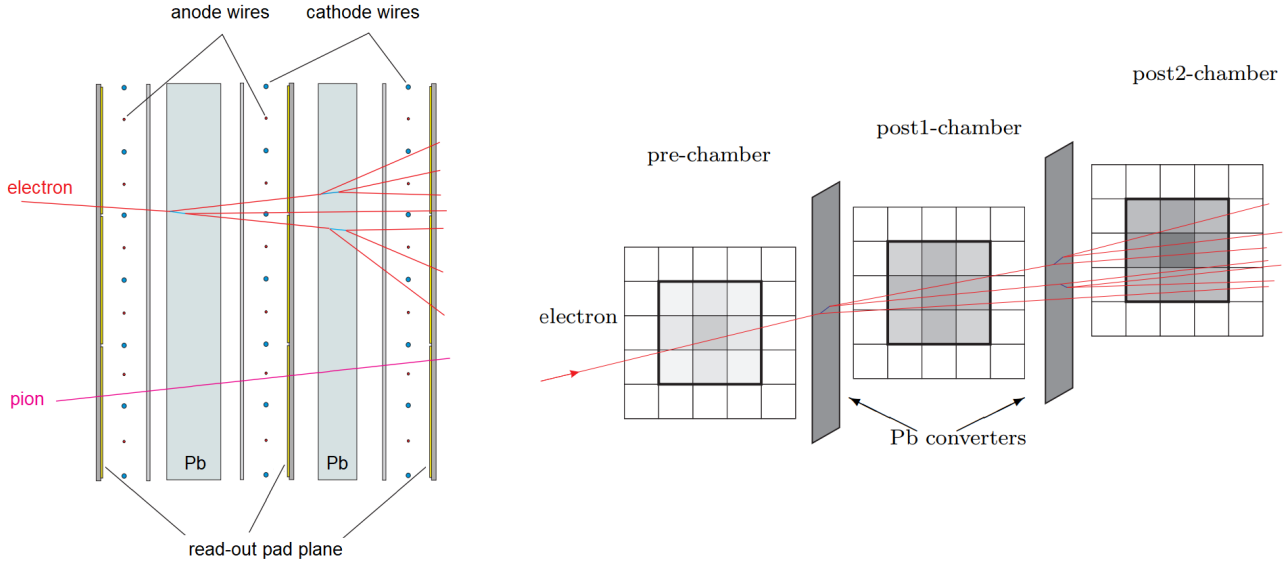
Figure 2.7: The left panel shows the structure of the Pre-Shower detector. An electromagnetic shower induced by a lepton is much more pronounced than a hadronic shower. On the right the principle of the shower algorithm is indicated. [55]

The drift chambers consist of a wire plane of equally spaced cathode and anode wires sandwiched between two flat cathode planes. One of the cathode planes also acts as read-out plane with 942 individual pads. To provide a constant granularity the pad size increases with the polar angle. The chambers are filled with a gas mixture of $\text{Ar}/\text{c}_4\text{H}_{10}/\text{C}_7\text{H}_{16}$ (33/65/2) and operated in the limited self-quenching streamer mode (SQS). Because of the charge saturation effect that limits the chamber gain in this mode, the integrated charge depends weakly on the specific particle energy loss but is rather proportional to the number of particles traversing the chamber. Thus fake contributions from non-minimum ionizing particles with larger energy losses are reduced.

To identify a particle traversing the detector, the charge in all three chambers ($Q_{\text{pre}}, Q_{\text{post1}}, Q_{\text{post2}}$) is measured. In order to obtain the complete charge of a shower, the deposited charge in 3×3 pads centered around a local maximum is integrated. This can be seen in Figure 2.7 on the right. Subsequently the charge difference between the first chamber in front of the two lead converters and the sum of the two following chambers behind the converters is calculated:

$$Q_{\text{sig}} = \left(Q_{\text{post1}} + Q_{\text{post2}}\right) - Q_{\text{pre}} \qquad (2.2)$$

This charge difference is expected to be larger for electrons and positrons, hence it can be used to distinguish between leptons and hadrons. In conclusion the combination of the information

from the Pre-Shower detector with the reconstructed tracks in the MDCs and the RICH rings provides a clean electron identification. For the future experiments at FAIR Phase-0 the Pre-Shower detector is replaced by an Electromagnetic Calorimeter (ECAL). [55]

2.6 The Forward Hodoscope Wall

In order to measure the spectators of a collision that are crucial to reconstruct the reaction plane and estimate the centrality of an event a Forward Hodoscope Wall (FW) detector is installed 7 m downstream of the target. It covers polar angles between $0.3° < \Theta < 7.3°$ which extends the acceptance of the detector system in the lower polar angles. The structure of the Forward Wall can be seen in Figure 2.8. It consists of 288 scintillator modules that are read out by photomultiplier tubes. The size of the elements varies to match the increasing spectator multiplicity towards the center. The innermost part of the detector is made of 140 $4 \times 4\,\mathrm{cm}^2$ cells. The 64 elements in the middle measure $8 \times 8\,\mathrm{cm}^2$ and the outermost part of the Forward Wall has 84 $16 \times 16\,\mathrm{cm}^2$ sized cells. In the center a $8 \times 8\,\mathrm{cm}^2$ hole is left empty to allow the primary beam to pass through.
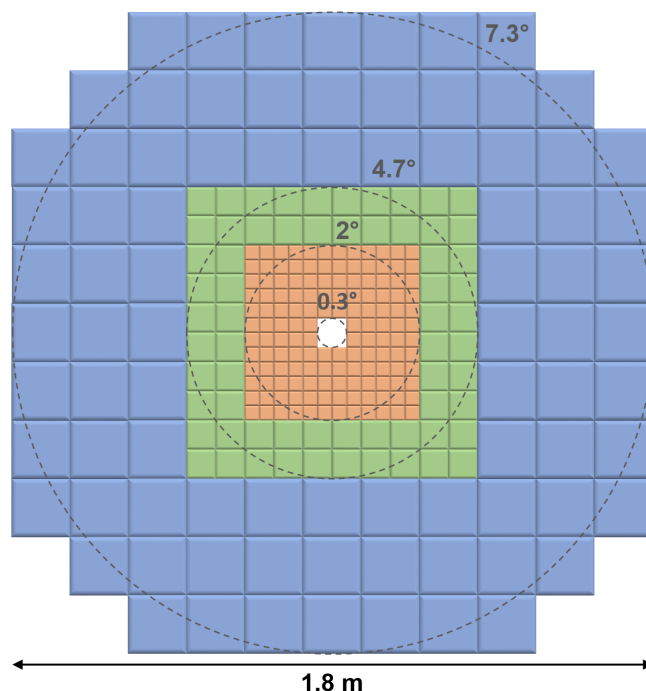
Figure 2.8: The Forward Hodoscope Wall consists of 288 scintillator modules in three different sizes and covers polar angles between 0.3° and 7.3°.

The Forward Wall provides information about the position of a hit (center coordinate of the cell) and together with the start detector also a time of flight measurement can be taken. Furthermore the number of photons produced in the scintillator material is proportional to the particle charge squared, thus the charge of an incoming particle can also be measured. The signal amplitude coheres with the energy loss of the particle or fragment in the cell and can be used to identify it. Since there is no magnetic field present a direct measurement of the momentum is impossible. The estimated resolution in the Au+Au beamtime was $\sigma_{\mathrm{tof}} = 400 - 500\,\mathrm{ps}$ resulting in a momentum resolution of 11 % for protons. [62]

2.7 The Data Acquisition Network (DAQ)

The HADES Data Acquisition Network has to handle high multiplicities and reaction rates as they occur in Au+Au collisions. Since dilepton pairs are rare probes, purely hadronic events are common. To prevent overloading of the DAQ and the frontend electronics on the one hand and to be able to acquire the needed dilepton statistics on the other hand an on-line data reduction and event filtering is performed. A two-staged trigger system[2] is used for the filtering. The Central Trigger Unit (CTU) creates and transmits the triggers to the individual subsystems. The level one (LVL1) trigger decision is based on external input sources such as charged particle multiplicity or calibrating triggers and operates at 20 kHz trigger rate in Au+Au. This corresponds to data rates of up to 400 MByte/s. Real time pattern recognition provides a second level (LVL2) trigger decision, selecting events by searching for lepton pairs. The readout board then only sends those events to the event builder that satisfy the trigger criteria. Thus only those events are build, i.e. the information from the different asynchronous data sources are combined and written to mass storage. Because of the delay between trigger level one and two of the order of 5 to 10 events, the readout board has to have buffer storage to hold the data for this time. The two-level trigger system of the HADES data acquisition network is summarized in Figure 2.9. The events recorded after the second trigger level show a ten times higher lepton yield than the unbiased LVL1 events. They are selected with 90 % efficiency. [63]
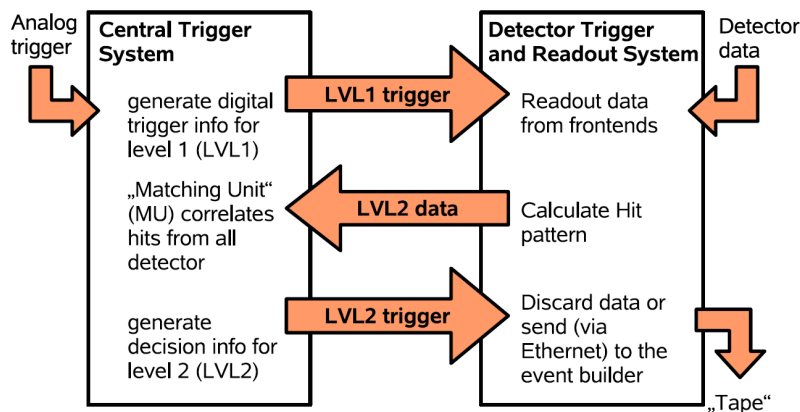
Figure 2.9: Schematic view of the two-level trigger system of the HADES data acquisition network. The analog triggers from the different sources are processed by the central trigger system which produces the digital LVL1 trigger based on this information. The trigger signal is transported to individual detector trigger systems. The LVL2 trigger decision is based on the hit patterns of the detectors. Finally the data is discarded or send to the event builder based on the LVL2 trigger decision. [63]

To transport the high data rates a custom FPGA based network, called TrbNet, with optical links is used inside the detector. A commercial Gigabit Ethernet infrastructure (GbE) then transports the digitized detector data to the server farm. The TrbNet provides three virtual channels, staggered by priority. Channel number one (with highest priority) is used for the distribution of the LVL1 trigger signal from the CTU to all data collecting front-ends. After the transmission the channel is blocked until all endpoints have returned a busy-release packet. The

---

[2] In the Au+Au beamtime in 2012 only the level one trigger was used.

round-trip time of the trigger and its acknowledgment defines the achievable trigger rates. Subsequently, the CTU requests the sending of the data (readout request) via the second channel. This data is transferred via GbE to the event builder where it is prepared for permanent storage as HADES list-mode data (HLD). The third channel is used for monitoring and slow control of each individual front-end board. [64]

3 Data Analysis Strategy

In eleven runs (test runs excluded) between 2002 and 2014 HADES collected data from various experiments at beam energies of $1 - 3.5\,\text{GeV}$. The size of the collision system ranged from elementary p+p collisions over light (C+C) and medium (Ar+KCl) sized collision systems to the large Au+Au system. In the last two runs performed in 2014 also pion induced reactions were investigated.

In this thesis data from the Au+Au run at $1.23\text{A}\,\text{GeV}$[1] in 2012 will be analyzed. In the five-week beamtime (overall 557 hours) with beam intensities between $1.2 - 1.5 \cdot 10^6\,\text{ions/s}$ a total of 7.3 billion events was measured and stored in $138\,\text{TByte}$ of data. The amount of raw data taken in the different HADES runs can be seen in the left part of Figure 3.1. The right part compares the interaction rates of different facilities. Of all currently operating facilities HADES has the highest interaction rate. [65, 66]
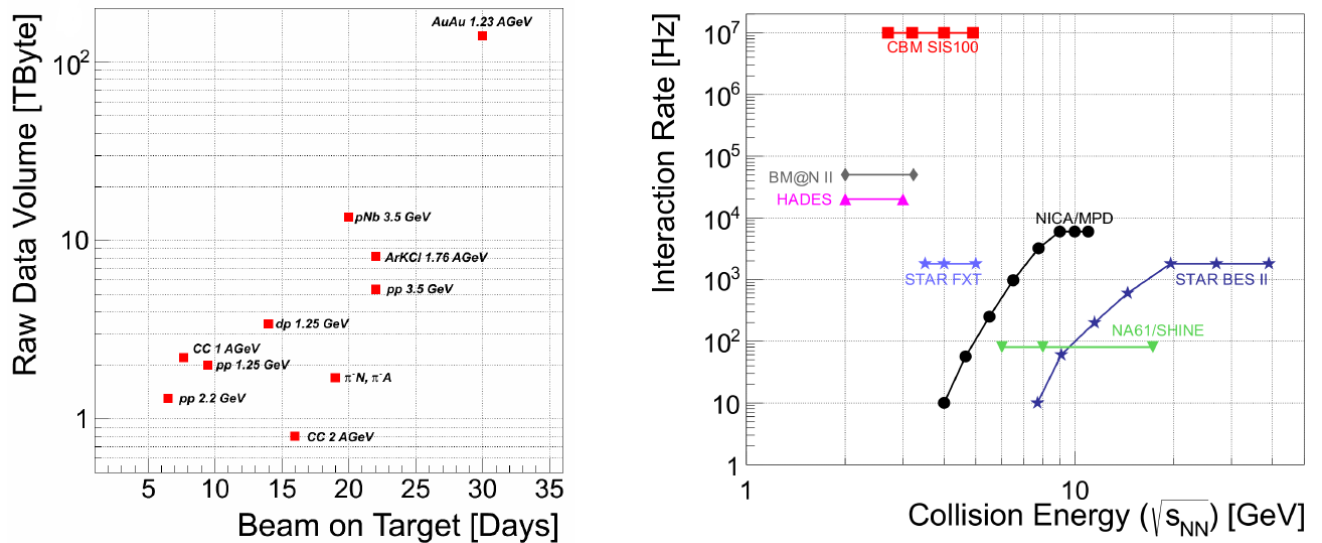
Figure 3.1: On the left the total amount of raw data collected during the different HADES runs is shown. The right panel compares the interaction rates of HADES to different existing and future experiments.

The HLD files written by the HADES data acquisition network contain the raw data from the readout electronics of the different detectors. To obtain the Data Summary Tape (DST) files, which contain additional physical quantities for characterization of the reconstructed particles, the HLD files have to undergo several steps. After unpacking the compressed data sent by the read-out electronics, it has to be calibrated, which means to convert the values from the detectors into physical quantities. Subsequently the single detector signals have to be combined into full tracks. For the analysis of the DST files the Hades sYstem for Data Reduction and

---

[1] A beam energy of $E_{\text{beam}} = 1.23\text{A}\,\text{GeV}$ corresponds to a center-of-mass energy of $\sqrt{s_{\text{NN}}} = 2.42\,\text{GeV}$ and a center-of-mass rapidity of $y_{\text{mid}} = 0.74$.

Analysis (HYDRA) is used. HYDRA is based on the software ROOT developed at CERN. ROOT is an object-oriented toolkit for data analysis, storage and visualization which provides most of the functionalities needed to deal with big data processing. Therefore it is widely used in High Energy Physics and other disciplines. It is mainly written in C++ but integrated with other languages such as Python and R. ROOT provides a framework with many libraries that allow processing a large amount of data, perform calculations, fit functions to the data, and visualize it, as well as store and access the data. HYDRA extends the functionalities of ROOT with detector specific tasks and functions for track reconstruction and data analysis specific to HADES. [67]

In this chapter the particle reconstruction procedure in the HADES Au+Au run 2012 is described. Furthermore the event selection criteria for this analysis will be discussed, including event characteristics like sector quality, centrality and event plane reconstruction. This will be followed by a section about the single lepton identification that uses a multivariate analysis. After the single electrons and protons are identified, they have to be combined into dilepton pairs, which will be subject of the subsequent section. The focus lies hereby on the handling of the combinatorial background via the like-sign geometric mean and event mixing approach. Finally different methods for the reconstruction of flow will be presented.

3.1 Particle Reconstruction

For the particle reconstruction the information of the different detectors has to be combined. The trajectory of the particle is reconstructed from hits in the MDC. By matching the straight-line segments from the two chambers in front of the magnet with the two chambers behind the magnet, the momentum of the particle can be calculated. To obtain the full track of the particle, the information from the MDC has to be matched with a hit in one of the META detectors. Furthermore the time-of-flight of the particle has to be reconstructed to get its velocity. For leptons also the information of the RICH detector is needed and the hits in the RICH pad plane are used to reconstruct a ring, that is also matched with the track of the lepton.
The output of all those analysis steps has the form of a tree data structure and is stored in the DST files. Those files can tan later on be used to further select particular events based on the respective physics case. In the following sections each step of the particle reconstruction is described.

3.1.1 Track Reconstruction

As a first step of the reconstruction of the particle trajectory, the hit position in each MDC plane has to be found. To obtain the track candidates, all fired drift cells are projected onto a common plane with a reference point within the vertex range. The wires from each layer of the MDC are summed up and maxima occur in case of correlated wire position. The left side of Figure 3.2 shows the result of this projection, which is a two dimensional histogram with a local maximum, called wire cluster, where the particle crosses the drift chamber. One of the challenges is the high particle multiplicity in Au+Au collisions which leads to a large number of possible tracks. Fake contributions from close clusters are removed by setting a dynamic threshold of fired wires, depending on the total amount of fired wires in this event. Assuming straight lines, the remaining clusters are combined with respect to the event vertex, using a χ^2-minimization technique,
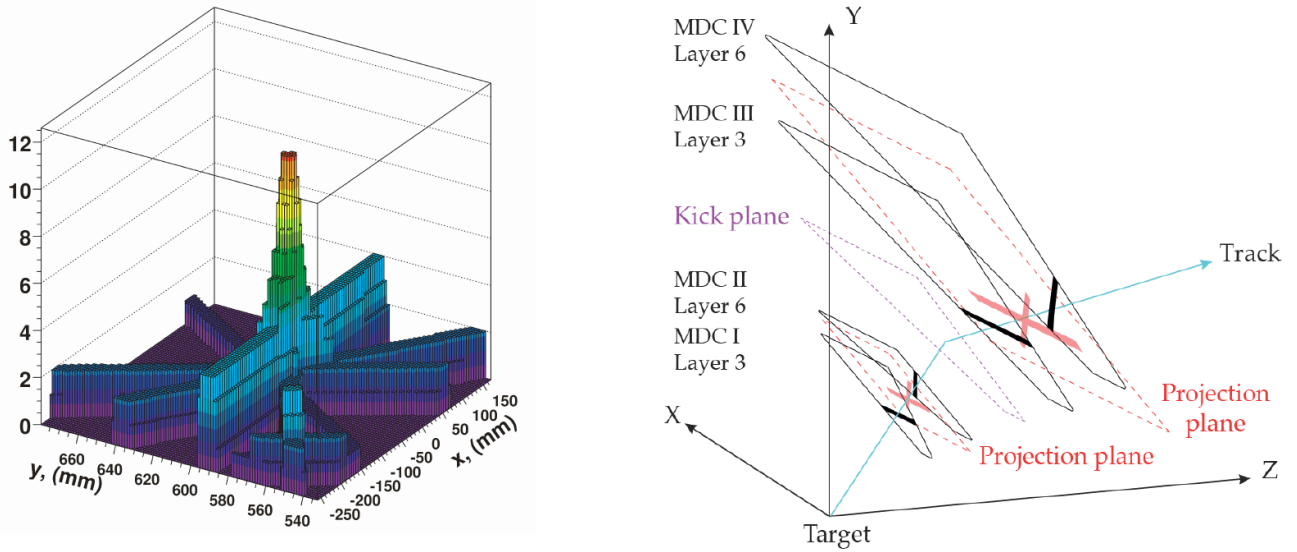
Figure 3.2: On the left the cluster finding procedure in the MDC chambers is illustrated. The projection of the fired drift cells into a plane perpendicular to the particle tracks shows a peak at the position where the particle crossed the wires. [53]
On the right the matching of an inner and outer segment using the kick plane method is shown. [55]

i.e. the straight line with the smallest deviation from the signals is chosen. Additionally the drift times and fit errors are included and at least nine layers are required to contribute to the track segment, to further improve the tracking efficiency. The result is a reconstructed inner track segment.

The outer track segment is reconstructed in a similar way, but the reference point for the projection plane now lies on the so called kick-plane. The assumption is, that the deflection in the magnetic field can be described by a momentum kick in a certain plane. The intersection of the reconstructed inner segment and this kick plane is then used as vertex for the cluster finding of the outer MDC chambers. The search for clusters is hereby restricted to the physical region of possible particle deflections. The matching between the inner segment and the possible outer segments is done using a Runge-Kutta method and again the one with the smallest χ^2 is preferred. All matched inner and outer MDC segments are then stored as MDC track candidates. The reconstruction of a MDC track is illustrated in Figure 3.2 on the right, where also the kick plane and the two projection planes for inner and outer track segment can be seen. Leptons exhibit a tracking efficiency of around 90 % for momenta p > 0.1 GeV/c. For smaller momenta the efficiency drops, since the tracks show a larger curvature, thus a higher deviation from the straight line assumption. [55]

3.1.2 Momentum Reconstruction

The momentum of a charged particle can be determined by its deflection angle in the magnetic field. The simplest approach is the kick-plane method, presented in the section about the reconstruction of the track candidates in the MDC. It assumes the deflection to be a single mo-

mentum kick in a two-dimensional, almost flat virtual surface that coincides roughly with the center plane of the magnet and is referred to as kick plane. The momentum kick is the change of the momentum of a particle from the inner to the outer segment and can be written as:

$$|\Delta\vec{p}| = |\vec{p}_{in} - \vec{p}_{out}| = 2p\sin(\Delta\theta_k/2), \qquad (3.1)$$

where $\vec{p}_{in}$ and $\vec{p}_{out}$ are the incoming and outgoing three-momentum vectors of magnitude p and $\Delta\theta_k$ denotes the deflection angle. The small-angle approximation of the sine function $(\sin\alpha \approx \alpha)$ holds for large momenta, i.e. small deflections, leading to:

$$|\Delta\vec{p}| \approx p\Delta\theta_k \qquad (3.2)$$

Using the the integral of the Lorentz force along the particle trajectory through the magnet to describe the deflection angle and truncate its Taylor expansion in $\sin(\Delta\theta_k/2)$ in second order, one obtains:

$$|\Delta\vec{p}| = \frac{1}{2}\frac{p_{k0}}{2\sin(\Delta\theta_k/2)} + p_{k1} + 2p_{k2}\sin(\Delta\theta_k/2) \qquad (3.3)$$

The parameter p_{ki}, $i = 0, 1, 2$ denotes the i-th order momentum kick and depends only on the entry and exit points of the particle track in the magnetic field. Those momentum kicks are computed in advance and stored in a look up table. While the kick-plane method is fast and easy to compute and can even be applied if only position information from the META detectors is available, it does not provide very accurate results nor a high momentum resolution. Thus in Au+Au it is only used for tracking purposes.
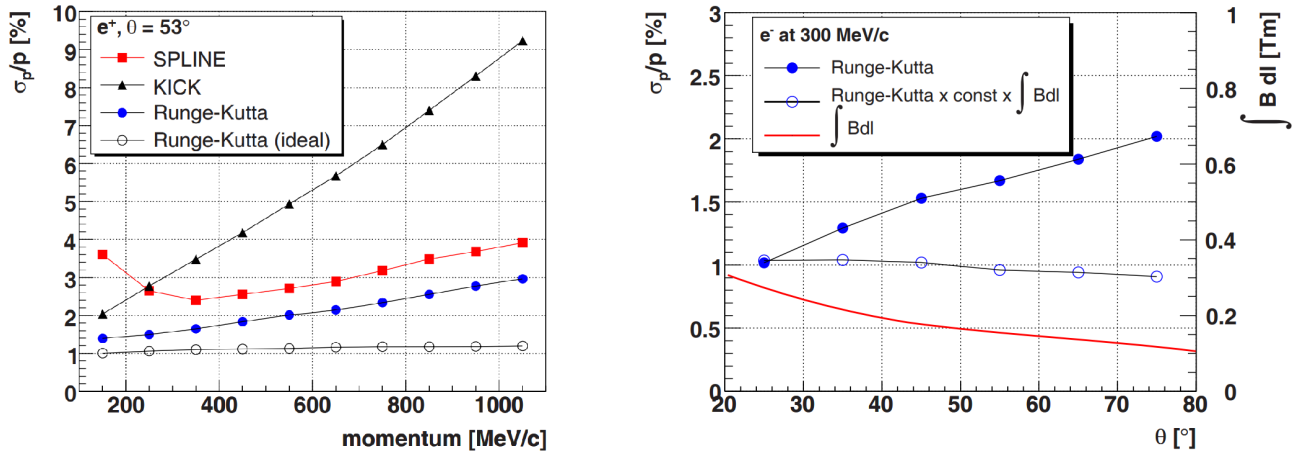
Figure 3.3: On the left different momentum reconstruction algorithms are compared in terms of their respective simulated momentum resolution of positron tracks at a fixed polar angle of 53°.
The right panel shows simulation results for the momentum resolution of $0.3\,\text{GeV/c}$ positrons at different angles (full symbols). The integrated magnetic field is indicated by the red line and the product of the resolution and the field integral (open symbols) shows, that the momentum dependence on the polar angle is due to the variation of $\int B\,dl$. [55]

A better precision can be achieved by using a cubic spline function to model the trajectory as a smooth curve passing through the detector hit points. Since this model is not exact, systematic corrections have to be applied later on. Further improvements are attained by solving the equations of motion of the particle in the field region numerically with the fourth-order Runge-Kutta method. Momentum, polarity, vertex and direction of the particle track are needed as initial conditions for the solution. The first two are provided by the spline method and the latter ones by the vertex fitter. Energy loss and multiple scattering is not taken into account, but since the material budget of the MDCs is very low, this does not have a large effect. The fit quality can be improved by iteratively modifying the track parameters to precisely fit the hit points measured in the MDCs. Figure 3.3 shows the simulated momentum resolution in dependence on the angle and the used reconstruction method. [55]

3.1.3 META-Matching

To obtain the full track information, the tracks from the MDC have to be combined with the time-of-flight information. Thus the reconstructed outer segment is matched with a hit in the Multiplicity Electron Trigger Array (META), consisting of the RPC, TOF Wall and Pre-Shower detector by extending the particles Runge-Kutta track. The quality of the position resolution in x direction is given by:

$$\text{metaQa} = \frac{\Delta x}{\sigma_x} \tag{3.4}$$

with Δx the distance between the extrapolated hit and the actual hit in the META detectors and σ_x the resolution of the position measurement. A deviation Δy in y-direction would lead to a hit in a different rod/cell of ToF/RPC and is therefore not used as a quality estimator.
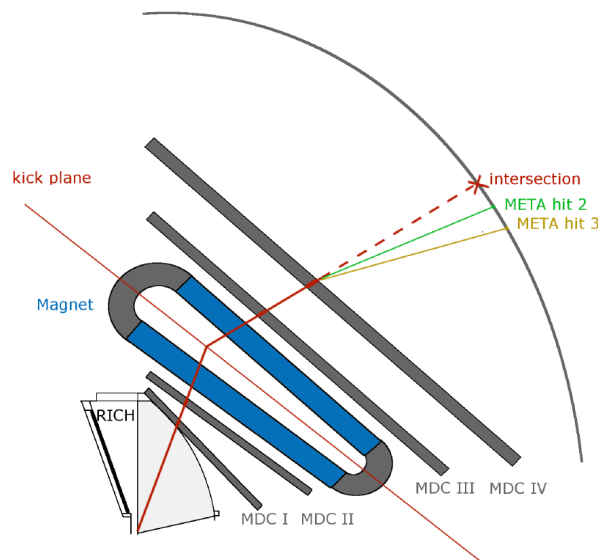
Figure 3.4: A sketch demonstrating the META matching procedure.

To match a META hit, the extended track has to point into the active volume, however a small deviation[2] on the Runge-Kutta track is allowed to account for multiple scattering. Especially in the more central collisions the matching of the track candidates to the META hits results in a large number of possible particle candidates. The best candidate is chosen by the matching quality.

3.1.4 RICH Ring Reconstruction

In case of a lepton, in addition to matching the outer MDC track segment to the META detectors, the inner segment is matched to a ring from the RICH detector. Thus ring shaped photon distributions in the RICH pad plane have to be found and reconstructed to be later on matched with the lepton track.

To reduce distortion of the ring finding procedure by background contributions like electronic noise or correlated background hits, a cleaning procedure is performed before the reconstruction. To get rid of direct hits by particles/fragments originating from the target region, groups of pads that contain at least one pad with very high charge (≥ 300 ADC ch.) are removed, since the typical maximum amplitude for Cherenkov photons lies at around 200 ADC channels. Furthermore single pads with small charges (≤ 5 ADC ch.), which are separated from the next fired pad by at least seven empty pads, are discarded. This corresponds to a charge threshold of $3 \langle \sigma \rangle$, where σ denotes the Gauss distributed noise signal of each pad, leading to a removal of 99.7% of all pads fired due to electronic noise.

Subsequently a labeling procedure is performed, which only tags areas that contain groups of fired pads as promising to be investigated by the ring finder algorithm. Due to the low occupancy in the pad plane, this reduces the computation time significantly. Pads are assigned to the same label, if they have a distance of less than seven pads to the next fired neighbor. Labels that are too small to contain a ring (typical ring radius is about four pads), are removed. The remaining labeled regions undergo the ring finder algorithm to search for a ring candidate.

Two different ring finder algorithms are available, one using a pattern mask and the other one based on the Hough transform. For the first one a 11×11-matrix is constructed based on hit distributions from real measured rings. All rings have been added up and the sum is then symmetrized and normalized to zero. The positive weight values form a ring, while the negative weights correspond to non-fired pads. Figure 3.5 shows a three-dimensional view of such a matrix on the left. To find a ring, the pattern matrix is compared to the hit distributions on the pad plane label by label. On a given label the matrix is shifted in a way, that each fired pad in the label overlaps once with each matrix slot. The Pattern Matrix Quality (PM quality) is estimated by adding up the weights of the matrix in each slot that coincides with a fired pad. For a good matching this value will be high, because most of the fired pads match with the ring shape. The position with the highest PM quality is is chosen and the center of the matrix is stored as the center of the ring candidate. To select rings with a certain quality, a threshold for the PM quality can be set. The value of the PM quality varies between 50 and 1500 and the threshold has to be set carefully in order to not discard too many real rings.

---

2   The size of the deviation is 4 mm for a straight line, i.e. high momentum particles and increases for lower momenta particles, which are more strongly distorted by multiple scattering.
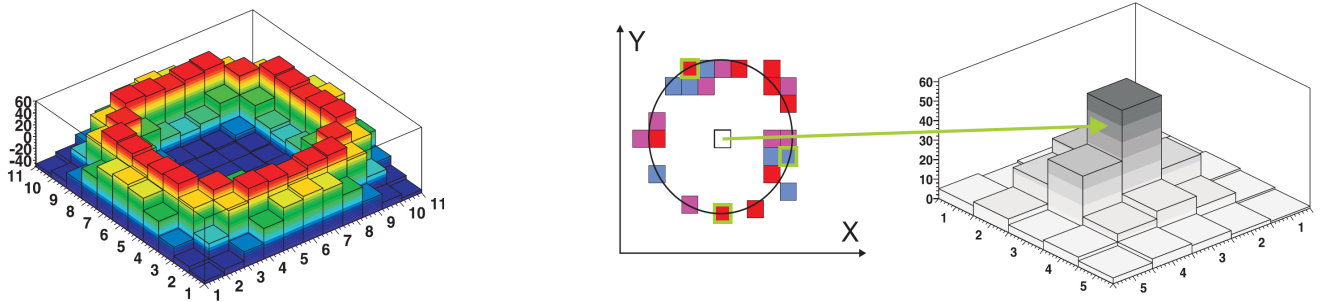
Figure 3.5: On the left a three-dimensional view of the pattern matrix mask is shown. It has positive weight values along the ring shape and negative weights were a non-fired pad is expected. [68]
The right panel illustrates the Hough Transform method. On the left a label on the pad plane is shown. The three currently selected pixels are marked in green and the circle fit to them is indicated. On the right the two-dimensional distribution of all accumulated ring centers for this label is plotted. The maximum of this distribution is the most probable position for the center of the ring. [68]

The second approach is the Randomized Hough Transform (RHT), a method for object identification. The circles are parametrized as a function of x- and y-position of the center and the ring radius r. The radius is fixed to four pads. In each step of the computation three fired pads from one label are chosen and the a circle is fit to them. The parameters x and y are saved and the operation is repeated for each triplet in the label. To reduce computing time and because of the fixed radius, the minimal distance between two sub-sequential pixels has to be larger than half the ring radius. The result is a two-dimensional distribution of the accumulated ring center positions in x and y, which can be seen in the right panel of Figure 3.5. The maximum of this distribution is chosen as the center of the RICH ring, since it coincides with the majority of pad combinations. The height of this maximum is the Hough Transform Quality.
Both algorithms have different advantages and disadvantages. While the Pattern Matrix algorithm is very fast, it has problems with identifying deformed rings due to electric noise or the overlap of two rings. The Hough Transform on the other hand does not strictly depend on the radius and is able to identify distorted rings. However, it will also misidentify large clusters of fired pads as rings. To benefit from the positive features of both algorithms they are used in combination. [68]

After the reconstruction the obtained rings have to be matched to the inner track segment from the MDCs. From all rings found in the event, the one is chosen for which the RICH matching quality

$$d_{\text{track-ring}} = \sqrt{\left(\Delta\theta_{\text{track-ring}}\right)^2 + \left(\Delta\phi_{\text{track-ring}} \cdot \sin\left(\theta_{\text{track}}\right)\right)^2} \qquad (3.5)$$

is the smallest. But this matching is only done under the condition, that $|\Delta\theta_{\text{track-ring}}| < 8°$ and $|\Delta\theta_{\text{track-ring}} \cdot \sin\left(\theta_{\text{track}}\right)| < 8°$. Otherwise no ring information is attached to the track. [69]

Instead of reconstructing the rings in the RICH detector and later on match them to their associated track, this procedure can be done the other way around. So the RICH detector is no longer used as an isolated system, but information from tracking and time-of-flight detectors in HADES is used to preselect electron candidates. For those preselected electron candidates the position information of the inner MDC chambers is used to predict the position of a possible signal in the RICH. This procedure is called backtracking.

All track candidates with $\beta > 0.95$ and an energy loss in the drift chambers below 10 as well as a good track quality ($\chi^2 < 1000$ of the Runge-Kutta fit) are chosen as lepton candidates. They are used to calculate the intersection of the track and the RICH mirror to predict the position of a possible ring center on the RICH pad plane. Afterwards, the region of expected photon hits has to be determined by using simulated electrons creating Cherenkov light. To be flexible in regards of the deformation of rings, parameters for azimuthal and polar angle and the position of the particle emission vertex are used to describe the ring shape. As a first step, the RICH response is compared to the calculated ring and it is searched for matching pads. Those matching pads are summarized into clusters and the local maximum of each cluster is determined. Based on the cluster positions and the number and positions of the local maxima within the region of interest the ring quality is estimated:

$$\chi^2_{\mathrm{BT}} = \frac{\sqrt{\sum_{n=1}^{N} \frac{\sqrt{\Delta x^2 + \Delta y^2}}{\sqrt{\sigma_{\mathrm{geom}}^2 + \sigma_{\mathrm{res}}^2}}}}{N} \tag{3.6}$$

Hereby N denotes the number of maxima per region of interest, Δx and Δy are the deviation in x and y direction between the maximum and the ring, σ_{geom} is the width of the photon distribution and σ_{res} is the resolution of the determination of the maximum position. This can also be done separately for x and y direction, which is useful for small momentum particles, since the reconstructed track might differ from the real trajectory due to the bending of the track in the inner MDCs and multiple scattering. Similarly to the pattern matrix quality of the RICH ring finder algorithm, the quality of the backtracking pattern matrix can be estimated by the fraction of pads directly matching in the region of interest to the ones on the circle. Both quality estimators provide a good distinction between good and bad rings, but they are only efficient for rings with a large number of maxima.

The advantage of this method compared to the previously used RICH ring finder algorithm is, that it is now possible to also detect overlapping rings, i.e. close pairs, and it is more tolerant to rings with lower quality, which leads to larger statistics in the final spectra. It also reduces the combinatorial background up to a factor of 4, because the higher lepton reconstruction efficiencies increase the probability of detecting incomplete lepton partners and in addition an opening angle cut can be applied. Thus the backtracking algorithm is used for electron identification in this analysis. [52, 53]

3.2 Event Selection

Having a clean sample of events is crucial to any analysis. Only events with a reaction inside the target should be analyzed and events with a vertex pointing to outside the target, e.g. the beam pipe or the target holder have to be removed. Likewise events without a reaction at all should be discarded. Overlapping events (so called pile-up events) distort the sample in a way that more particles are registered, leading to wrong centralities and collision times, thus they also have to be rejected. During the Au+Au beamtime HADES was running with two physical triggers (PT), one for low multiplicity events (PT2) and one for high multiplicity events (PT3). The latter one is part of the standard event selection flags used for this analysis. All used flags can be found in the following listing:

- **kGoodTRIGGER:** the number of TOF hits is above 20 (PT3 condition). Events with high multiplicity are selected, i.e. peripheral events are excluded.

- **kGoodSTART:** there is a correct hit in the START detector. This is important to allow for a time-of-flight calculation.

- **kNoPileUpSTART:** in case there is a cluster measured by the START detector, i.e. more than one hit in a time window of -5 to $15\,\mathrm{ns}$ around the collision, the event is rejected.

- **kGoodVertexClust:** to avoid events that originate from outside the target, e.g interaction of the Au beam with the START detector or the beam pipe, only events with a vertex position of $z > -65\,\mathrm{mm}$ are accepted.

- **kGoodVertexCand:** the same requirements are applied as for the vertex cluster, but at least two fully reconstructed candidates are required. Thus the criterion is more strict and also a good resolution perpendicular to the beam axis is achieved.

- **kNoVETO:** the VETO detector determines whether a collision with the target took place or not. If there is no collision a VETO hit is expected within $\pm10\,\mathrm{ns}$ around the START hit. In case of a collision there should be no VETO hit at all.

- **kGoodSTARTVETO:** events with a second START hit within 15 to $350\,\mathrm{ns}$ that has no correlated VETO hit within $\pm2\,\mathrm{ns}$ are excluded to prevent detector bias from the second event.

- **kGoodSTARTMETA:** events with a second START hit within 80 to $350\,\mathrm{ns}$ that is correlated to more than four hits in the META detectors within $7 \pm 5\,\mathrm{ns}$ are excluded to avoid wrong multiplicities by particles from the second event with unphysical time-of-flight measurements, since the offset of $7\,\mathrm{ns}$ corresponds to the fastest particles.

Furthermore certain event characteristics can be chosen as the extraction of a trend is only possible when there exist similar constraints such as the centrality class. And certain characteristics might be necessary for specific parts of the analysis. The used event characteristics are:

- **Number of good sectors:** at least four good sectors are required. The determination of a good sector is discussed in the paragraph below.

- **Centrality selection:** only the $40\,\%$ most central events are chosen for this analysis.

- **Reconstructed reaction plane:** The information of the reaction plane is needed determine the $\Delta\phi$ angle of the ejectiles which is crucial for the study of flow. Moreover the information is necessary for the estimation of the combinatorial background in the pair analysis. Therefore events without a reconstructed reaction plane are discarded.

Figure 3.6 summarizes the effect of the different event selection criteria. The axis on the left shows the number of events and on the right the quotient to the number of PT3 events is shown. From initially around $7\cdot10^9$ events $5.5\cdot10^9$ PT3 events are chosen and after all selection decisions about $2.6\cdot10^9$ events remain in the sample for dilepton analysis. This corresponds to around $47\,\%$ of PT3 events.
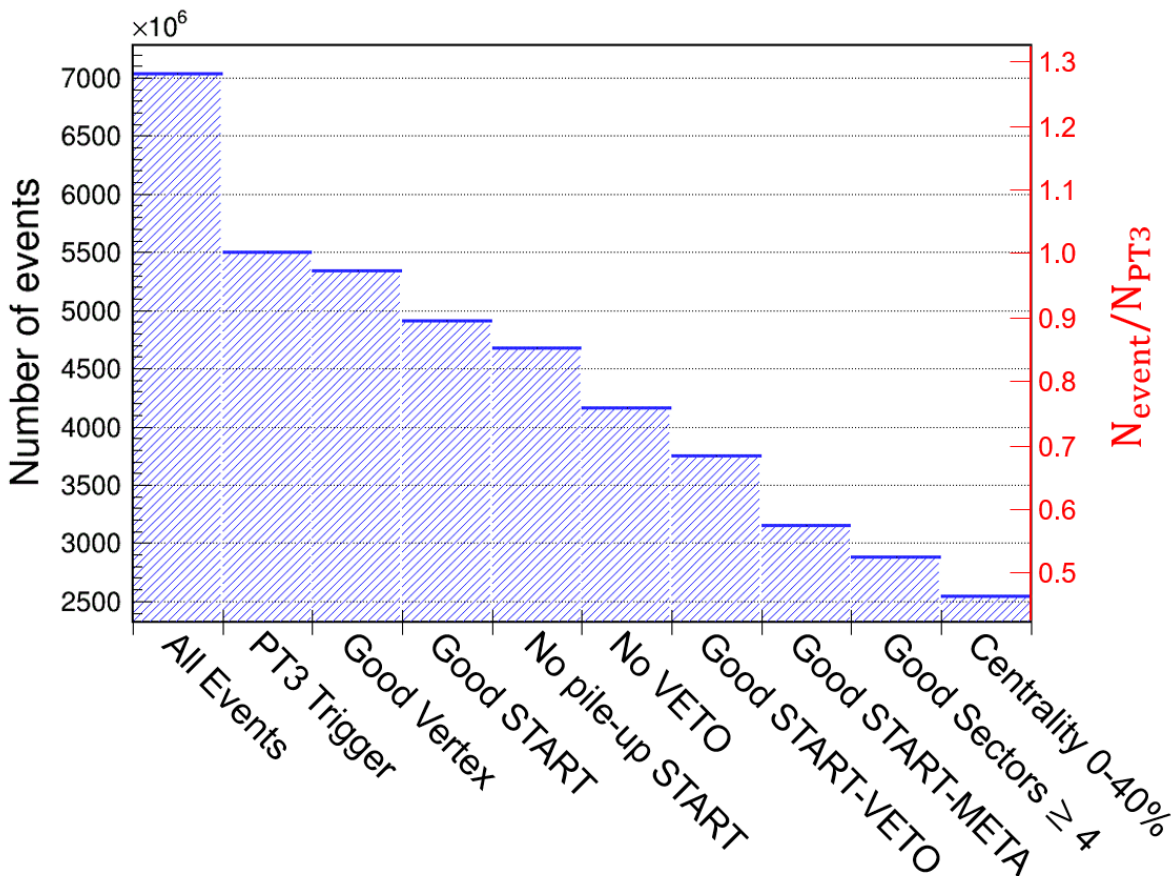
Figure 3.6: Number of events after each event selection step. The axis on the right is normalized to the number of PT3 events.

3.2.1 Sector Quality

During data taking it happened occasionally, that gas chambers of the RICH or MDC suffered from trips, leading to the affected part of the detector getting inefficient for a certain time. In case of the MDC this inefficiency additionally depends on the type of particle and its velocity, as it is larger for minimum ionizing particles. Sector 2 of the MDC (azimuthal angle $240° \leq \phi \leq 300°$) was affected almost the whole beam time. The best method to handle such detector problems in analysis is to exclude the problematic sectors from the data sample. This was done separately for each run of 2 to 3 minutes, since this time span is in the same

order than the time needed by an affected sector to fully recover. To make the decision about which sector should be removed, the number of reconstructed charged pions and RICH rings is plotted as a function of time. If the number deviates more than 3σ from the mean number, the concerned sector is marked as useless for hadron (number of pions) or lepton (number of RICH rings) analysis.

A reduced number of sectors alters the acceptance of the spectrometer. This prohibits a direct comparison of the Au+Au results with previous experiments where all 6 sectors were available. Hence an acceptance correction is applied to cancel this effect. For one to two missing sectors the correction factor reaches a maximum value of around 4. For three or less sectors a considerably larger correction would be needed, which leads to the decision to demand at least four good sectors. [69]

3.2.2 Centrality Selection

As mentioned in section 1.4 the centrality of an event denotes the size of the overlap region of the colliding nuclei. The larger the overlap, the more central the collision is. Simultaneously the distance between the centers of the two nuclei, called the impact parameter b, decreases with centrality while the particle multiplicity in the detector increases. Hence a higher number of measured particles is correlated to a more central event, which can be used as a selection criterion.

Centrality class	b [fm]	META hits	Multiplicity bin
$0-10\%$	$0.00-4.60$	$160-250$	1
$10-20\%$	$4.60-6.50$	$121-159$	2
$20-30\%$	$6.50-7.95$	$88-120$	3
$30-40\%$	$7.95-9.18$	$60-87$	4
$40-100\%$	$9.18-18.00$	$0-59$	5

Table 3.1: Definition of the different centrality classes as a function of hits in RPC and TOF. Multiplicity bin 0 denotes the $0-40\%$ most central events and is not listed here separately.

To model the particle multiplicities of two colliding nuclei, thus the centrality of this event, the Glauber Model can be used. It treats an A-A collision as a superposition of elementary nucleon-nucleon collisions. Hereby it makes the assumption, that the nucleons travel along straight lines and that after an ()inelastic) collision an exited (nucleon-like) hadron is created, which interacts with the same cross section. Nucleons that have experienced a collision are called wounded nucleons or participants, the other nucleons are called spectators. For a randomly generated impact parameter according to a probability distribution, the number of participants $\langle N_{\text{part}} \rangle$ and the number of binary collisions $\langle N_{\text{coll}} \rangle$ are simulated from many nucleus-nucleus collisions. Since those quantities are not measurable, they are called pseudo-observables and

cannot be used directly to determine the centrality. However, assuming that the particle production scales monotonically to $\langle N_{part}\rangle$ and $\langle N_{coll}\rangle$, those pseudo-observables can be used to calculate the charged particle multiplicity distribution. This distribution on the other hand can be measured by using the number of particle tracks, the number of META hits or the hits in the Forward Wall. Since the number of META hits provide the most precise estimation of the charged particle multiplicity, it is used for the centrality determination in this analysis. The relation between the pseudo-observable b and the measured hits in the META detector can be found in Table 3.1.

Due to the limited number of particles, the different centrality classes overlap as a function of the impact parameter, which is illustrated in Figure 3.7. But because the centrality classes are defined by the multiplicity distribution in the META detectors, the centrality classes would be clearly separated as a function of META hits.
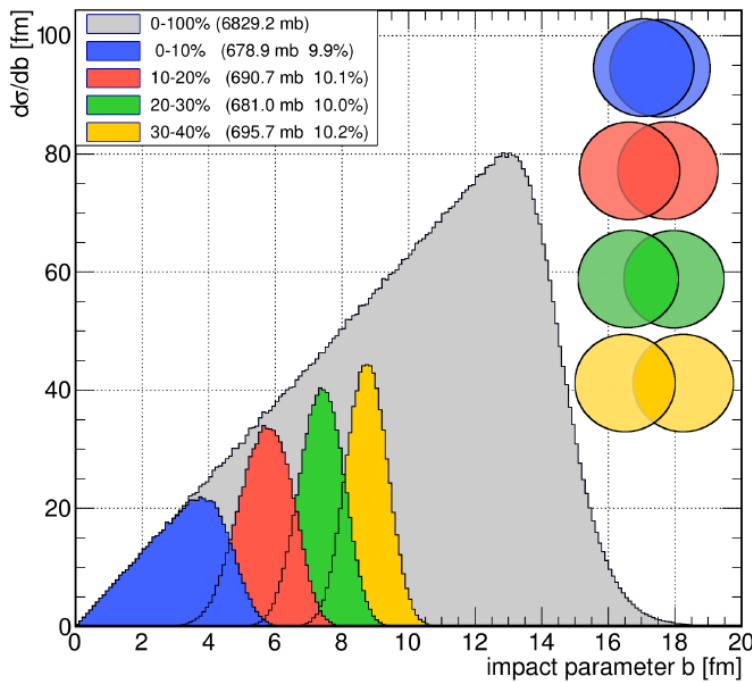
Figure 3.7: Distribution of the impact parameters in Au+Au minimum bias collisions and 10% centrality classes. The corresponding numbers can found in Table 3.1. [53]

3.2.3 Event Plane Reconstruction

To analyze the collective flow of charged particles produced in a collision the reaction plane of this collision needs to be known. To obtain this information a modified total transverse momentum transfer technique is used. It has to be modified since the forward wall cannot measure the transverse momentum of the spectators. According to this technique the reaction plane in each event is determined by the direction of the beam and the vector $\vec{Q}$. This vector is hereby given by the weighted sum of the transverse velocities of all charged spectators. The transverse velocities of the spectators can be substituted by the unit vectors of the positions of the triggered cells. This is possible because all spectators of an incident nucleus have the same velocity thus their transverse velocity vectors are oriented parallel to the respective spatial

vector of the spectator position in the plane perpendicular to the beam axis, i.e. the plane of the forward wall. Hence the vector $\vec{Q}$ is given by:

$$\vec{Q} = \sum_{i=1}^{N_{Sp}} \omega_i \frac{\vec{r_i}}{|\vec{r_i}|} \tag{3.7}$$

Where N_{Sp} denotes the number of spectators, i.e. the number of fired cells and $\vec{r_i}$ is the position vector of the ith cell. The sign of the weight is positive for particles flying forward in the center-of-mass system and analogously negative for particles flying backwards. The absolute value of the weight is set to unity since the hodoscope wall is incapable of measuring the transverse momentum of the particles. A slight improvement of the angular resolution might be possible by using the charge of the particle as weight value. But the effect is rather small. Eventually the azimuthal reaction plane angle ϕ_{RP} is defined as the angle between the X-axis and the vector $\vec{Q}$. [62, 70]

Since the beam position is not always exactly centered with respect to the forward wall, the positions of the cells have to be corrected for this shift. This procedure is called recentering. Initially this was done with one shift value for all events. Because the beam position varies over time (see Figure 3.8) performing time dependent recentering presumably improves the event plane resolution.
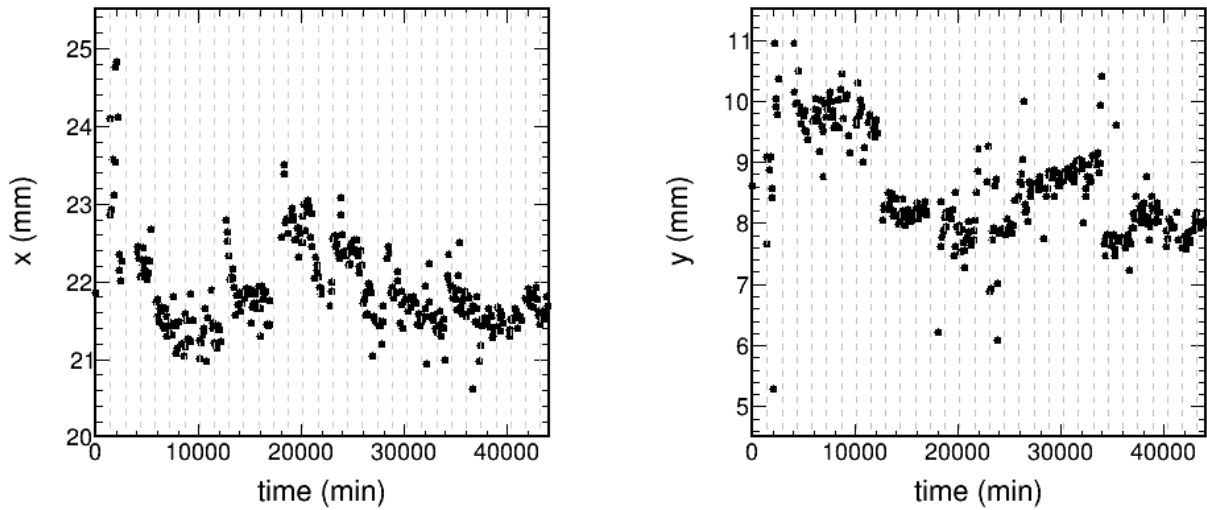
Figure 3.8: Mean Position of the beam in x and y over time during the 2012 Au+Au beamtime as measured in the Forward Wall. The individual days are indicated by the dashed lines.

31 values are used to do this correction, one for every day of the beamtime. Subsequently an anisotropy correction is performed. The reaction plane angle is expected to show a flat distribution, i.e. over all events all angles between $-180°$ and $180°$ should be equally likely. If the distribution is not isotropic, a correction is applied by fitting a function to the histogram and later on using the fit values for correcting the spectrum. This is done in 5 % centrality classes which is shown in Figure 3.9
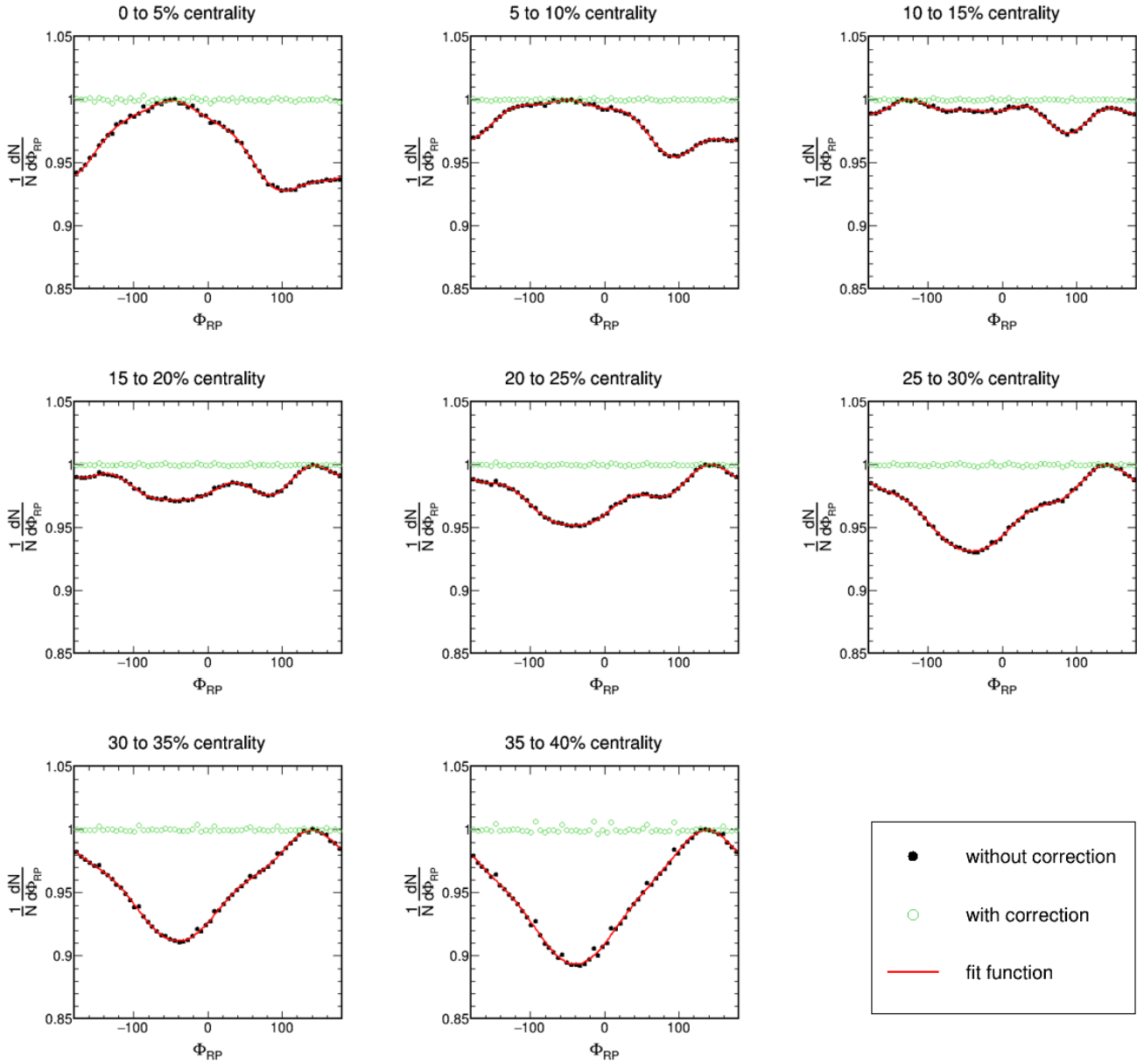
Figure 3.9: Anisotropy correction of the reaction plane angle. The plots show the normalized number of events $\frac{1}{N}\frac{dN}{d\phi_{RP}}$ versus the reaction plane angle ϕ_{RP} in 5 % centrality classes. The black dots are the data points before the correction, the fit function is plotted in red and the green circles show the distribution after applying the correction.

Applying the two corrections leads to an isotropic behavior of the reaction plane. After performing the time dependent recentering procedure it came apparent, that the improvements of the reaction plane resolution are negligible for the reconstruction of dilepton flow. Nevertheless it has no disadvantage to use more than one shift value.

3.2.4 Correction for Event Plane Resolution

As described in the section above, the event plane angle is determined using the spectator hits in the forward wall. Due to the finite number of spectators, the resolution of the event plane is limited. In general the reconstructed azimuthal angle ϕ^{rec} differs from the true azimuthal angle ϕ by an error $\Delta\phi$: $\phi^{\text{rec}} = \phi - \Delta\phi$. Averaged over many events and under the assumption that ϕ and $\Delta\phi$ are statistically independent the following relation is obtained:

$$
\begin{aligned}
\langle\cos(n\phi^{\text{rec}})\rangle &= \langle\cos(n\phi)\rangle \cdot \langle\cos(n\Delta\phi)\rangle \\
v_n^{\text{rec}} &= v_n \cdot R_n
\end{aligned}
\tag{3.8}
$$

As the mean value of the cosine is always less than one, the measured flow will be smaller than the real flow values. This is easily comprehensible, because the maximum flow is reached in the reaction plane frame and the measured values are smeared by the error $\Delta\phi$. Thus the reconstructed flow values have to be corrected by dividing v_n^{rec} by the event plane resolution. To evaluate the event plane resolution $R_n = \langle\cos(n\Delta\phi)\rangle$ a large sample of events with the same magnitude of impact parameter, experimentally determined for instance by their multiplicity, is considered. Since the number of particles used for event plane determination is large, the central limit theorem states, that the fluctuations of the event plane vector $\vec{Q}$ around its mean value $\langle\vec{Q}\rangle$ are gaussian. Under the assumption of isotropic fluctuations the two dimensional distribution of the event plane vector is then of the form:

$$
\frac{dN}{Q\,dQ\,d\Delta\phi} = \frac{1}{\pi\sigma^2}\exp\left(-\frac{|\vec{Q}-\langle\vec{Q}\rangle|^2}{\sigma^2}\right) = \frac{1}{\pi\sigma^2}\exp\left(-\frac{Q^2+\bar{Q}^2-2Q\bar{Q}\cos(\Delta\phi)}{\sigma^2}\right)
\tag{3.9}
$$

Without loss of generality an impact parameter parallel to the x-axis is chosen, thus $\vec{Q} = Q\left(\vec{e}_x\cos(\Delta\phi)+\vec{e}_y\sin(\Delta\phi)\right)$ and $\langle\vec{Q}\rangle = \bar{Q}\,\vec{e}_x$. By integrating Equation 3.9 over $\Delta\phi$ and Q the Fourier coefficients can be calculated. Thus for the event plane resolution it follows:

$$
R_n = \langle\cos(n\Delta\phi)\rangle = \frac{\sqrt{\pi}}{2}\chi e^{-\chi^2/2}\left[I_{\frac{n-1}{2}}\left(\frac{\chi^2}{2}\right)+I_{\frac{n+1}{2}}\left(\frac{\chi^2}{2}\right)\right]
\tag{3.10}
$$

The dimensionless parameter $\chi = \bar{Q}/\sigma$ scales like $\sqrt{N}$, because $\bar{Q} \propto N$ and $\sigma \propto \sqrt{N}$. I_k denotes the modified Bessel function of order k. To determine the value of R_n, χ has to be estimated from the experimental data. On that account each event is randomly divided into two sub-events A and B containing N/2 particles each. And the resolution of the event plane is calculated from the correlation of the event planes of those independent sub-events:

$$
\langle\cos(n(\psi_A-\psi_B))\rangle = \langle\cos(n\psi_A)\rangle \times \langle\cos(n\psi_B)\rangle
\tag{3.11}
$$

The easiest way is to calculate the fraction of events with a relative angle $\psi_{AB} = \psi_A - \psi_B$ larger than $90°$ or smaller than $-90°$:

$$
r = \frac{\int_{-180°}^{-90°}d\psi_{AB}+\int_{90°}^{180°}d\psi_{AB}}{\int_{-180°}^{180°}d\psi_{AB}} = \frac{\exp\left(-\chi^2/2\right)}{2}
\tag{3.12}
$$

Figure 3.10 shows the distribution of ψ_{AB} for the 40% most central events. The limits of integration are indicated and the two regions that contribute to the numerator of Equation 3.12 are highlighted. By rearranging this equation the parameter χ that is needed for the calculation of the event plane resolution is obtained: $\chi = \sqrt{-2\ln(2r)}$.
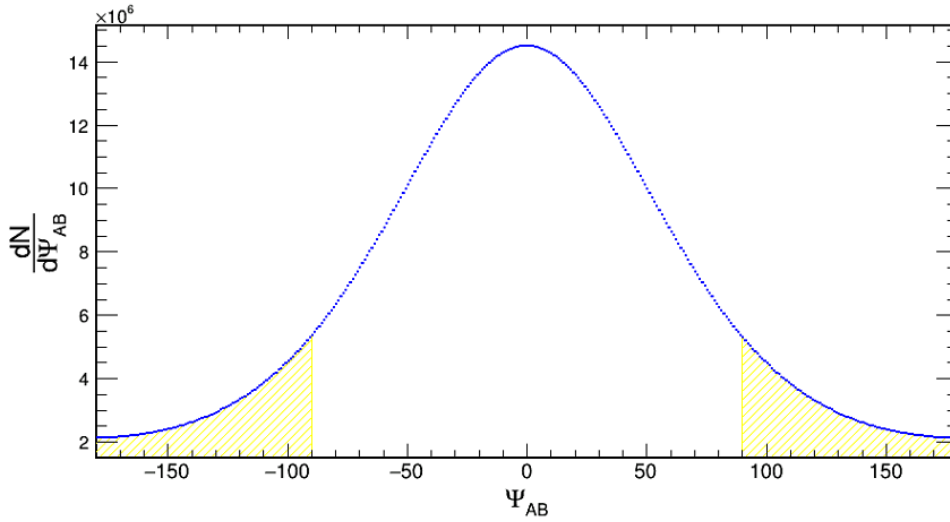
Figure 3.10: Distribution of $\psi_{AB} = \psi_A - \psi_B$ for the 40% most central events. The highlighted area divided by the integral over the whole spectrum gives the ratio r from Equation 3.12, which is used to estimate the accuracy of the event plane.
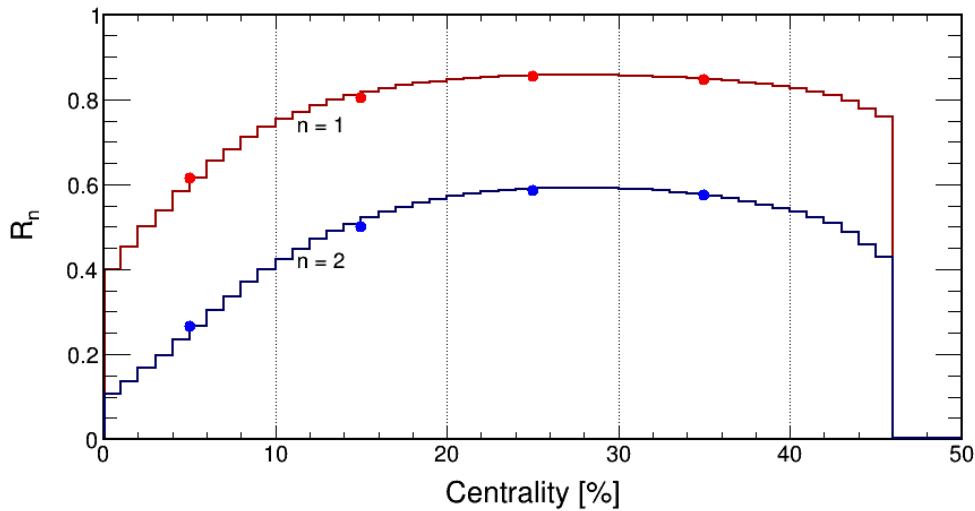
Figure 3.11: Event plane resolution as a function of centrality for the first and second order. The circles show the values used to correct the flow in the 10% centrality bins.

Because the number of spectators varies with the centrality of an event, the resolution of the event plane is centrality dependent. For the most central events only few spectators hit the forward wall, leading to a rather poor resolution. The highest resolution is reached for semi-central events with 25−30% centrality. For the more peripheral events the event plane resolution drops

again, due to the fragmentation of the spectators[3]. Thus the resolution has to be calculated for each centrality separately. Furthermore the resolution also depends on the order of n the flow coefficient. For a distribution of width δ, the resolution of the reaction plane $R_n = \langle \cos(n\Delta\phi) \rangle$ decreases with n and becomes small for $n > 1/\delta$. Thus the higher the order, the lower the resolution. A consequence is, that it becomes increasingly difficult to reconstruct higher order flow contributions. In Figure 3.11 the resolution of the event plane for the first and second order is shown as a function of centrality. For this analysis the ψ_{AB} distribution is filled for the 10 % centrality classes and the correction factor is calculated for each class independently. The resulting values are indicated with circles in the same plot. [71–73]

3.3 Singe Lepton Identification

Dileptons are very rare probes with branching ratios of e.g. $\Gamma_{ee}/\Gamma = (4.72 \pm 0.05) \cdot 10^{-5}$ in case of the ρ-meson [17]. Thus a very precise particle identification is crucial for reliable measurements. To separate the leptons from the hadronic background hard cuts in one or two dimensions can be applied on various observables. However, those cuts are inflexible, since they concentrate only on one or two variables, while ignoring all other dimensions. Furthermore, it is very difficult to choose the optimal set of all hard cuts. For this reason a Multi-Variate Analysis (MVA) is introduced, which is able to optimize a multidimensional set of conditions in all variables at once.
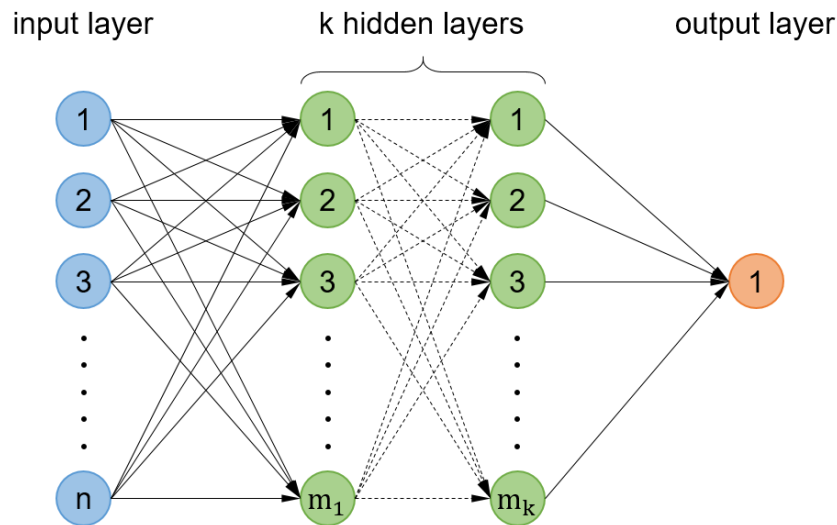
Figure 3.12: A schematic view of a multilayer perceptron. The different layers do not need to have the same number of nodes. Each connection has a weight, corresponding to the importance of the respective input.

A Feed-Forward Multi-Layer Perceptron (MLP) is a type of artificial neural network that is used to perform the MVA. Mathematically it is described by a function $y : \mathbb{R}^n \rightarrow [0, 1]$. The condition $y(x_1, ..., x_n) = c$, $c \in [0, 1]$ defines a $(n-1)$-dimensional surface in the n-dimensional

---

[3]   In peripheral events the spectators are not only single nucleons, but also larger chunks of several nucleons, that hit the Forward Wall and are counted as one hit. Thus the number of hits decreases for more peripheral events, although there are less particles taking part in the collision, i.e. more possible spectators.

input space $x_1, ..., x_n$. The points in the space represent simultaneous measurements of all quantities for a single event. They are separated by the plane into points that are accepted $(y(x_1, ..., x_n) > c)$ or rejected $(y(x_1, ..., x_n) < c)$.

The MLP consists of multiple layers of computational units: one input-layer, one output-layer and an arbitrary number of hidden layers, which perform intermediate steps of the calculation. Each layer contains nodes, that are connected to all nodes in the preceding layer (except for the nodes in the input layer) and their values are calculated based on the values of the nodes they are connected to. A schematic view of a multilayer perceptron can be seen in Figure 3.12.

In order to give the correct response, the system has to be trained with highly pure signal and background samples. Those training samples are taken from experimental data in case of the RICH ring finder algorithm. To assure the high purity, a very strong cut on the matching between tracks and the rings in the RICH detector $(d_{track-ring})$ is applied. One difficulty is, that the quantities used for the definition of the training signal and background samples cannot be used as an input to the MLP. Since they provide obviously the perfect discrimination between signal and background, they would be preferably chosen by the neural network, while all the other variables would be assigned with weights close to zero, resulting in a MVA that basically reproduces only the strict hard cuts on the training sample. Therefore a different set of input variables has to be chosen.
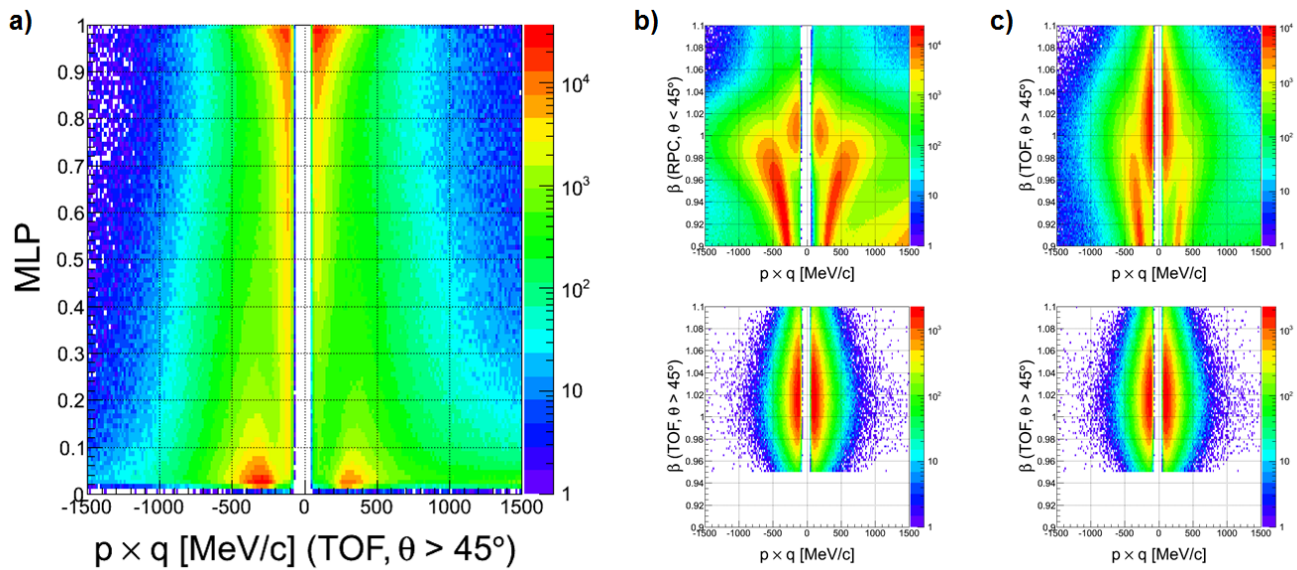
Figure 3.13: a) The plot shows the output of the neural network response function, which is the probability that a given particle is a lepton. Thus the leptons are found close to one, while the hadrons are around zero.
b) The two plots show the output of the RPC detector before (top) and after (bottom) the cut is applied. Before the cut, the lepton signal is overlapping with the one from the pions. After the cut the signal purity is about 99%.
c) The two plots show the output in the TOF region before (top) and after (bottom) the cut [74].

In case of backtracking simulated data containing tracks that passed the electron candidate selection are used as training sample. Many variables describing the ring identification (number of fired pads in the region of interest, number of clusters, number of maxima, sum of charge,

ring quality, etc.), as well as other variables concerning the track like the META matching quality or the quality of the Runge-Kutta fit and basic properties like momentum or velocity are given as an input to the MLP. The output of the neural network response function is the probability that a particle belongs to the signal, i.e. is a lepton. In Figure 3.13 this probability and the resulting cuts can be seen.

The purity of the lepton signal can be checked by looking at the momentum distribution. A clean electron identification should lead to an exponentially decaying spectrum. A contamination by hadrons leads to a deviation from this shape. Figure 3.14 shows a comparison between the electron identification using hard cuts both for the ring finder algorithm and for backtracking and the MVA in combination with backtracking. For momenta $p < 500\,MeV/c$ all three methods show an exponential shape. The MVA is clearly able to reconstruct much more electrons in this region, due to the reduced RICH response requirements. Above $500\,MeV/c$ both hard cut analysis show a contamination by hadrons. The effect is larger for the backtracking algorithm, since the RICH matching quality of the standard ring finder algorithm applies a stronger condition than the single backtracking observables. The MVA on the other hand still follows the exponential decay up to $700\,MeV/c$, where it shows a step, because a more significant RICH response is needed at high momenta to suppress hadron tracks.
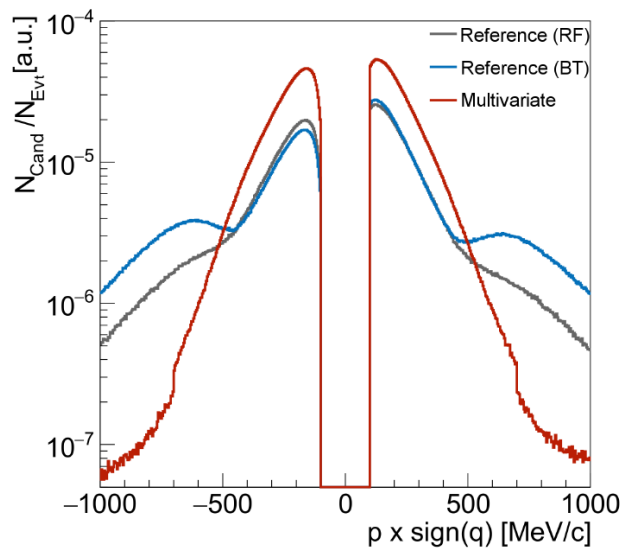
Figure 3.14: The plot shows the momentum distribution in the acceptance of the RPC detector after the single electron identification. The three curves compare the results obtained by using hard cuts and the RICH ring finder algorithm (grey) or the backtracking algorithm (blue) and the MVA in combination with backtracking (red). [53]

In conclusion, the combination of the multivariate analysis with the backtracking algorithm leads to a clearly enhanced lepton reconstruction efficiency compared to the RICH ring finder algorithm as well as a very high purity of single lepton identification with at least 98 %. [53, 69, 74, 75]

3.4 Dilepton Analysis

In order to take the step from the reconstructed single electron signal to the dilepton spectra, the electron-positron pairs have to be build. Since there is no information about the decay vertex of a particle available, it is not possible to identify electrons and protons from the same vertex. Instead all possible unlike-sign pair combinations are calculated event by event. Of course this leads to a large contribution of wrong pairings to the final spectra. This so called combinatorial background has to be subtracted from all pairs to obtain the true signal pairs.

Usually two types of fake lepton pairs are distinguished, namely uncorrelated and correlated background. The former one stems from the pairing of leptons, originating from different mother particles, as pictured in the left panel of Figure 3.15. This is the largest contribution to the combinatorial background and due to the random combination of two different decays it is structureless. In case of a two-photon decay, or a Dalitz decay with subsequent photon conversion of a neutral meson, it can happen, that the paired leptons have different mother particles but share their grandparent. The right side of Figure 3.15 shows such a case. The correlation of the pair leads to a background contribution with a bump-like structure.
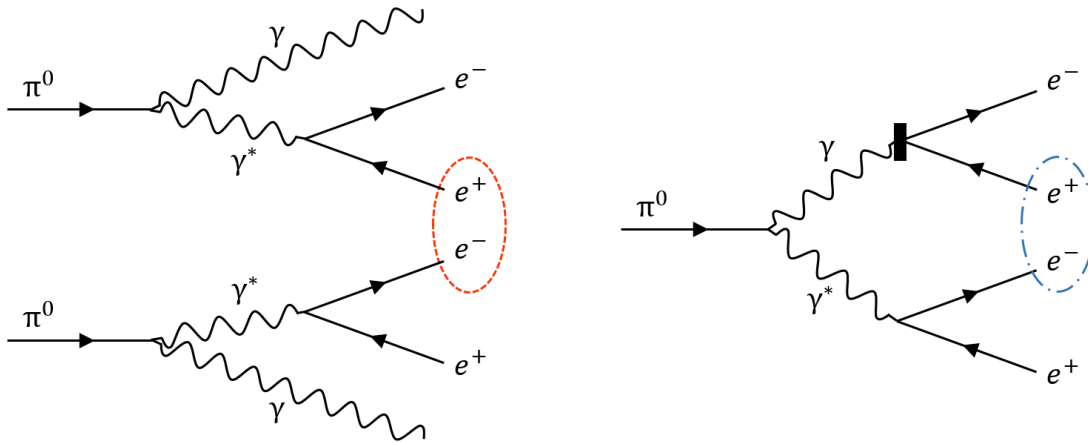
Figure 3.15: Combinatorial background can have different sources. The left diagram shows lepton pairs from different decay vertices, resulting in uncorrelated background. On the right the leptons are originating from the same source, which leads to correlated background.

Furthermore instead of real leptons, also hadrons or fake tracks from a wrong combination of detector hits contribute to the background. Figure 3.16 shows the different sources of combinatorial background obtained from a simulation by Patrick Sellheim [53]. A cocktail with π^0, η and dielectrons from a coarse-grained transport approach, embedded into UrQMD events, has been used. After the particle identification procedure described in the last section, they are categorized in leptons (LEP), hadrons(HAD) and fake matches (FAKE) using the Monte Carlo information.

As mentioned before, the largest contribution stems from uncorrelated lepton pairs. Since uncorrelated lepton pairs originate from π^0-decays, they are mostly present in the low-mass region. Fake tracks are most often paired with a lepton, producing uncorrelated background over the whole mass-range. Pairs containing a hadron are very rare, which confirms the high purity of the single electron signal.

The uncorrelated background can be reproduced using event mixing, while the correlated back-
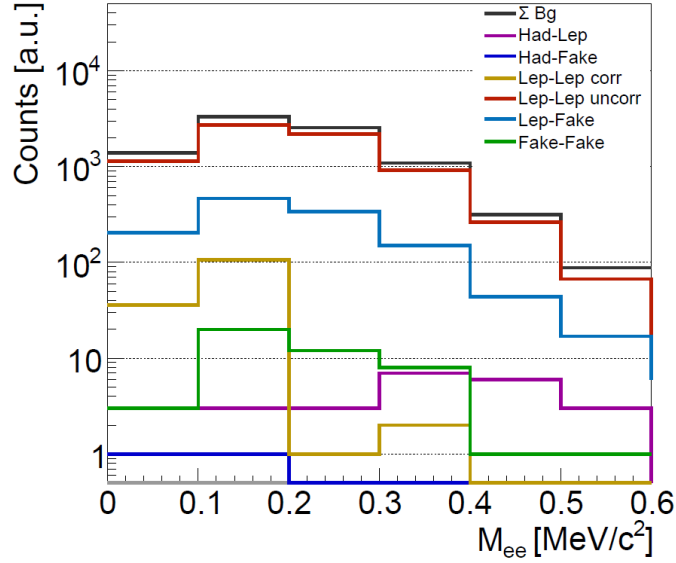
Figure 3.16: The plot shows fractions of different pair combinations that contribute to the combinatorial background obtained from simulation. The reconstructed single leptons are scaled down by a factor of 2 to account for the overestimated efficiency in simulation. [53]

ground is handled using a same-event like-sign background. The used methods are described in the sections below.

3.4.1 Same-Event Like-Sign Background

One method to obtain the combinatorial background, is to intentionally build purely combinatorial pairs. The probability to build a combinatorial e^+e^- pair is identical to the probability to build a like-sign pair (e^+e^+ or e^-e^-) in this event. This holds true not only for uncorrelated pairs, but also for correlated background, since the like-sign pairs can be correlated in the same way as the unlike-sign pairs (see Figure 3.15 on the right). To account for asymmetries in the number of positively and negatively charged particles, the geometric mean of those two distributions is taken:

$$\langle N_{e^+e^-} \rangle \;=\; 2\sqrt{\langle N_{e^+e^+} \rangle \langle N_{e^-e^-} \rangle} \tag{3.13}$$

This kind of background was studied for the dimuon spectrum of the NA50 experiment [76–78]. Equation 3.13 is derived using the assumption of Poisson distributed parent particle multiplicities and by neglecting the momentum correlation for correlated background pairs. Low-mass dileptons from hadron decays are always produced in pairs, i.e. correlated and their parents do not exhibit a statistical distribution of their multiplicity. However, looking at Figure 3.16 shows, that correlated pairs do only have a small contribution in the π^0 mass range and is negligible above. More information about the background pair combination in case of a non-Poisson distributed spectrum can be found in Appendix A of [79].

3.4.2 Mixed-Event Background

To create uncorrelated combinatorial background, also leptons from different events can be mixed and combined into pairs. This technique provides a large statistics, since there exist much more possible combinations and electrons from a given event are used multiple times. Randomly mixing leptons from all given events can introduce a bias, since their features can differ over time and different event characteristics. Thus for an accurate background description the following event properties have to be taken into account:

- **Centrality:** The reconstruction efficiency for electrons is dependent on their centrality. Only events within the same 10 % centrality class are mixed with each other.

- **Reaction vertex:** The acceptance varies with the vertex position. Thus the events are separated into seven 6 to 8 mm sized vertex bins.

- **Event plane angle:** To analyze flow effects, which depend on the emission angle of the particles, only particles with similar angles should be mixed. In order to obtain higher statistics, not fixed bins of event plane angle regions are used, but a condition on the maximum difference between the angles of particles that can be mixed. This difference should not exceed 15°.

- **Time:** Due to small efficiency losses in different detectors for certain time periods, which alter the particle reconstruction efficiency, not all events from the whole beamtime should be mixed. Therefore a good trade-off between high statistics and short timescales has to be found. Finally 250 files are chosen as the number of files to mix events from.

Another important parameter is the size of the event buffer. Event mixing basically works with equally sized buffers of each event class, which store single events, where each event contains lists with the electrons and positrons in it. As soon as the buffers are filled, the leptons from one event in the buffer are combined with the leptons from every other event. As soon as another event of the given event class arrives, the oldest event is removed from this buffer and the procedure is executed again. Consequently, the larger the buffer size, the larger the statistics, as long as the number of identified leptons is sufficient to fill the buffers. Since electrons and positrons are only mixed within the same event class, which depends as mentioned above on centrality, reaction vertex, event plane angle and time, the size of the buffer has to be chosen accordingly to those characteristics. Stricter conditions lead to the usage of a smaller buffer, while for looser requirements a larger buffer can be chosen. Thus the selection of all event mixing parameters has to be tested and optimized. Further constraints are, that at least two leptons have to be identified in an event used for mixing. This is important, since the different input types modify the shape of the background distribution strongly (See Figure 3.17 on the right). Because for same-event like-sign background the presence of at least two electrons per event is necessary, the same condition is chosen here.

The number of centrality classes and vertex bins is chosen as suggested in [53] for the standard event mixing setup, i.e. seven vertex bins and 10 % centrality classes. The impact of changes in those parameters can be seen in the left panel of Figure 3.17. Since in this analysis a special
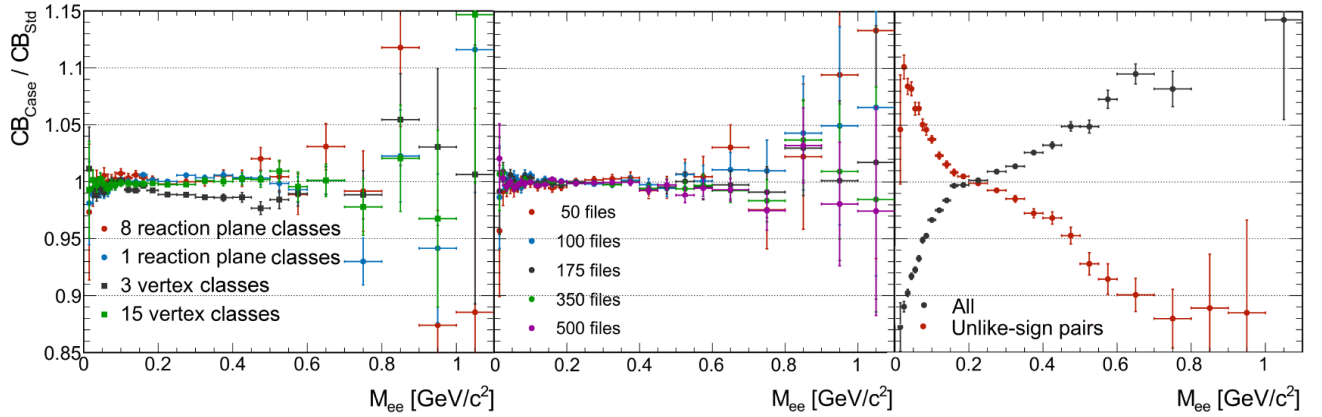
Figure 3.17: Variation of the combinatorial background obtained in event mixing due to changes in different event characteristics in relation to the standard event mixing setup. On the left the number of vertex bins and reaction plane classes is altered. The middle plot shows the influence of the number of input files, i.e. the timescale. A comparison between different input types is shown on the right. [53]

interest lies on the angular distribution of the dileptons, the standard four event plane classes are too coarse grained. In order to decrease the size of the event plane bins, either the number of files, i.e. the timescale has to be increased or the buffer has to be smaller. Also a combination of both is possible. Furthermore mixing can be done without waiting for the buffer to be filled, which allows to set a larger buffer size again to gain statistics, which is chosen for this analysis. In [53] it was shown, that the influence of the number of files on the shape of the background distribution is rather small (see Figure 3.17 in the middle). Thus the number of input files can be used to adjust the number of particles in a certain class after stricter angular cuts are applied. In order to reduce runtime, a set of mini-DST files was produced, which only contains events with at least two identified leptons. This condition would be applied anyway, so for mixing it does not make a difference if the full files or the extracted ones are used. And the extracted files allow to combine a lot more files per job than the original DST. Since the runtime is reduced drastically, also quick tests of parameter changes are possible. After testing several different bin sizes for event plane angle, a range of 10 to 15° per bin was found to be optimal. To increase the statistics while still using a rather strict angular constraint, instead of fixed event plane angle bins (e.g. particles with angles between $0 - 15°$, $15 - 30°$, etc.) all particles with a difference between their angles of less than $10°$ are mixed. For the final analysis the full DST was used as well as 250 files per job as it is suggested in the standard event mixing procedure.

3.4.3 Correction for sign dependent reconstruction asymmetries

In HADES the acceptance and reconstruction efficiency for electrons and positrons is not the same. Since they carry opposite charge, their deflection in the magnetic field goes in different directions which leads to sign dependent reconstruction asymmetries. For the same-event like-sign background a different charge combination is used than for the actual unlike-sign background. Thus a correction has to be applied.
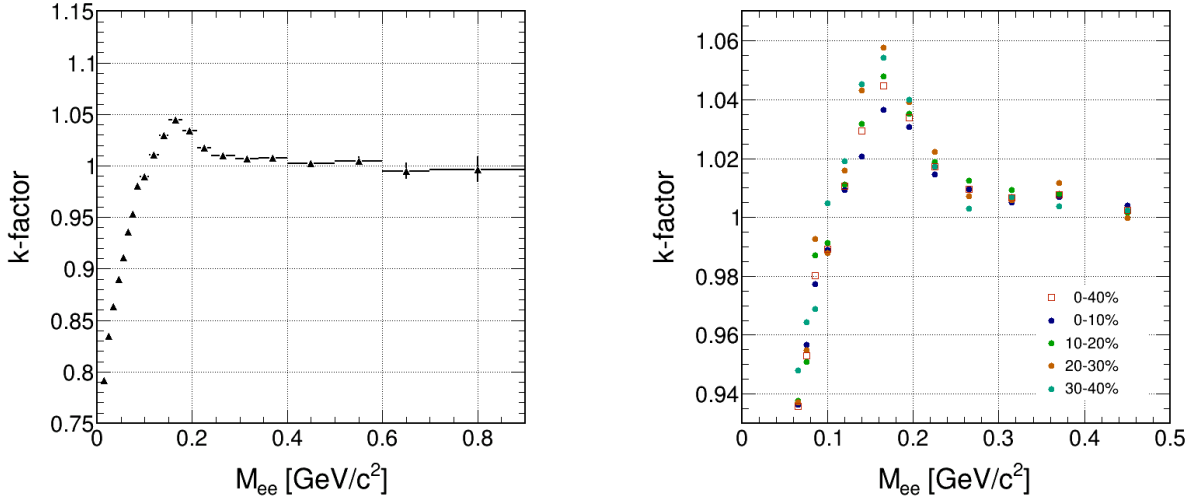
Figure 3.18: The two plots show the k-factor as function of invariant mass. In the right panel also the effect of centrality is shown. Since the points are lying very close to each other it is zoomed in and the error bars are not plotted to increase visibility.

To calculate the correction factor, the so called k-factor is constructed, using the like-sign and unlike-sign pair distributions obtained from event mixing:

$$k = \frac{N_{e^+e^-}}{2 \cdot \sqrt{N_{e^+e^+} \cdot N_{e^-e^-}}} \tag{3.14}$$

Figure 3.18 shows the shape of the k-factor as a function of invariant mass. At masses below $0.1\,\mathrm{GeV/c^2}$ a large deviation from unity is visible. The advantage is, that in this region the background is clearly lower than the signal, which diminishes the effect of the background shapes. At $0.15\,\mathrm{GeV/c^2}$ the maximum of around $5\,\%$ deviation is reached and above $0.25\,\mathrm{GeV/c^2}$ the k-factor stays close to one. The k-factor is evaluated and applied for all centrality classes separately. As it can be seen in the right panel of Figure 3.18 it has a very similar shape for all centralities, but is slightly smaller for more central events. This is expected, since the effects of efficiency and acceptance are the same for all centrality classes. The slight decrease for the most central events might be due to fake tracks which reduce the imbalance of the charged particle reconstruction.

In Figure 3.19 the resulting dilepton spectrum for $0-40\,\%$ centrality is plotted. The combinatorial background consists of the same-event like-sign geometric mean background multiplied with the k-factor up to an invariant mass of $M_{ee} = 0.12\,\mathrm{GeV/c^2}$. For the higher masses the mixed-event background is used. In the lower panel the resulting signal to background ratio is shown.
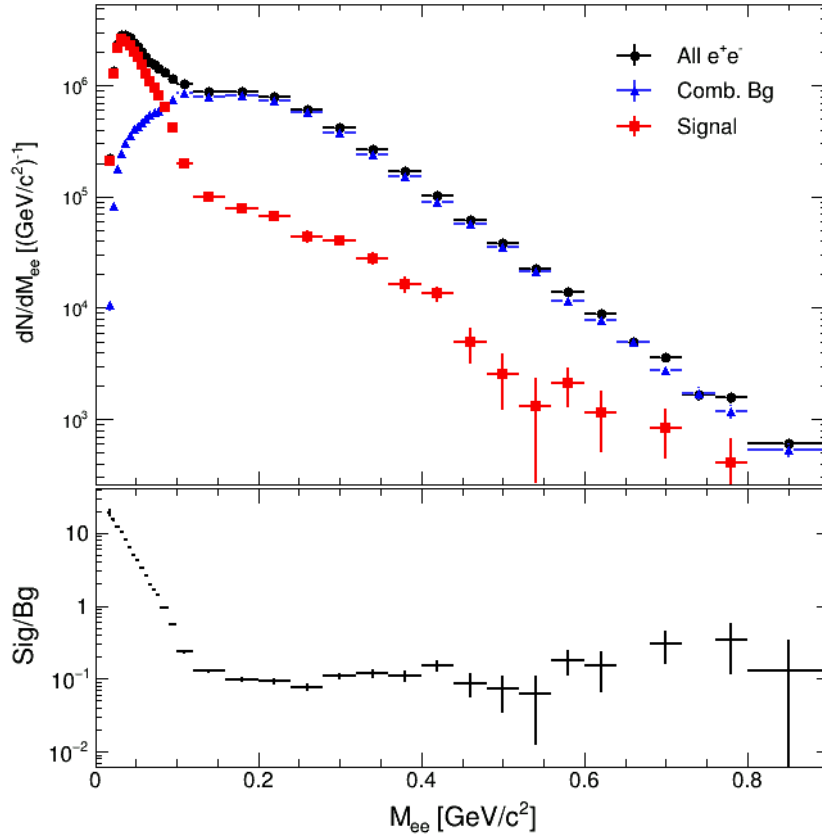
Figure 3.19: The resulting dilepton spectrum and signal to background ratio.

3.5 Flow Reconstruction

To extract the $\Delta\phi$ of dileptons the azimuthal angle of the dilepton pair is subtracted from the angle of the event plane, which is determined using the information of the spectator hits in the Forward Wall. This subtraction is necessary due to the correlation between the directed and elliptic flow components and the collision geometry.

The $\Delta\phi$-angle is extracted in four mass bins, summarized in Table 3.2. In the first mass bin up to $0.12\,\mathrm{GeV/c^2}$, which is dominated by π^0-Dalitz decays, correlated background pairs contribute significantly to the combinatorial background. Thus the same-event like-sign geometric mean method is used to determine the background is this mass region. For the three other mass bins the event mixing approach is chosen for background estimation.

The most direct approach to obtain the flow components v_1 and v_2 is to fit a Fourier expansion to the $\Delta\phi$ signal and extract the fit parameters and their errors. However, this method can get difficult when statistics is low or the background contribution is high. To deal with those difficulties, one can fit two separate Fourier expansions to the data and the background. The actual flow of the signal can then be calculated using the parameters extracted from the two fits.

Mass range [GeV/c^2]	# all e^+e^- pairs	# signal pairs	SIG/BG-ratio
$0.00 - 0.12$	171 880	114 783	2.01
$0.12 - 0.25$	109 225	12 969	0.13
$0.25 - 0.50$	58 920	7 194	0.14
$0.50 - 0.90$	3 008	573	0.24

Table 3.2: Summary of the four mass regions for the flow analysis.

Starting from the number of total, signal and background pairs, one can differentiate with respect to $\Delta\phi$:

$$N^{tot} = N^{sig} + N^{bg}$$

$$\frac{dN^{tot}}{d\Delta\phi} = \frac{dN^{sig}}{d\Delta\phi} + \frac{dN^{bg}}{d\Delta\phi} \tag{3.15}$$

Using the Fourier expansion

$$\frac{dN}{d\Delta\phi} = c \cdot \sum_{n=1}^{\infty} v_n \cdot \cos(n\Delta\phi), \tag{3.16}$$

where the constant c corresponds to the number of entries and v_n denotes the Fourier coefficients, leads to:

$$N^{tot} \cdot \sum_{n=1}^{\infty} v_n^{tot} \cdot \cos(n\Delta\phi) = N^{sig} \cdot \sum_{n=1}^{\infty} v_n^{sig} \cdot \cos(n\Delta\phi) + N^{bg} \cdot \sum_{n=1}^{\infty} v_n^{bg} \cdot \cos(n\Delta\phi) \tag{3.17}$$

Now the coefficients of each summand can be compared, which gives:

$$N^{tot} v_n^{tot} = N^{sig} v_n^{sig} + N^{bg} v_n^{bg}$$

$$\Leftrightarrow \quad v_n^{sig} = \frac{N^{tot}}{N^{sig}} v_n^{tot} - \frac{N^{bg}}{N^{sig}} v_n^{bg} \tag{3.18}$$

$$= \frac{1}{r} \left[(r+1) v_n^{tot} - v_n^{bg} \right]$$

Hereby is r the mass dependent signal to background ratio. The last line of equation 3.18 can also be found in [80].

The Fourier coefficients v_n are given by the mean value of the cosine:

$$v_n = \langle \cos(n\Delta\phi) \rangle \tag{3.19}$$

Thus instead of filling histograms with the $\Delta\phi$ distribution and fitting the Fourier expansion to it, it is also possible to fill profiles with $\cos(\Delta\phi)$ and $\cos(2\Delta\phi)$ to directly obtain the v_1 and v_2 flow coefficients, since the profiles calculate the mean value of the input event by event. This has the advantage, that the binning of the histogram does not influence the outcome. To visualize this effect a $\Delta\phi$ flow signal was simulated with a hundred million events and filled into histograms with 15 (low), 30 (mid) and 60 (high) bins between $-180°$ and $180°$ and a profile. Subsequently the flow analysis was performed and the flow coefficients were extracted.
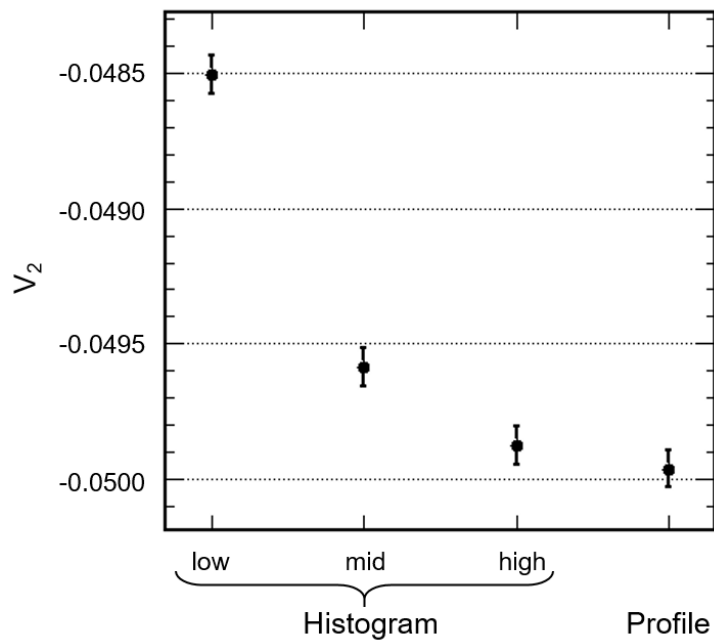
Figure 3.20: Comparison between histograms with a low (15), mid (30) and high (60) number of bins and a profile. Only the result of the profile reproduces the input value of $v_2^{input} = -0.05$. The higher the bin number, the closer the histogram result comes the profile output.

Figure 3.20 shows the result for v_2. Only the profile value agrees with the input of $v_2^{input} = -0.05$. The histogram with the high number of bins at least agrees within errors with the profile. The lower the bin number, the further away is the result from the input. In case of 360 instead of 60 bins for the last histogram, the result coincides exactly with the profile. Since statistics are not high enough to use such a fine binning, the profiles are the better alternative and more convenient to use.

The handling of the combinatorial background plays an important role in the analysis of dilepton flow. As mentioned before, the same-event like-sign method and the event-mixing method are available for background estimation. Both can be used to fill profiles with the background flow values and subsequently use Equation 3.18 to calculate the signal flow. Furthermore it might be possible, to directly extract the flow from all e^+e^- pairs without taking the combinatorial background into account. The reason for this is that for continuum dileptons the combinatorial

pairs experience the same effects leading to the formation of flow as the signal pairs. Thus one could assume, that $v_2^{sig} = v_2^{tot}$. A hint in this direction is given by the fact, that the trend in the $\Delta\phi$ distribution as a function of centrality for signal pairs is also visible for all e^+e^- pairs. This is shown in Figure 3.21, where the yield of all e^+e^- pairs and the yield of the signal pairs is plotted against $\Delta\phi$ in 10 % centrality classes. The signal yield is scaled up for an easier comparison. The shape of the two distributions coincides very well.
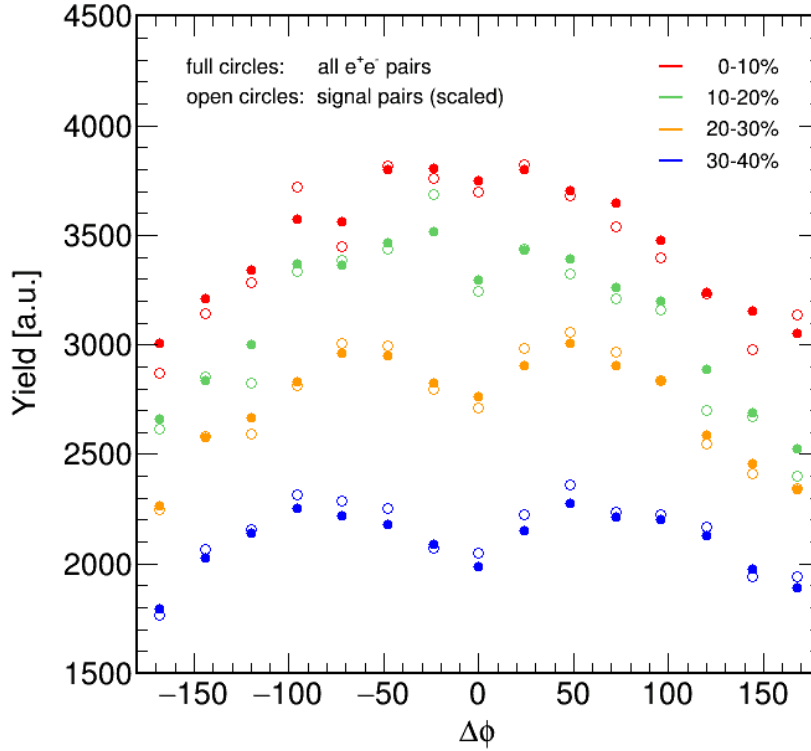
Figure 3.21: The plot shows the $\Delta\phi$ distribution of all e^+e^- pairs (full circles) and the signal pairs (open circles) after subtraction of the same-event like-sign background in the mass region below $0.12\,\text{GeV}/c^2$ in four centrality classes. The signal yield is scaled up to simplify the comparison of the two distributions. Errors are not plotted for better visibility. They range from 1.5 % for the most central events and all pairs up to 3.5 % for the signal pairs in the most peripheral events. The shape of the signal and all pairs is very similar.

In conclusion three different methods are available for the flow analysis, whereby not all three methods are applicable in every mass region. For the final analysis the mean of all methods in a mass bin is calculated as flow value. The statistical error is taken from the event-mixing method in the mass region beyond $0.12\,\text{GeV}/c^2$ and from the same-event like-sign geometric mean in the first mass bin. The systematic errors are estimated using the standard deviation of the applied methods.

Furthermore a differential analysis, especially in the low mass region where statistics is high, can be performed. Thus the flow is analyzed as a function of centrality, rapidity or transverse momentum. In the π^0-dominated region those results can also be compared to the ones obtained for the charged pions.

3.5.1 Efficiency Correction as a Function of Track Density

High particle multiplicities lead to reconstruction efficiency losses, because a high occupancy biases the track reconstruction. This results in a rapidity asymmetry. To account for these effects, a correction based on the track density is applied. The θ dependent track densities are measured for positive and negative charged pions and subsequently a correction matrix is constructed for each centrality class. Those correction matrices are displayed in Figure 3.22 for $0-10\%$ centrality.
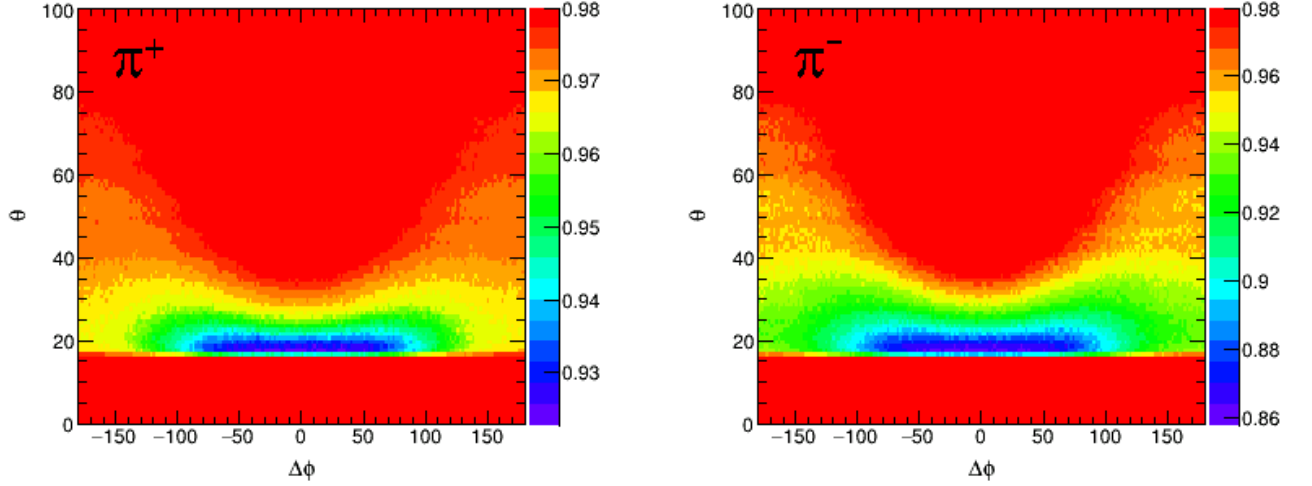
Figure 3.22: Occupancy correction matrices for π^+ and π^- constructed based on track density.

Since for this analysis particle pairs are used, the correction factor is calculated using the product of of the values for both particles extracted from the respective correction matrix. Equation 3.20 shows the calculation of this correction in case of unlike-sign pairs:

$$
\begin{aligned}
\mathrm{Corr}_{\mathrm{ee}}\left(\mathrm{E}_{\mathrm{ee}}, \vec{\mathrm{p}}_{\mathrm{ee}}, \psi_{\mathrm{RP}}\right) &= \mathrm{Corr}_{\mathrm{ee}}\left(\Delta\phi_{\mathrm{e}^+}, \theta_{\mathrm{e}^+}, \Delta\phi_{\mathrm{e}^-}, \theta_{\mathrm{e}^-}\right) \\
&= \mathrm{Corr}_{\pi^+}\left(\Delta\phi_{\mathrm{e}^+}, \theta_{\mathrm{e}^+}\right) \times \mathrm{Corr}_{\pi^-}\left(\Delta\phi_{\mathrm{e}^-}, \theta_{\mathrm{e}^-}\right)
\end{aligned}
\tag{3.20}
$$

For the elliptic flow the occupancy correction has almost no effect. Hence it is integrated into the systematic uncertainties. The directed flow on the other hand strongly depends on the rapidity, thus rapidity anisotropies have to be corrected and the occupancy correction influences the value of v_1 significantly.

4 Results

4.1 Elliptic Flow as a Function of Invariant Mass

The flow parameters are extracted as described in section 3.5 in four bins of invariant mass separately. In the pion region, where correlated background sufficiently contributes to the combinatorial background, event mixing can not be used for background determination. Thus two different methods, namely same-event like-sign background and assuming that $v_2^{sig} = v_2^{tot}$ are available in this mass range. In the last mass bin with $0,5\,\text{GeV/c}^2 \le M_{ee} \le 0.9\,\text{MeV/c}^2$ statistics is low and the same-event like-sign background is fluctuating a lot. Thus the value obtained with this background method is not taken into account. So in conclusion in each mass bin two or three different methods are available and used to determine the elliptic flow values. This is summarized in Table 4.1.

method mass	same-event	event mixing	$\mathbf{v}_{sig} = \mathbf{v}_{tot}$
0.00 - 0.12 GeV/c^2	-0.049 ± 0.008	-0.059 ± 0.005	-0.047 ± 0.003
0.12 - 0.25 GeV/c^2	-0.009 ± 0.083	-0.093 ± 0.046	-0.016 ± 0.004
0.25 - 0.50 GeV/c^2	-0.052 ± 0.166	-0.075 ± 0.049	-0.013 ± 0.006
0.50 - 0.90 GeV/c^2	0.897 ± 0.553	0.009 ± 0.138	-0.002 ± 0.026

Table 4.1: Elliptic flow values for the $40\,\%$ most central events obtained with three different methods for background evaluation. Due to correlated background pairs, mixing cannot be used in the first mass bin. Furthermore the low statistics in the high mass region lead to the same-event background being unprecise. Thus those two values (printed in gray) are excluded.

To obtain the final flow value, the outcome of the different methods is averaged. The statistical uncertainties are taken from the same-event like-sign method in the pion region and from event mixing at the higher masses. To estimate the systematic uncertainties, the standard deviation between the flow values is calculated:

$$\sigma = \sqrt{\frac{1}{n}\sum_{k=1}^{n}\left(v_2^k - \bar{v}_2\right)^2} \tag{4.1}$$

Where k denotes the used method. An additional systematic uncertainty is introduced by the occupancy correction, which was explained in section 3.5.1. On v_2 the influence is very small,

thus the value is taken without the correction because this allows the use of several different methods. Instead the deviation between the flow value with correction and without is added to the systematic error of the points. Figure 4.1 compares the outcome of the different methods for flow analysis in the four mass regions. In Figure 4.2 the final result including also the two different contributions to the systematic uncertainties is shown.
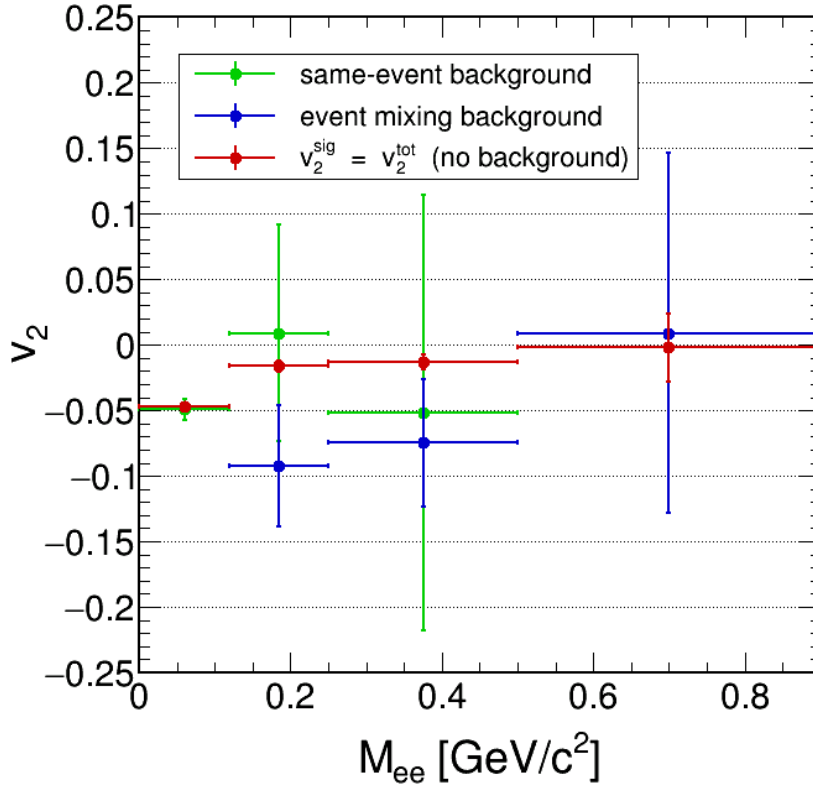
Figure 4.1: The plot shows v_2 for dileptons with different methods for background determination applied. The green points show the signal flow which is calculated using the same-event like-sign geometric mean background. It is used in the first three mass bins. For obtaining the blue points, the background is estimated via event mixing. Due to correlated background pairs in the first mass bin, this value is excluded here. The red points show the flow values obtained for all e^+e^- pairs, using the hypothesis that $v_2^{sig} = v_2^{tot}$. All three (two) methods are in very good agreement for every mass region.

For the mass region between $0.5 - 0.9\,\mathrm{GeV}/c^2$ it is easily visible, that there is no flow. For the two points between $0.25 - 0.5\,\mathrm{GeV}/c^2$ the situation is more difficult. They have a finite value, but within errors they are consistent with zero. Due to low statistics it is not possible to make a more clear statement. Of course, following the hypothesis that $v_2^{sig} = v_2^{tot}$ one could take a look at the behavior of the flow of all e^+e^- pairs (red points in Figure 4.1). Here it can be seen, that the elliptic flow for invariant masses of $0.25 - 0.5\,\mathrm{GeV}/c^2$ has a small but finite value. It has to be investigated, whether this contribution is caused by the η meson. If so, subtracting the eta would further reduce the flow in this mass region, leading to a value more close or equal to zero. In the lowest mass bin there is an elliptic flow of $v_2 = -0.047$ present. This value is in good agreement with the v_2 of the charged pions, which will be discussed more thoroughly
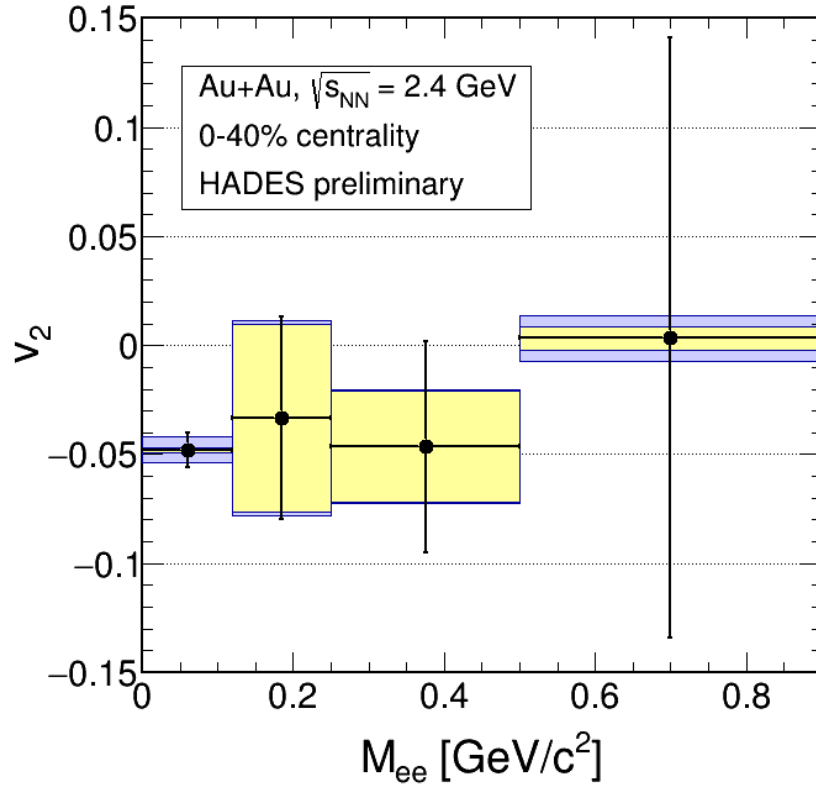
Figure 4.2: The figure shows the elliptic flow of dileptons plotted against invariant mass. The values are calculated using the mean of all available methods in the given mass region. The statistical uncertainties are taken from the analysis with same-event like-sign background in the pion region and mixed event background at the higher masses. The yellow boxes show the systematic uncertainties introduced by the differences between the used methods. The blue boxes indicate the additional contribution from the occupancy correction.

in section 4.2. All flow values are negative, which is expected in the SIS18 energy regime, where the ejectiles are preferably emitted out of plane due to the shielding of the spectators. An explanation for the decreasing flow in the larger masses could be, that this shielding influences hadrons but not leptons. Thus the dilepton pairs are ejected isotropically regardless of the surrounding spectator nuclei.

Results from a coarse-grained transport simulation concerning the collective transverse velocity β_T of dileptons with $0.3 \leq M_{ee} \leq 0.7 \, \text{GeV}/c^2$ show, that the majority (85%) of dileptons is emitted within a 13 fm/c time window, which very closely follows the build up of the collective medium flow. Thus most of the radiated dileptons do not carry the full transverse velocity, that would be present at freezeout. The simulation result is shown in the left panel of Figure 4.3, where the cumulative dilepton yield is plotted alongside β_T. This supports the argument, that elliptic flow, which is close to zero in this mass region (point three and four in Figure 4.2) and the effective temperature, which is calculated using the transverse expansion velocity, carry the same information. [81]

As mentioned above, in the second and third mass bin, a physics background dominated by η decays might be present. The right panel of Figure 4.3 shows the contributions to the dilepton

spectrum from first chance collisions and the freeze-out stage. The largest contribution in the mass region between $0.25 - 0.5\,\text{GeV}/c^2$ (second and third mass bin for flow analysis) stems from the η Dalitz decay, which is on the $10\,\%$ level. Up until now, η flow is not measured in Au+Au collisions at SIS18 energies, thus a direct comparison like in the pion dominated mass region is not possible. Measurements of η flow exist for collisions of $1.9\,\text{A}\,\text{GeV}\ ^{58}\text{Ni} + ^{58}\text{Ni}$ and $2\,\text{A}\,\text{GeV}\ ^{40}\text{Ca} + ^{\text{nat}}\text{Ca}$ by the TAPS collaboration. But due to the different system sizes and energies a direct comparison to the $1.23\,\text{A}\,\text{GeV}\,\text{Au}+\text{Au}$ collisions cannot be performed. However, subtracting the η would only lead to a further decrease of the flow in absolute value, thus the physics message would not change.
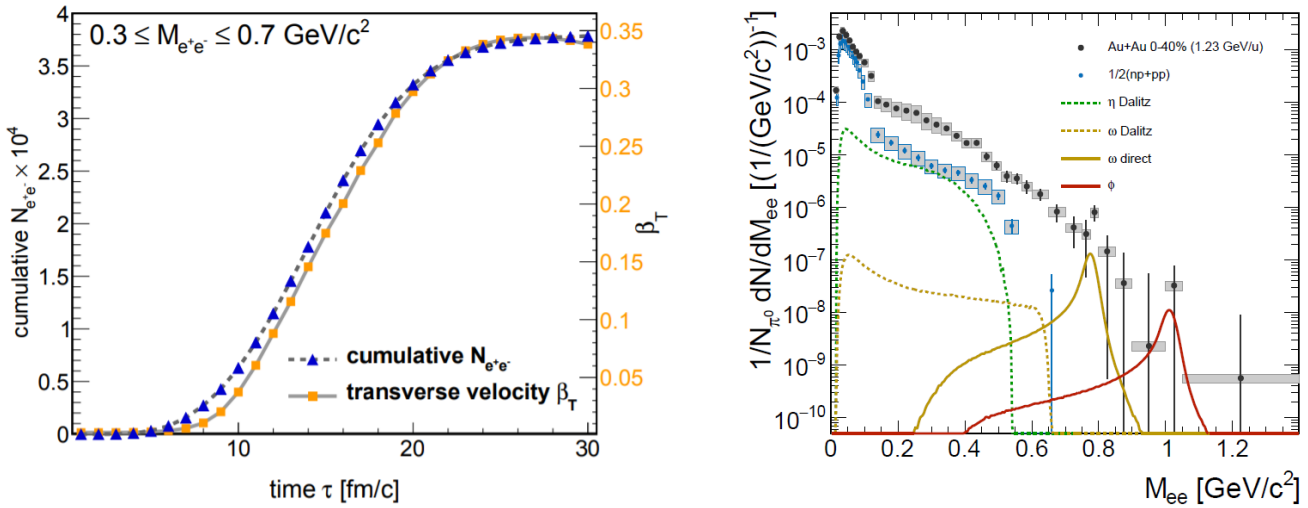
Figure 4.3: The left panel shows the time evolution of the cumulative dilepton yield (blue triangles) and the transverse velocity β_T (orange squares, right vertical scale) from a coarse-grained transport simulation. [81]
The right panel shows the efficiency corrected invariant mass spectrum together with the dilepton contributions from first chance collisions and the freeze-out stage. [53]

4.2 Comparison to the Charged Pions

In the mass region below $0.12\,\text{GeV}/c^2$ the dilepton spectrum is dominated by π^0 Dalitz decays. Thus a comparison between the elliptic flow of low mass dileptons to the v_2 of charged pions is very interesting. It is expected that all pion species experience the shadowing and squeeze-out in the same way. Hence the behavior of their azimuthal anisotropy should be similar. Figure 4.4 shows the $\Delta\phi$ distribution of the dilepton signal obtained using a same-event like-sign geometric mean background in four centrality classes. It is fitted with a Fourier expansion up to order 4, also including the sine terms. The v_2 extracted from this fit coincides with the one from the profiles filled with $\langle\cos(2\Delta\phi)\rangle$. From the most central events (left most panel) to the more peripheral events (right most panel) the influence of the second order cosine increases, which leads to the dip in the middle.

In Figure 4.5 the elliptic flow of dileptons in the π^0 dominated mass region is compared to the one of the charged pions (π^+) in four centrality classes. The dilepton v_2 is obtained as explained in section 4.1 by using the mean of the values with same-event like-sign background
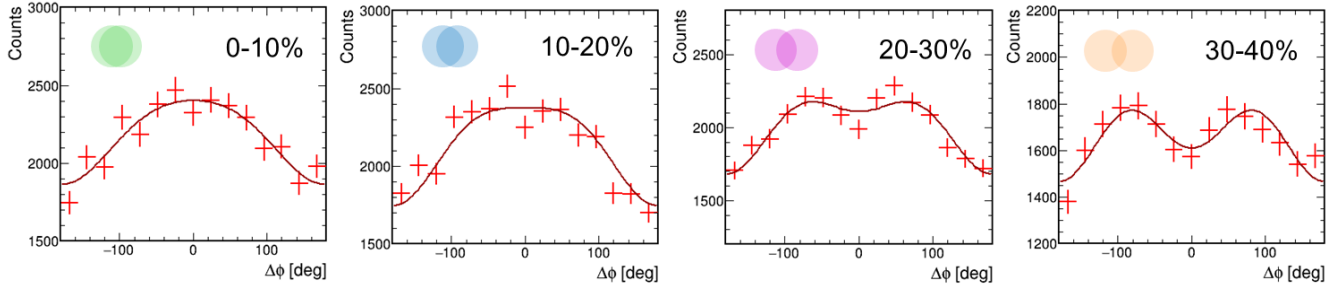
Figure 4.4: $\Delta\phi$ distribution of dileptons with $0 \leq M_{ee} \leq 0.12$ in four centrality classes. The influence of the second order cosine increases from the most central to the more peripheral events which leads to the dip at zero.

and no background method applied. The statistical errors stem from the like-sign method and the systematics are estimated using the standard deviation between the two methods and the deviations due to the occupancy correction. The dilepton flow is in very good agreement with the v_2 of the charged pions.
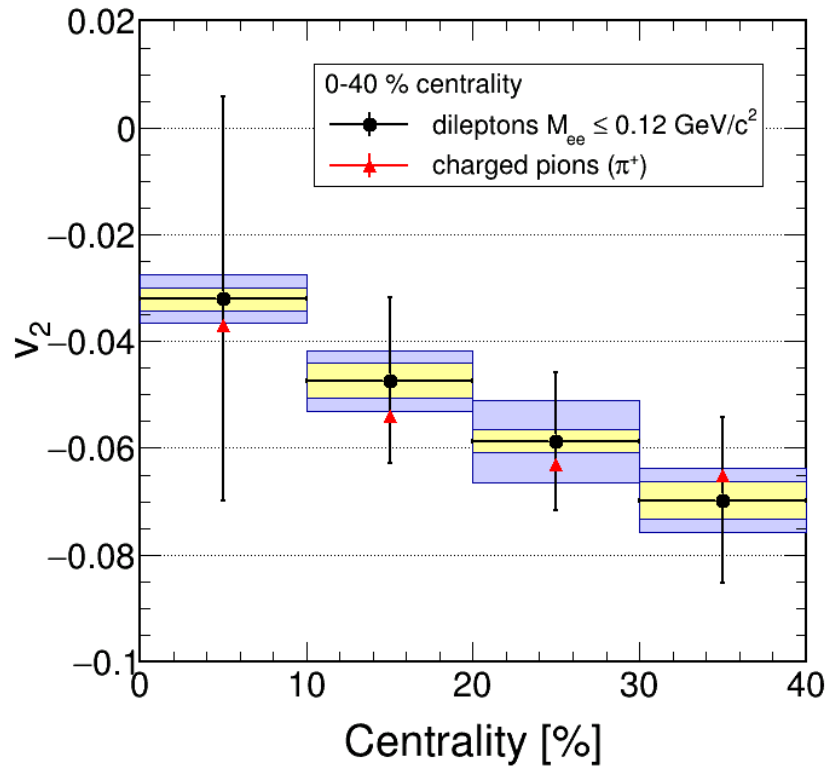
Figure 4.5: Elliptic flow of dileptons with $0 \leq M_{ee} \leq 0.12$ and positively charged pions in four centrality classes.

Furthermore a comparison of the p_T dependence of the elliptic flow of charged pions and dileptons in the π^0 region can be performed. Figure 4.6 shows a plot of v_2 against the transverse momentum of dileptons (black circles) integrated for $0 \leq M_{ee} \leq 0.12\,\mathrm{GeV}/c^2$ and $0-40\,\%$ centrality in comparison to the charged pions (triangles). The dilepton flow is in very good agreement with the flow of the charged pions over the whole p_T range.
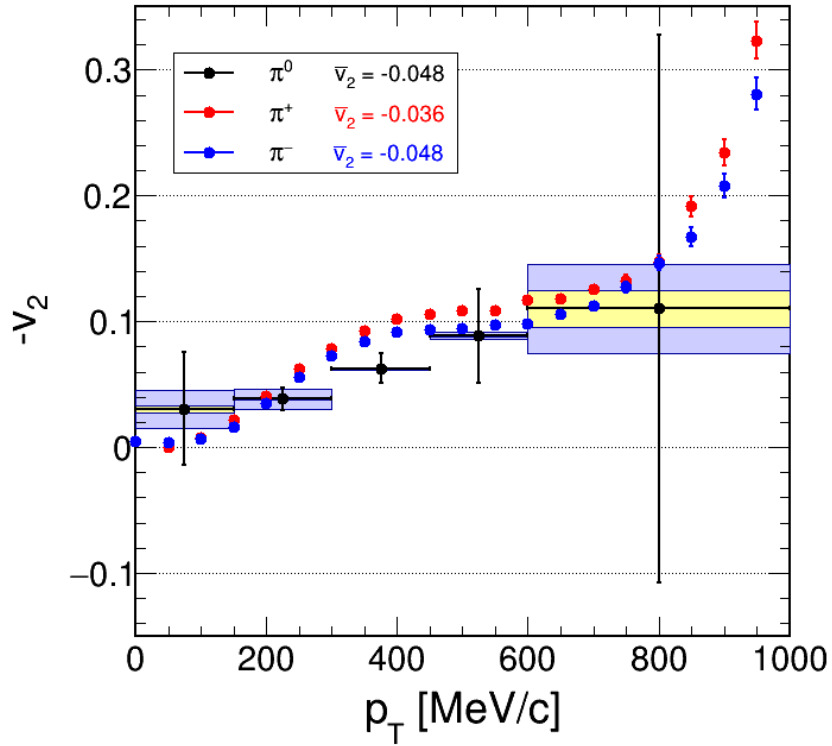
Figure 4.6: Elliptic flow of charged pions and dileptons in the π^0 mass region multiplied by -1 for $0-40\%$ centrality versus transverse momentum.

The comparison between the dileptons and charged pions shows the expected agreement, which can serve as a proof of principle that the applied reconstruction method is valid.

4.3 Centrality, Rapidity and Transverse Momentum dependent Analysis

In Figure 4.7 the elliptic flow of dileptons in the four described mass regions is plotted against rapidity for the $0 - 40\%$ most central events. Besides the flow in the lowest mass, all values are consistent with zero. Statistical as well as systematic errors are getting larger for the higher masses. Especially systematics have to be pointed out, since the additional contribution from the occupancy correction is not even taken into account here. Thus they would be even larger. In conclusion, there is no indication of a non-zero flow value above the pion dominated mass region.

Figure 4.8 displays the elliptic flow of dileptons integrated over all rapidities plotted against centrality in the four mass regions. Especially for the most central events the statistical errors are very large. For the three mass regions above the pion dominated mass bin, the values mostly coincide with zero. There are two exceptions, namely the $30 - 40\%$ most central events in the mass region between $0.12 - 0.25\,\mathrm{GeV/c^2}$ and the $10 - 20\%$ most central events in the mass region between $0.25 - 0.5\,\mathrm{GeV/c^2}$. Since the systematic uncertainties do not include the contribution from the occupancy correction, it is probable that the errors of those values would also touch zero. In the lowest mass region there is flow, which is in good agreement with the flow of the charged pions (see Figure 4.4). Thus in conclusion the elliptic flow for the masses above the pion region is mainly zero over all centralities.

The behavior of the elliptic flow versus the transverse momentum is shown in Figure 4.9. It is integrated over all rapidities and the $0 - 40\%$ most central events for the four mass regions. For the masses above $0.12\,\mathrm{GeV/c^2}$ all values with the exception of the flow for masses between $0.25 - 0.5\,\mathrm{GeV/c^2}$ and transverse momenta above $0.6\,\mathrm{GeV/c}$ are consistent with zero. Again, the systematics do not include the deviation from the occupancy correction, thus it may well be that also this value would be zero within errors. For the pion mass region a good agreement between the dilepton flow and the flow of the charged pions was discussed in Section 4.2. In conclusion a finite flow above the pion region is not visible.

In summary it can be stated, that there is no additional dependence of the flow pattern visible in the differential analysis. The higher mass regions do not show flow and no trend for different rapidities, centralities or transverse momenta is present. An η contribution must have been very small (at most 10%) and values with subtracted η would probably agree within errors with the presented analysis. In the region dominated by π^0 Dalitz decays finite flow values are measurable. As discussed in Section 4.2 they agree very well with the values measured in the charged pions.
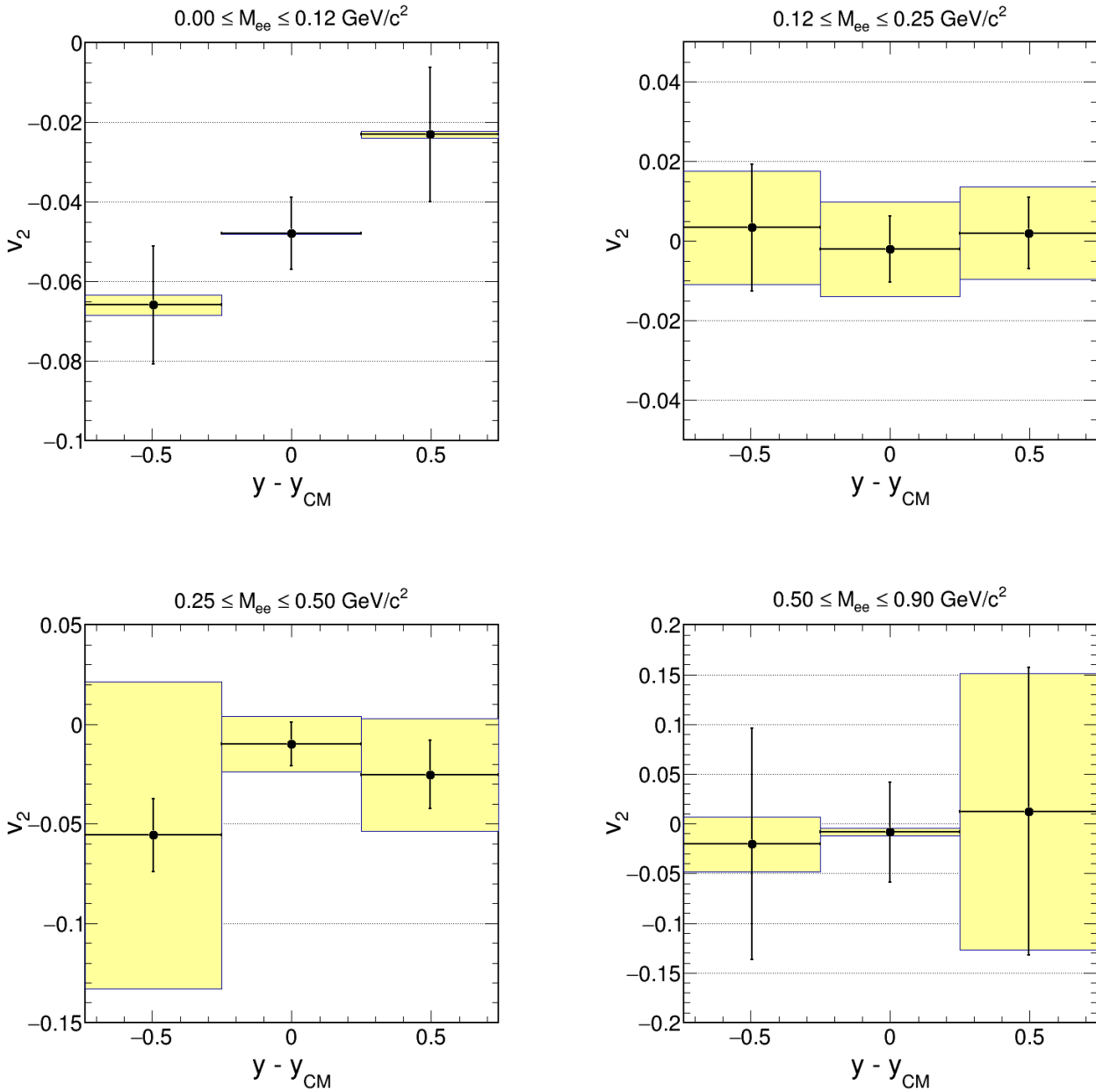
Figure 4.7: Elliptic flow of dileptons versus rapidity in four mass ranges for the $0-40\%$ most central events. The statistical errors are taken from same-event like-sign background in the lowest mass region (upper left) and event mixing background above. The systematic uncertainties take the standard deviation between the different applied methods for background estimation into account but not the deviations introduced by the occupancy correction.
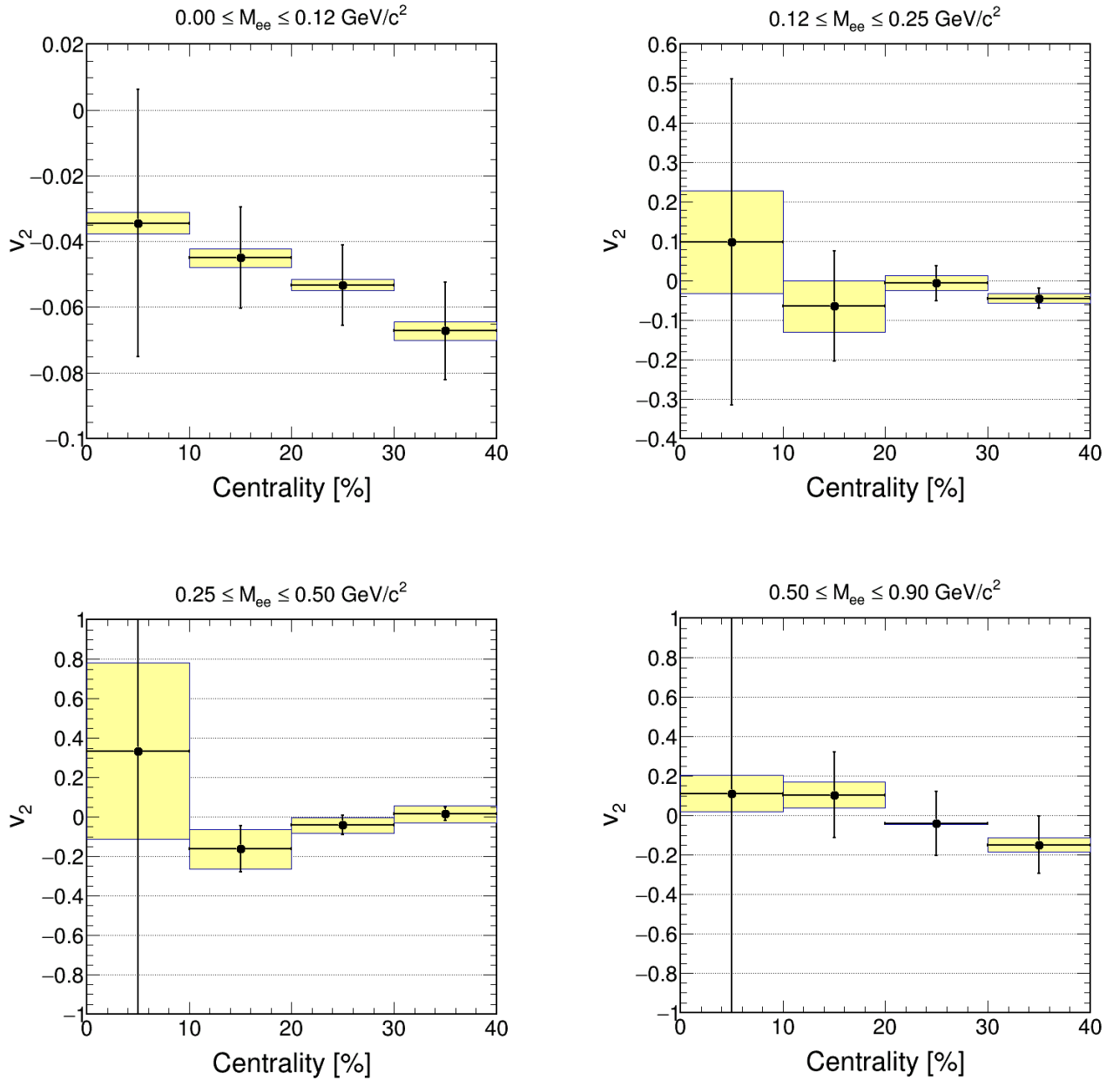
Figure 4.8: Elliptic flow of dileptons versus centrality in four mass ranges integrated over all rapidities. The statistical errors are taken from same-event like-sign background in the lowest mass region (upper left) and event mixing background above. The systematic uncertainties take the standard deviation between the different applied methods for background estimation into account but not the deviations introduced by the occupancy correction.
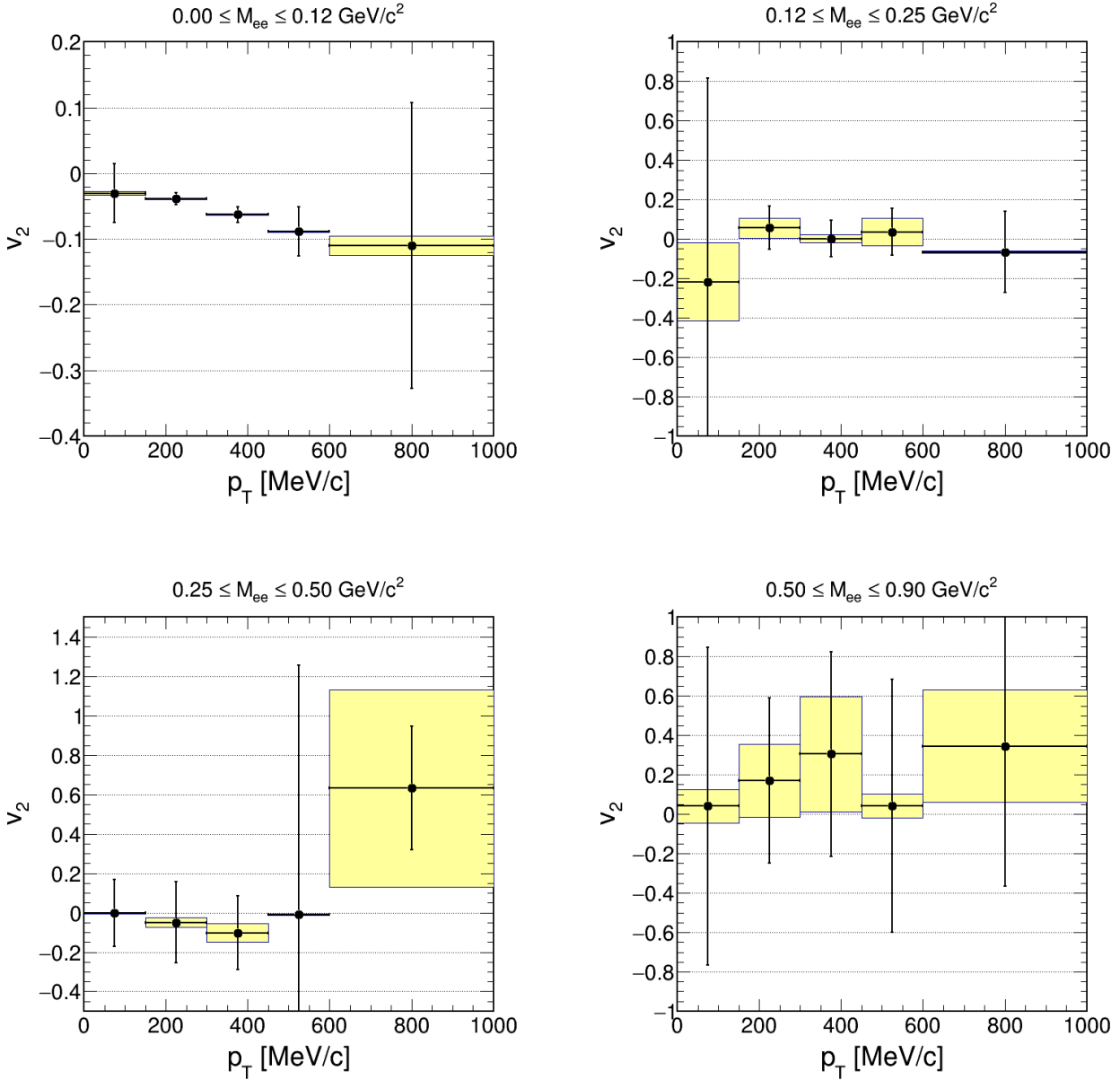
Figure 4.9: Elliptic flow of dileptons versus transverse momentum in four mass ranges integrated over all rapidities and the $0 - 40\%$ most central events. The statistical errors are taken from same-event like-sign background in the lowest mass region (upper left) and event mixing background above. The systematic uncertainties take the standard deviation between the different applied methods for background estimation into account but not the deviations introduced by the occupancy correction.

In addition to the elliptic flow, also the directed flow component v_1 can be analyzed. Since v_1 is influenced by rapidity, correcting for rapidity asymmetries is crucial. This is done using the occupancy correction. The correction matrices are build for charged pions and combined for the pairs. This procedure is still under investigation and might introduce further systematic uncertainties that are not yet determined. Hence they are not taken into account here, but it should be mentioned, that the shown systematic errors are expected to be larger, once the systematics due to the occupancy correction are included.
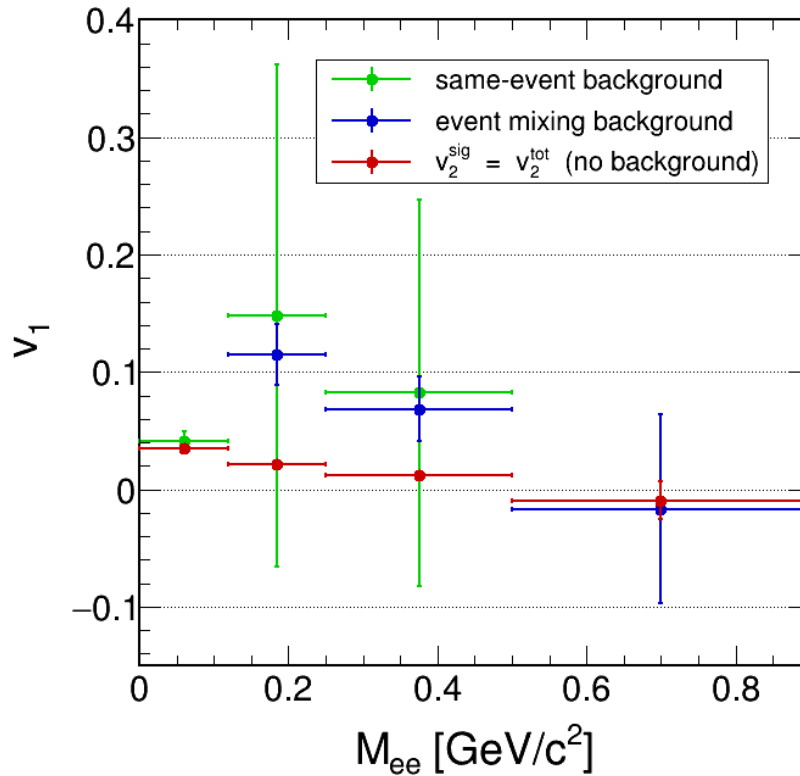
Figure 4.10: The plot shows the efficiency corrected v_1 for dileptons with different methods for background determination applied. The green points show the signal flow which is calculated using the same-event like-sign geometric mean background. It is used in the first three mass bins. For obtaining the blue points, the background is estimated via event mixing. Due to correlated background pairs in the first mass bin, this value is excluded here. The red points show the flow values obtained for all e^+e^- pairs, using the hypothesis that $v_2^{sig} = v_2^{tot}$.

The directed flow is expected to vanish at mid rapidity. Figure 4.11 shows the directed flow after occupancy correction for the $0-40\%$ most central events and integrated over all rapidities. Since the integral is symmetric around mid rapidity, the extracted values should be zero. This is not the case. The plots in Figure 4.12 of v_1 versus rapidity show the same behavior. The point at $y - y_{CM} = 0$ should be in agreement with zero. This is not the case for all mass bins below $0.5\,\mathrm{GeV/c^2}$, implying, that further corrections are needed. This is still under investigation. As
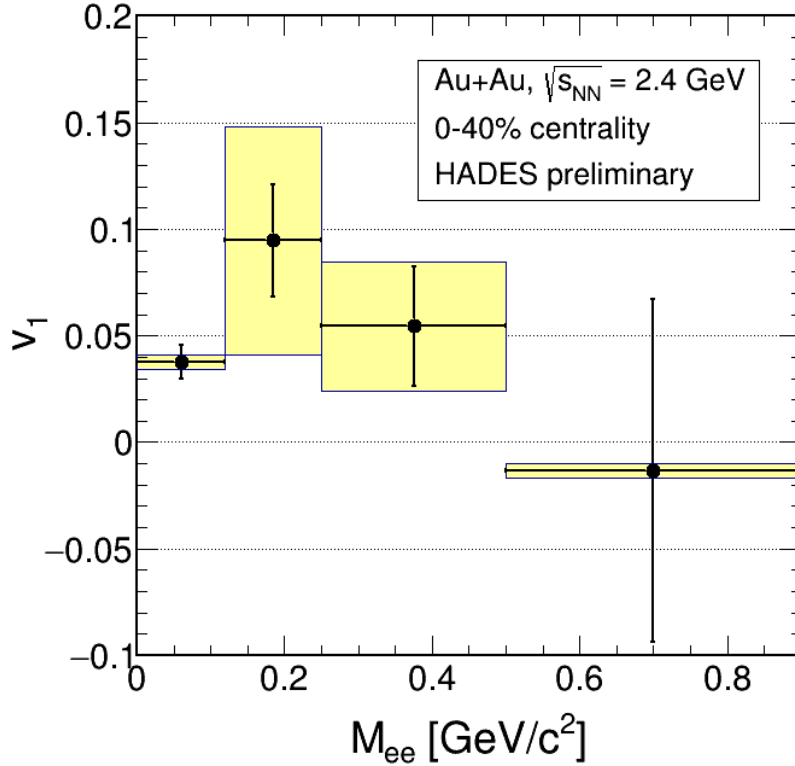
Figure 4.11: In this figure the efficiency corrected directed flow of dileptons plotted against invariant mass. The values are calculated using the mean of all available methods in the given mass region. The statistical uncertainties are taken from the analysis with same-event like-sign background in the pion region and mixed event background at the higher masses. The yellow boxes show the systematic uncertainties introduced by the differences between the used methods.

mentioned above, the occupancy correction is constructed from the charged pions and it is not finally resolved, if it behaves correctly for pairs. In Figure 4.13 and Figure 4.14 the centrality and transverse momentum dependent directed flow is displayed. A comparison to the charged pions is not performed, because of the obviously not complete corrections. Also different rapidity dependencies could distort a direct comparison of the values. An idea is to plot the rapidity dependent directed flow for different transverse momenta, fit the values and extract the slope at mid rapidity to compare it to the slope at mid rapidity of the charged pions. Figure 4.15 can give a first impression of the behavior of the slope of v_1 at mid rapidity. It has to be mentioned, that those values are extracted from all e^+e^- pairs with occupancy correction but without any background estimation. Furthermore, as stated above the applied correction seems not to be sufficient, thus those values might change. However, a comparison to the values of the charged pions could be interesting.
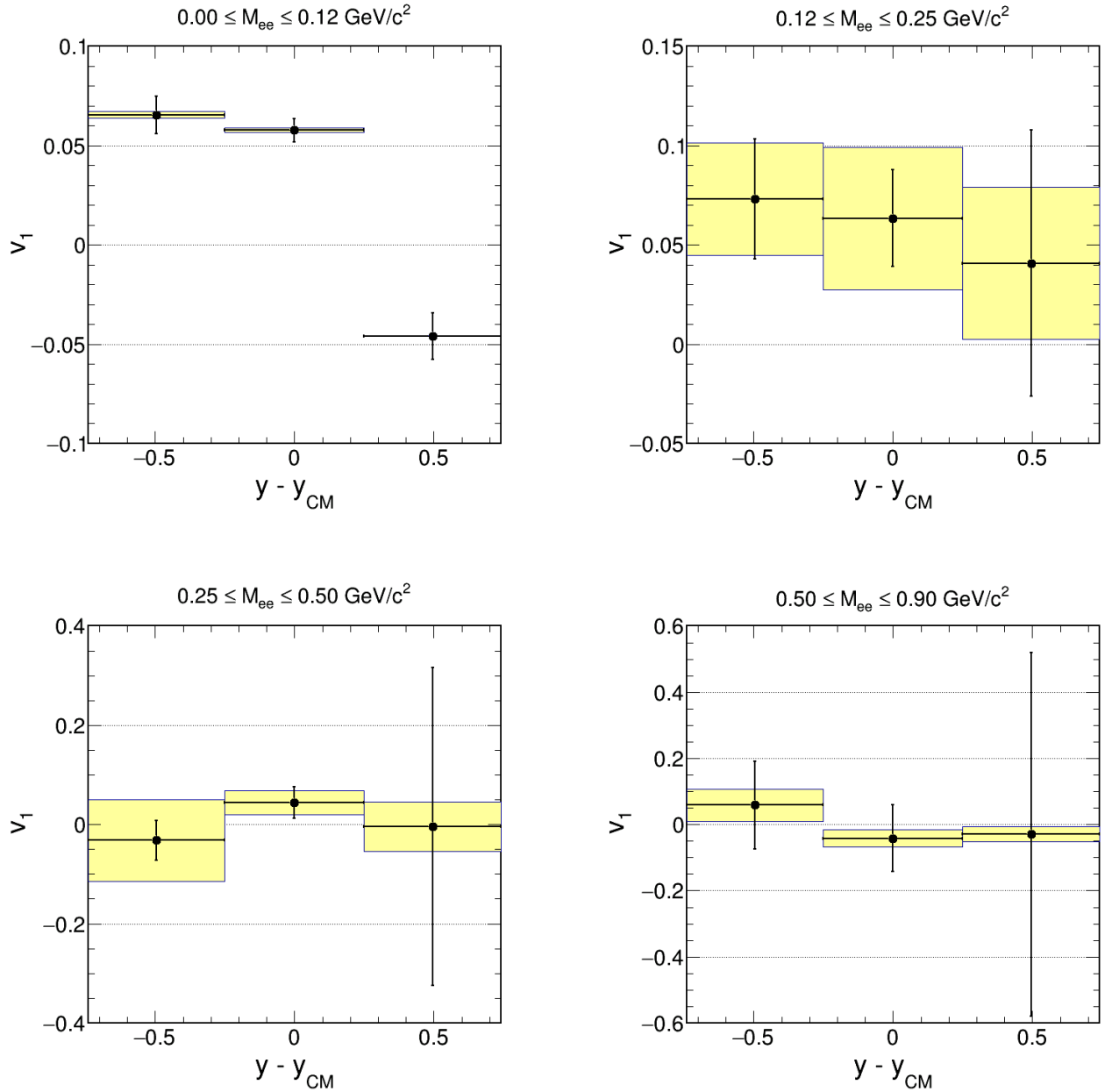
Figure 4.12: Efficiency corrected directed flow of dileptons versus rapidity in four mass ranges for the $0-40\%$ most central events. The statistical errors are taken from same-event like-sign background in the lowest mass region (upper left) and event mixing background above. The systematic uncertainties take the standard deviation between the different applied methods for background estimation into account but not the deviations introduced by the occupancy correction.
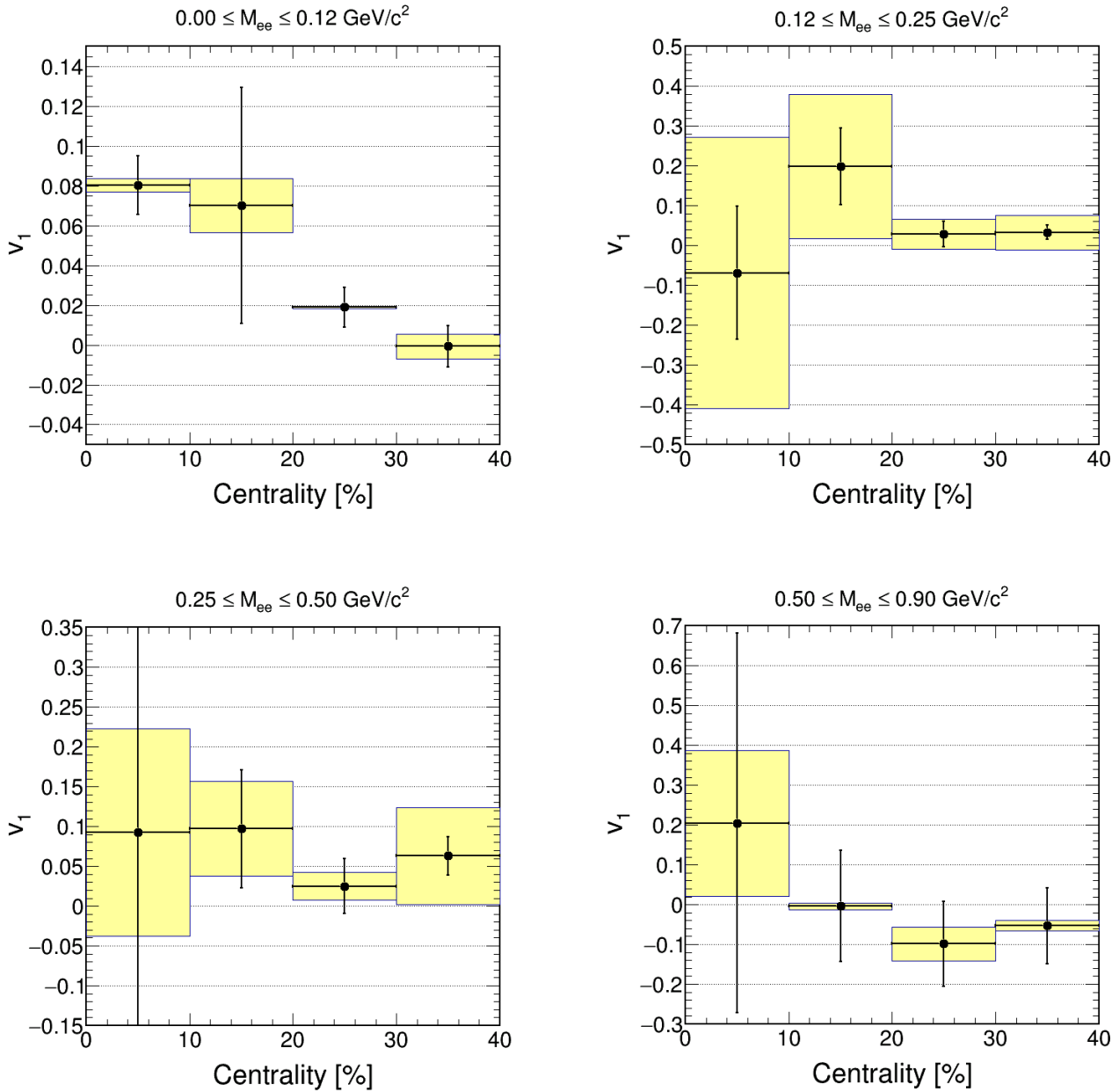
Figure 4.13: Efficiency corrected directed flow of dileptons versus centrality in four mass ranges integrated over all rapidities. The statistical errors are taken from same-event like-sign background in the lowest mass region (upper left) and event mixing background above. The systematic uncertainties take the standard deviation between the different applied methods for background estimation into account but not the deviations introduced by the occupancy correction.
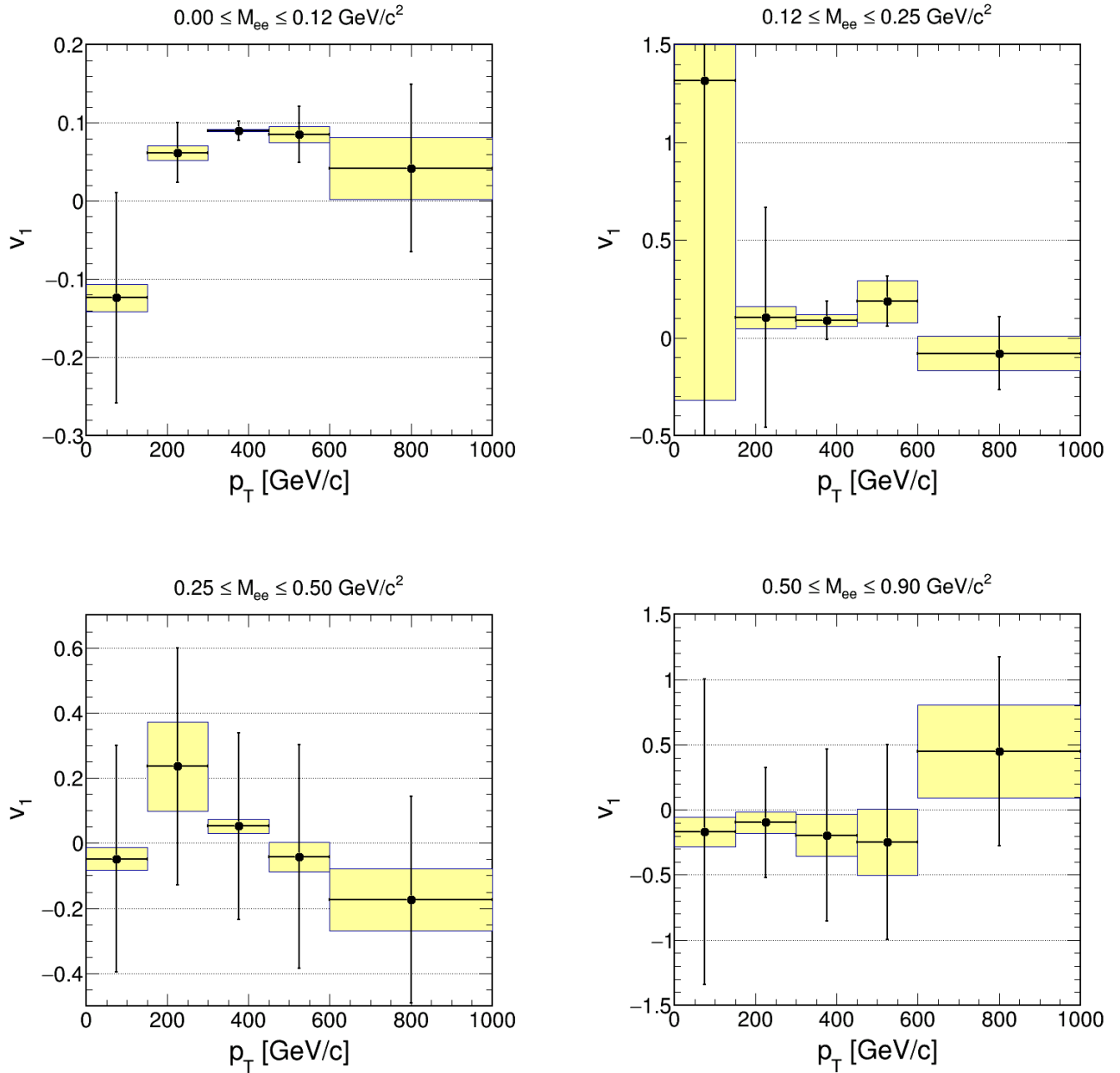
Figure 4.14: Efficiency corrected directed flow of dileptons versus transverse momentum in four mass ranges integrated over all rapidities and the $0-40\%$ most central events. The statistical errors are taken from same-event like-sign background in the lowest mass region (upper left) and event mixing background above. The systematic uncertainties take the standard deviation between the different applied methods for background estimation into account but not the deviations introduced by the occupancy correction.
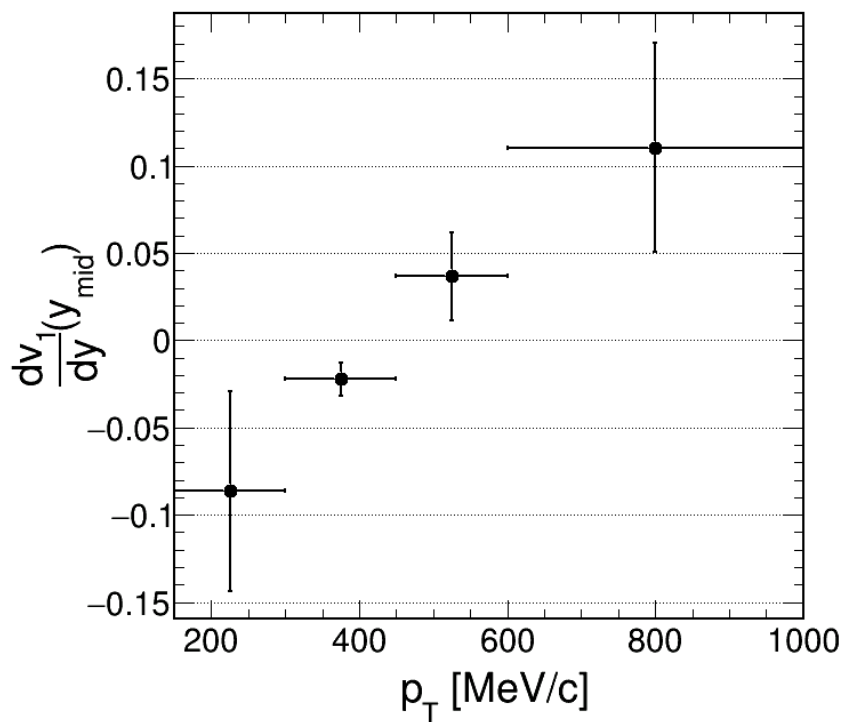
Figure 4.15: Transverse momentum dependent slope of v_1 of dileptons with $M_{ee} \leq 0.12\,\mathrm{GeV/c^2}$ at mid rapidity. The values are extracted from all e^+e^- pairs with occupancy correction but without any background estimation.

5 Conclusion and Outlook

The aim of this thesis was to analyze the azimuthal anisotropy from Au+Au collisions at $\sqrt{s_{NN}} =$ 2.4 GeV. The main focus was put on the second order flow v_2 that was investigated in four mass regions for different centralities, rapidities and transverse momenta. A similar analysis was performed for the directed flow v_1, but it became apparent, that further corrections are missing. Two different methods for flow analysis were introduced in the proposal to this work, namely directly fitting the signal $\Delta\phi$ distribution and calculating the signal flow from the flow component extracted via a fit of the $\Delta\phi$ distribution of all e^+e^- pairs and the background. In this thesis a third method was suggested, that uses profile histograms directly filled with the mean value of $\cos(n\Delta\phi)$ to obtain v_n. This method does not use an approximation, because every fit function has to be truncated in some order and the profiles are exact. Furthermore additional uncertainties due to the chosen bin size of the $\Delta\phi$ histograms can be avoided. Thus the profile method was chosen for the final flow analysis. In addition different methods for the determination of the combinatorial background were investigated. The same-event like-sign geometric mean background that is also able to reproduce the correlated background in the pion dominated mass region, the event mixing background and finally the hypothesis that the flow of the signal coincides with the flow of all pairs. For the event mixing background a careful tuning of all mixing parameters was done and especially the use of a constraint on the difference of the event plane angles of the mixed particles instead of fixed event plane bins has to be pointed out, since it lead to a large improvement of the background description. A study of the systematic uncertainties introduced by the different methods was performed and in addition the uncertainty due to the occupancy correction was taken into account for the elliptic flow. In case of the directed flow the occupancy correction was applied rather than introduced as an systematic uncertainty, because the directed flow is largely influenced by rapidity asymmetries. Nevertheless, this occupancy correction was still not sufficient to obtain vanishing directed flow at mid rapidity. Thus a further investigation of the effects leading to those rapidity asymmetries is needed and a suitable correction has to be found. This is also the reason why no comparison of the directed flow of dileptons in the pion region and charged pions was performed. However, due to potentially different rapidity effects a direct comparison would not be favorable. Instead a comparison of the slopes at mid rapidity for different transverse momenta could be the better choice. The elliptic flow of dileptons with $M_{ee} \leq 0.12$ GeV/c^2 was compared to the v_2 of charged pions for different centralities and transverse momenta. They are in very good agreement, which proves that the main source of flow in this region stems from the π^0. It further serves as a prove of principle for the chosen reconstruction method. For the higher masses the elliptic flow vanishes. The very small contributions left for the mass region between $0.12 - 0.5$ GeV/c^2 might be explained by a contribution from the η meson. So in conclusion it can be stated, that in the dilepton excess radiation no elliptic flow is observed. This can be explained by the mechanism, that leads to elliptic flow in the SIS18 energy regime. The shadowing of the spectators that reduces the mean free path of particles that are emitted in the direction of the reaction plane is clearly not influencing the lepton pairs as much as the hadrons. Thus the observed squeeze-out of particles perpendicular to the reaction plane seems to be valid only

for hadrons. The elliptic flow is expected to behave similar as the effective temperature. A comparison to a coarse-grained transport simulation of the transverse velocity, which enters the calculation of the effective temperature, and the cumulative yield of dileptons with masses between $0.3 - 0.7\,\mathrm{GeV/c^2}$ shows, that the majority of dileptons ejected in this mass region do not carry the full transverse velocity measured in hadrons. Thus a vanishing elliptic flow for the dilepton excess radiation makes sense.

As mentioned above, a better understanding of the rapidity asymmetry effects and its correction for pairs is needed to allow for a good reconstruction of odd flow components like v_1. Afterwards also a comparison to the charged pions could be performed for the directed flow. Lastly the data on η flow obtained by the TAPS collaboration could be used to estimate the expected flow in our collision system and energy to better understand the physics background contribution.

In the upcoming Ag+Ag beamtime a higher statistic also for the higher invariant masses is expected. Moreover the new electromagnetic calorimeter will enable HADES to measure neutral mesons like π^0 and η via their two photon decay. Thus a direct comparison between the Dalitz decay channel and the two photon decay can provide further insights.

List of Figures

List of Tables

Bibliography

[1] M. Gell-Mann. The eightfold way: A theory of strong interaction symmetry. Technical report, California Inst. of Tech., Pasadena. Synchrotron Lab., mar 1961.

[2] D. Griffiths. *Introduction to Elementary Particles*. Wiley VCH Verlag GmbH, 2008. ISBN 3527406018.

[3] M. Gell-Mann. A schematic model of baryons and mesons. *Physics Letters*, 8(3):214–215, feb 1964. doi:10.1016/s0031-9163(64)92001-3.

[4] G. Zweig. An SU(3) Model for Strong Interaction Symmetry and its Breaking. *CERN Report No.8182/TH.401*, jan 1964. URL http://cdsweb.cern.ch/record/570209/files/CERN-TH-412.pdf.

[5] M. Riordan. The discovery of quarks. *Science*, 256(5061):1287–1293, may 1992. doi:10.1126/science.256.5061.1287.

[6] G. Hanson et al. Evidence for jet structure in hadron production by e^+e^-- annihilation. *Physical Review Letters*, 35(24):1609–1612, dec 1975. doi:10.1103/physrevlett.35.1609.

[7] B. Povh, K. Rith, C. Scholz, and F. Zetsche. *Particles and Nuclei: An Introduction to the Physical Concepts*. Springer, 2008. ISBN 3540793674.

[8] H. Burkhardt and B. Pietrzyk. Low energy hadronic contribution to the QED vacuum polarization. *Physical Review D*, 72(5), sep 2005. doi:10.1103/physrevd.72.057501.

[9] R. Brandelik et al. Evidence for planar events in e^+e^- annihilation at high energies. *Physics Letters B*, 86(2):243–249, 1979. ISSN 0370-2693. doi:10.1016/0370-2693(79)90830-X.

[10] J. Ellis, M. K. Gaillard, and G. G. Ross. Search for gluons in e^+e^- annihilation. *Nuclear Physics B*, 111(2):253–271, 1976. ISSN 0550-3213. doi:10.1016/0550-3213(76)90542-3.

[11] J. Ellis. The discovery of the gluon. *International Journal of Modern Physics A*, 29(31), 2014. doi:10.1142/S0217751X14300725.

[12] C. Burgess and G. Moore. *The Standard Model*. Cambridge University Press, 2012. ISBN 1107404266.

[13] K. Kainulainen et al. A model for dark matter, naturalness and a complete gauge unification. *Journal of Cosmology and Astroparticle Physics*, 2015(07):34, jul 2015. doi:10.1088/1475-7516/2015/07/034.

[14] V. Khachatryan et al. Measurement of the inclusive 3-jet production differential cross section in proton–proton collisions at 7 TeV and determination of the strong coupling constant in the TeV range. *The European Physical Journal C*, 75(5), may 2015. doi:10.1140/epjc/s10052-015-3376-y.

[15] Jeff Greensite. *An Introduction to the Confinement Problem*. Springer Berlin Heidelberg, 2011. doi:10.1007/978-3-642-14382-3.

[16] Bengt Friman, Claudia Höhne, Jörn Knoll, Stefan Leupold, Jorgen Randrup, Ralf Rapp, and Peter Senger, editors. *The CBM Physics Book*. Springer Berlin Heidelberg, 2011. doi:10.1007/978-3-642-13293-3.

[17] C. Patrignani and others (Particle Data Group). Review of particle physics. *Chinese Physics C*, 40 (10), oct 2016. doi:10.1088/1674-1137/40/10/100001.

[18] M. Thomson. *Modern Particle Physics*. Cambridge University Pr., 2013. ISBN 1107034264.

[19] E. Witten. Current algebra theorems for the u(1) "goldstone boson". *Nuclear Physics B*, 156(2): 269–283, sep 1979. doi:10.1016/0550-3213(79)90031-2.

[20] Jeffrey Goldstone, Abdus Salam, and Steven Weinberg. Broken symmetries. *Physical Review*, 127 (3):965–970, aug 1962. doi:10.1103/physrev.127.965.

[21] J. Jankowski and D. Blaschke. Chiral condensate and the structure of hadrons. *Acta Physica Polonica B Proceedings Supplement*, 7(1):225, 2014. doi:10.5506/aphyspolbsupp.7.225.

[22] Murray Gell-Mann, R. J. Oakes, and B. Renner. Behavior of current divergences under SU3×SU3. *Physical Review*, 175(5):2195–2199, nov 1968. doi:10.1103/physrev.175.2195.

[23] R. Rapp, J. Wambach, and H. van Hees. The chiral restoration transition of QCD and low mass dileptons. In *Relativistic Heavy Ion Physics*, pages 134–175. Springer Berlin Heidelberg, 2010. doi:10.1007/978-3-642-01539-7_6.

[24] Volker Koch. Aspects of chiral symmetry. *International Journal of Modern Physics E*, 06(02):203–249, jun 1997. doi:10.1142/s0218301397000147.

[25] R. Rapp and J. Wambach. Chiral symmetry restoration and dileptons in relativistic heavy-ion collisions. *Advanced Nuclear Physics*, 25(1), 2000. URL http://arxiv.org/pdf/hep-ph/9909229v1.

[26] Tatjana Galatyuk and. The electromagnetic response of resonance matter and other strange observations. In *Proceedings of The 26th International Nuclear Physics Conference — PoS(INPC2016)*. Sissa Medialab, may 2017. doi:10.22323/1.281.0354.

[27] Kenji Fukushima and Chihiro Sasaki. The phase diagram of nuclear and quark matter at high baryon density. *Progress in Particle and Nuclear Physics*, 72:99–154, 2013. URL http://arxiv.org/pdf/1301.6377v3.

[28] Masayuki Asakawa Chiho Nonaka. Modeling a realistic dynamical model for high energy heavy ion collisions. *Progress of Theoretical and Experimental Physics*, sep 2012. doi:10.1093/ptep/pts014.

[29] Dmitri Kharzeev, Eugene Levin, and Larry McLerran. Parton saturation and npart scaling of semi-hard processes in QCD. *Physics Letters B*, 561(1-2):93–101, may 2003. doi:10.1016/s0370-2693(03)00420-9.

[30] Ionut Cristian Arsene. *Properties of hot and dense matter created in relativistic heavy ion collisions*. PhD thesis, University of Oslo, 2009. URL http://www4.rcf.bnl.gov/brahms/WWW/thesis/IonutArsene_phdThesis.pdf.

[31] A. Andronic. An overview of the experimental study of quark-gluon matter in high-energy nucleus-nucleus collisions. *International Journal of Modern Physics A*, 29(22), 2014. doi:10.1142/S0217751X14300476.

[32] E.V. Shuryak. Two scales and phase transitions in quantum chromodynamics. *Physics Letters B*, 107 (1-2):103–105, dec 1981. doi:10.1016/0370-2693(81)91158-8.

[33] K.J. Eskola, K. Kajantie, P.V. Ruuskanen, and K. Tuominen. Scaling of transverse energies and multiplicities with atomic number and energy in ultrarelativistic nuclear collisions. *Nuclear Physics B*, 570(1-2):379–389, mar 2000. doi:10.1016/s0550-3213(99)00720-8.

[34] Evolution of collisions and QGP, oct 2016. URL `https://particlesandfriends.wordpress.com/2016/10/14/evolution-of-collisions-and-qgp`. (accessed September 5, 2018).

[35] Ralf Rapp. Dilepton spectroscopy of QCD matter at collider energies. *Advances in High Energy Physics*, 2013. URL `http://arxiv.org/pdf/1304.2309v2`.

[36] R. Rapp, J. Wambach, and H. van Hees. *The Chiral Restoration Transition of QCD and Low Mass Dileptons*. Springer Berlin Heidelberg, 2010. doi:10.1007/978-3-642-01539-7_6.

[37] T. Ablyazimov et al. Challenges in QCD matter physics - The scientific programme of the Compressed Baryonic Matter experiment at FAIR. *The European Physical Journal A*, 53(3):60, Mar 2017. ISSN 1434-601X. doi:10.1140/epja/i2017-12248-y.

[38] Hendrik van Hees and Ralf Rapp. Dilepton radiation at the CERN super proton synchrotron. *Nuclear Physics A*, 806:339–387, 2008. doi:10.1016/j.nuclphysa.2008.03.009.

[39] Takao Sakaguchi. Photon and dilepton production in high energy heavy ion collisions. *Pramana*, 84(5):845–859, 2015. doi:10.1007/s12043-015-0970-3.

[40] I. G. Bearden et al. Collective expansion in high energy heavy ion collisions. *Physical Review Letters*, 78(11):2080–2083, mar 1997. doi:10.1103/physrevlett.78.2080.

[41] Payal Mohanty and. Elliptic flow of thermal dileptons as a probe of QCD matter. *Physical Review C*, 85(3), mar 2012. doi:10.1103/physrevc.85.031903.

[42] Rupa Chatterjee, Dinesh K. Srivastava, Ulrich Heinz, and Charles Gale. Elliptic flow of thermal dileptons in relativistic nuclear collisions. *Physical Review C*, 75(5), may 2007. doi:10.1103/physrevc.75.054909.

[43] G. Vujanovic, C. Young, B. Schenke, R. Rapp, S. Jeon, and C. Gale. Dilepton emission in high-energy heavy-ion collisions with viscous hydrodynamics. *Physical Review C*, 89(3), mar 2014. doi:10.1103/physrevc.89.034904.

[44] Dominique Dittert. Azimuthal anisotropy of virtual photons in Au+Au collisions at $\sqrt{s_{NN}} = 2.4\,\mathrm{GeV}$. *GSI Scientific Report 2016*, page 110, 2017. doi:10.15120/gsi-2017-00527.

[45] Norbert Herrmann, Johannes P. Wessels, and Thomas Wienold. Collective flow in heavy ion collisions. *Annual Review of Nuclear and Particle Science*, 49(1):581–632, dec 1999. doi:10.1146/annurev.nucl.49.1.581.

[46] Behruz Kardan. Flow harmonics of Au+Au collisions at 1.23 AGeV with HADES. *Journal of Physics: Conference Series*, 742:12008, aug 2016. doi:10.1088/1742-6596/742/1/012008.

[47] P. Salabura. HADES - A High Acceptance DiElectron Spectrometer. *Nuclear Physics B - Proceedings Supplements*, 44(1-3):701–707, nov 1995. doi:10.1016/0920-5632(95)00605-2.

[48] HADES wiki page. URL `https://hades-wiki.gsi.de/cgi-bin/view`. (accessed September 20, 2018).

[49] E. Berdermann, M. Ciobanu, N. Herrmann, K.D. Hildenbrand, M. Kis, W. Koenig, M. Pomorski, M. Rebisz-Pomorska, and A. Schuttauf. Diamond Start Detectors. In *2009 IEEE Nuclear Science Symposium Conference Record (NSS/MIC)*. IEEE, oct 2009. doi:10.1109/nssmic.2009.5401672.

[50] J. Pietraszko, W. Koenig, and M. Weber. A diamond Start-Veto system for the HADES heavy ion experiment. *GSI Scientific Report 2010*, 2011. doi:10.15120/gsi-2017-00527.

[51] J. Pietraszko, T. Galatyuk, V. Grilj, W. Koenig, S. Spataro, and M. Traeger. Radiation damage in single crystal CVD diamond material investigated with a high current relativistic 197Au beam. *Nuclear Instruments and Methods in Physics Research Section A: Accelerators, Spectrometers, Detectors and Associated Equipment*, 763:1–5, nov 2014. doi:10.1016/j.nima.2014.06.006.

[52] P. Sellheim. Backtracking algorithm for lepton reconstruction with HADES. *Journal of Physics: Conference Series*, 599:012027, apr 2015. doi:10.1088/1742-6596/599/1/012027.

[53] Patrick Sellheim. *Reconstruction of the low-mass dielectron signal in 1.23A GeV Au+Au collisions*. PhD thesis, Johann Wolfgan Goethe-Universität Frankfurt, 2017.

[54] J. V. Jelley. Cerenkov radiation and its applications. *British Journal of Applied Physics*, 6(7):227, 1955. URL http://stacks.iop.org/0508-3443/6/i=7/a=301.

[55] G. Agakichiev et al. The high-acceptance dielectron spectrometer HADES. *The European Physical Journal A*, 41(2):243–277, jul 2009. doi:10.1140/epja/i2009-10807-5.

[56] K. Zeitelhack et al. The HADES RICH detector. *Nuclear Instruments and Methods in Physics Research Section A: Accelerators, Spectrometers, Detectors and Associated Equipment*, 433(1-2):201–206, aug 1999. doi:10.1016/s0168-9002(99)00371-x.

[57] G. Kornakov. *New advances and developents on the RPC ToF wall of the HADES experiment at GSI*. PhD thesis, Universidad de Santiago de Compostela, 2012.

[58] D. Belver et al. The HADES RPC inner TOF wall. *Nuclear Instruments and Methods in Physics Research Section A: Accelerators, Spectrometers, Detectors and Associated Equipment*, 602(3):687–690, may 2009. doi:10.1016/j.nima.2008.12.090.

[59] G. Kornakov et al. Time of flight measurement in heavy-ion collisions with the HADES RPC TOF wall. *Journal of Instrumentation*, 9(11):11015, nov 2014. doi:10.1088/1748-0221/9/11/c11015.

[60] A. Blanco, P. Fonte, J. A. Garzon, W. Koenig, G. Kornakov, and L. Lopes. Performance of the HADES-TOF RPC wall in a Au+Au beam at 1.25 AGeV. *Journal of Instrumentation*, 8(01):1004, jan 2013. doi:10.1088/1748-0221/8/01/p01004.

[61] H. Alvarez Pol et al. A large area timing RPC prototype for ion collisions in the HADES spectrometer. *Nuclear Instruments and Methods in Physics Research Section A: Accelerators, Spectrometers, Detectors and Associated Equipment*, 535(1-2):277–282, dec 2004. doi:10.1016/j.nima.2004.07.276.

[62] O. V. Andreeva et al. Forward scintillation hodoscope for nuclear fragment detection at the high acceptance dielectron spectrometer (HADES) setup. *Instruments and Experimental Techniques*, 57 (2):103–119, mar 2014. doi:10.1134/s0020441214020146.

[63] I. Frohlich, M. Kajetanowicz, K. Korcyl, W. Krzemien, M. Palka, P. Salabura, C. Schrader, P. Skott, H. Strobele, J. Stroth, A. Tarantola, M. Traxler, R. Trebacz, and S. Yurevich. A general purpose trigger and readout board for HADES and FAIR-experiments. *IEEE Transactions on Nuclear Science*, 55(1):59–66, 2008. doi:10.1109/tns.2007.913487.

[64] J. Michel, M. Böhmer, M. Kajetanowicz, G. Korcyl, L. Maier, M. Palka, J. Stroth, A. Tarantola, M. Traxler, C. Ugur, and S. Yurevich. The upgraded HADES trigger and data acquisition system. *Journal of Instrumentation*, 6(12):12056, dec 2011. doi:10.1088/1748-0221/6/12/c12056.

[65] Tetyana Galatyuk. HADES overview. *Nuclear Physics A*, 931:41–51, nov 2014. doi:10.1016/j.nuclphysa.2014.10.044.

[66] List of all HADES beamtimes. URL `https://www-hades.gsi.de/?q=node/5`. (accessed September 19, 2018).

[67] I. Antcheva et al. ROOT — A C framework for petabyte data storage, statistical analysis and visualization. *Computer Physics Communications*, 180(12):2499–2512, dec 2009. doi:10.1016/j.cpc.2009.08.005.

[68] Laura Fabbietti. *Study of the* e^+e^- ^' *pair acceptance in the dilepton spectrometer HADES*. PhD thesis, Technische Universität München, 2003.

[69] S. Harabasz. *Reconstruction of virtual photons from Au+Au collisions at 1.23 GeV/u*. PhD thesis, Technische Universität, Darmstadt, 2017. URL `http://tuprints.ulb.tu-darmstadt.de/6605/`.

[70] George Fai and Jørgen Randrup. FREESCO: Statistical event generator for nuclear collisions. *Computer Physics Communications*, 42(3):385–397, nov 1986. doi:10.1016/0010-4655(86)90007-x.

[71] A. M. Poskanzer and S. A. Voloshin. Methods for analyzing anisotropic flow in relativistic nuclear collisions. *Physical Review C*, 58(3):1671–1678, sep 1998. doi:10.1103/physrevc.58.1671.

[72] Jean-Yves Ollitrault. Reconstructing azimuthal distributions in nucleus-nucleus collisions. 1997. URL `http://arxiv.org/pdf/nucl-ex/9711003v2`.

[73] Jean-Yves Ollitrault. Flow systematics from SIS to SPS energies. *Nuclear Physics A*, 638(1-2):195c–206c, aug 1998. doi:10.1016/s0375-9474(98)00413-8.

[74] S. Harabasz. Electron identification in au+au collisions at 1.23 GeV/u using multivariate analysis. *Journal of Physics: Conference Series*, 503:12014, apr 2014. doi:10.1088/1742-6596/503/1/012014.

[75] Christopher M. Bishop. *Pattern Recognition and Machine Learning*. Springer-Verlag New York Inc., 2006. ISBN 0387310738.

[76] S. Constantinescu, S. Dita, and D. Jouan. Study of the estimation of the combinatorial muon pair background. Technical report, Institut de physique nucléaire, Université Paris, 1996. URL `https://cds.cern.ch/record/301370/files/SCAN-9604149.pdf`.

[77] Marek Gazdzicki and Mark I. Gorenstein. Background subtraction from the dilepton spectra in nuclear collisions. 2000. URL `http://arxiv.org/pdf/hep-ph/0003319v1`.

[78] M. C. Abreu et al. Dimuon and charm production in nucleus-nucleus collisions at the CERN-SPS. *The European Physical Journal C*, 14(3):443–455, jun 2000. doi:10.1007/s100520000373.

[79] A. Adare et al. for the PHENIX Collaboration. Detailed measurement of the e^+e^- pair continuum in p+p and au+au collisions at sqrt(s_nn) = 200gev and implications for direct photon production. *Phys. Rev. C*, 81(034911), 2010. doi:10.1103/PhysRevC.81.034911.

[80] Frank Geurts. The STAR dilepton physics program. *Nuclear Physics A*, 904-905:217c–224c, may 2013. doi:10.1016/j.nuclphysa.2013.01.062.

[81] T. Galatyuk, P. M. Hohler, R. Rapp, F. Seck, and J. Stroth. Thermal dileptons from coarse-grained transport as fireball probes at SIS energies. *The European Physical Journal A*, 52(5), may 2016. doi:10.1140/epja/i2016-16131-1.